

DIAGNOSTICS FOR MAPPING A LASER-INDUCED PLASMA

By

DANIEL SHELBY

A DISSERTATION PRESENTED TO THE GRADUATE SCHOOL
OF THE UNIVERSITY OF FLORIDA IN PARTIAL FULFILLMENT
OF THE REQUIREMENTS FOR THE DEGREE OF
DOCTOR OF PHILOSOPHY

UNIVERSITY OF FLORIDA

2011

© 2011 Daniel Shelby

To ThumbWars, 985-5480, and Team Upstairs

ACKNOWLEDGMENTS

I thank Dr. Nicolás Omenetto for being an admirable advisor. He has always kept his door open for questions and his mouth closed when they were ignorant. He has humbled me by showing me the absolute limits on how much one person can know. Along with Dr. Ben Smith, a graduate student could not desire a better team to show him how little he knows and how far he can go. I thank Dr. Gary Hieftje for making my infancy in the scientific community an inviting one and pointing me to work for a very good and wise group of advisors.

I thank my predecessors, Dr. William Wetzel, Dr. Gerardo Gomez, Dr. Benoit Lauly, and Dr. Nicolas Taylor. Their hands-on experience gave me the courage and foolishness to dive into instrumentation head-on. I firmly believe that I only understand as much as I do now because I had their knowledge and experience to propel me beyond my years.

I thank my contemporaries, Greg Bishop, Jonathan Merten, Andrew Warren, Jared Lynch, Warren and Kyle Mino, and Dave and Natasha Pirman. Periodic discussions during relieving breaks reassured me that I was not so off track as I had feared. Travelling with them made it seem not so daunting.

I thank my family, Amanda, Julia, Ed, Sandy, Salah and Rachel for tolerating my moving across the country in pursuit of a continued education. I thank them for being there when I have needed them after not heeding them. I thank them for reminding me that down in the dumps, I should never go.

TABLE OF CONTENTS

	<u>page</u>
ACKNOWLEDGMENTS.....	4
LIST OF TABLES.....	7
LIST OF FIGURES.....	8
LIST OF ABBREVIATIONS.....	12
ABSTRACT.....	13
CHAPTER	
1 SCOPE OF STUDY.....	15
Introduction to LIBS.....	15
Laser-Induced Fluorescence.....	17
Instrumentation.....	19
General Geometry.....	19
Fluorescence Excitation.....	21
Spectrograph.....	24
CCD Binning.....	26
Monochromator.....	27
Timing.....	28
Absorption Source.....	30
2 SPATIALLY RESOLVED EMISSION.....	37
Motivation.....	37
Temperature and Electron Number Density Considerations.....	38
Experimental.....	42
Results.....	45
Conclusions.....	47
3 SCHLIEREN IMAGING.....	53
Motivation.....	53
Premise of Schlieren Imaging.....	55
Sedov-Taylor Blast Wave.....	59
Experimental.....	60
Results.....	62
Time Dependence.....	62
Energy Dependence.....	63
Density Dependence.....	64
Conclusions.....	65

4	SPATIALLY RESOLVED LASER-INDUCED FLUORESCENCE.....	72
	Motivation	72
	Experimental.....	74
	Results.....	77
	Atomic Fluorescence.....	77
	Ionic Fluorescence	78
	Vertically resolved.....	78
	Horizontally resolved.....	79
	Conclusions	82
5	TIME-RESOLVED LASER-INDUCED FLUORESCENCE.....	92
	Motivation	92
	Temperature Measurements.....	94
	Experimental.....	97
	Results.....	100
	Temperatures.....	100
	Removing Volumes from Calculated Temperatures	104
	Response Times	106
	Conclusions	110
6	CONCLUSIONS	122
	Completed Project Goals.....	122
	Future Project Goals.....	123
	LIST OF REFERENCES	128
	BIOGRAPHICAL SKETCH.....	142

LIST OF TABLES

<u>Table</u>		<u>page</u>
1-1	Properties of the dye lasers used in this study.	35
2-1	Composition of the D33 aluminum alloy used in this study in mass percent.	49
2-2	Central wavelengths for the nine spectral windows used in this study along with the relevant lines and associated spectroscopic quantities.	50

LIST OF FIGURES

<u>Figure</u>	<u>page</u>
1-1	General schematic for the proposed instrument. 33
1-2	Spectral width of dye laser centered at 283.305 nm..... 33
1-3	Absorption profiles of lead in a LIP at several delays after the plasma formation. 34
1-4	Time profiles of the excimer, dye laser, and doubled dye laser pulses..... 34
1-5	Effect of on-chip binning for the CCD. 35
1-6	MCP response to an LED as a function of applied voltage..... 35
1-7	Timing schematic for triggers and lasers. 36
1-8	Conversion between time and frequency for tuning the diode laser. 36
2-1	Trigonometry for optical emission collection..... 48
2-2	Diagram of raster across the plasma profile. 48
2-3	Map of the T determined from the Saha-Boltzmann plot in CF-LIBS..... 51
2-4	Map of the electron number density from the fitting of the H-alpha emission line..... 51
2-5	Maps of the aluminum distribution within the plasma. 52
2-6	Maps of the silicon distribution within the plasma..... 52
2-7	Maps of the magnesium distribution within the plasma. 52
3-1	Schematic for a generic lens schlieren system working in the dark field. 67
3-2	Comparison between bright and dark field cutoffs for schlieren imaging..... 67
3-3	Progression from dark to bright field schlieren by moving a horizontally oriented pinpoint cutoff horizontally. 67
3-4	Progression from bright to dark field schlieren by moving a horizontally oriented pinpoint cutoff vertically. 68
3-5	Schematic for the optics used in the schlieren imaging for this work..... 68

3-6	Image taken from WinSpec32 for measuring the propagation of the shockwave by bright field schlieren imaging.....	69
3-7	Shockwave expansion by bright field from a LIP formed with 69 mJ/pulse.	69
3-8	Image taken from WinSpec32 for measuring the propagation of the shockwave by dark field schlieren imaging.....	70
3-9	Shockwave expansion by dark field from a LIP formed with 69 mJ/pulse.	70
3-10	Energy dependence of the shockwave produced by a LIP at atmospheric pressure.	71
3-11	Density dependence of the shockwave produced by a LIP at 49 mJ/pulse.	71
4-1	Examples of the vertical extent of the plasma at two delays.	84
4-2	Diagram of the vertical separation of data within the CCD image at 0.5 μ s.....	84
4-3	LabVIEW VI used to select ROI's and parse data within for spatial resolution. ...	85
4-4	Spatially integrated Pb I emission and fluorescence signals at delays.	85
4-5	Examples of the Pb I parsed emission and fluorescence curves obtained at three heights within the plasma.	86
4-6	Waterfall plot of vertically parsed Pb I emission data.	86
4-7	Waterfall plot of vertically parsed Pb I fluorescence data.	87
4-8	Spatially integrated Ba II emission and fluorescence signals at delays. The spatial integration is along the vertical axis within the plasma.....	87
4-9	Examples of the Ba II vertically parsed emission and fluorescence curves obtained at three heights within the plasma.	88
4-10	Waterfall plot of vertically parsed Ba II emission data.	88
4-11	Waterfall plot of vertically parsed Ba II fluorescence data.	89
4-12	Spatially integrated Ba II emission and fluorescence signals at delays from a LIP of 11% Ba by mass. The spatial integration is along a horizontal axis within the plasma.....	89
4-13	Spatially integrated Ba II emission and fluorescence signals at delays from a LIP of 0.5% Ba by mass. The spatial integration is along a horizontal axis within the plasma.....	90

4-14	Examples of the Ba II horizontally parsed emission and fluorescence curves obtained at three positions within the plasma.	90
4-15	Waterfall plot of horizontally parsed Ba II emission data.	91
4-16	Waterfall plot of horizontally parsed Ba II fluorescence data.	91
5-1	Temperature dependence of the precision of the calculated temperature from a 10% error within the observed ratio.	112
5-2	Separation of energy level dependence of the precision of the calculated temperature from a 10% error within the observed ratio.	112
5-3	Lens geometry for spatially selecting regions of the plasma.	113
5-4	Energy level diagram for Ba II.	113
5-5	Temporal profile of the excitation pulse at 455.403 nm.	114
5-6	Repeatability of 4 temporal profiles of the 614.171 nm direct line fluorescence each averaged from 500 laser shots.	114
5-7	Temperatures calculated from the direct line fluorescence at 614.171 nm about 1 mm from the surface.	115
5-8	Temperatures calculated from the direct line fluorescence at 614.171 nm grazing the surface.	115
5-9	Temperatures calculated using the conventional Boltzmann plot method on D33 aluminum alloy under the same conditions as the Ba II studies.	116
5-10	Temperatures calculated with errors propagated from interpulse standard deviations.	116
5-11	Temperatures calculated from the direct line fluorescence at 489.997 nm after excitation by 452.493 nm.	117
5-12	Temperatures calculated from the collisionally coupled emission at 389.178 nm after excitation by 455.403 nm.	117
5-13	Temperature correction for volume ratio between emission and fluorescence. ..	118
5-14	614.171 nm emission and fluorescence traces.	118
5-15	389.178 nm emission and fluorescence traces.	119
5-16	Fluorescence traces for 614.171 and 389.178 nm along with scatter from the excitation laser at 455.403 nm.	119

5-17	Effect of normalization on a saturated fluorescence signal.....	120
5-18	Response times calculated from difference between the half intensity of the direct line fluorescence at 614.171 nm and collisionally coupled line at 389.178 nm.....	120
5-19	Fluorescence traces for 489.997 and 389.178 nm along with scatter from the excitation laser at 452.493 nm.....	121
6-1	Absorption of a diode laser as it is tuned away from the center of an argon metastable absorption profile.....	127

LIST OF ABBREVIATIONS

CCD	Charge Coupled Device
CF-LIBS	Calibration Free Laser-Induced Breakdown Spectroscopy
ICCD	Intensified Charge Coupled Device
LEAF	Laser-Excited Atomic Fluorescence
LIBS	Laser-Induced Breakdown Spectroscopy
LIF	Laser-Induced Fluorescence
LIP	Laser-Induced Plasma
LOD	Limit of Detection
MCP	Multichannel Plate
Nd:YAG	Neodymium-doped Yttrium Aluminum Garnet
OPO	Optical Parametric Oscillator
PMT	Photomultiplier Tube
Q-switch	Quality Factor Switch
RELIBS	Resonance Enhanced Laser-Induced Breakdown Spectroscopy
ROI	Region of Interest

Abstract of Dissertation Presented to the Graduate School
of the University of Florida in Partial Fulfillment of the
Requirements for the Degree of Doctor of Philosophy

DIAGNOSTICS FOR MAPPING A LASER-INDUCED PLASMA

By

Daniel Shelby

August 2011

Chair: Nicolás Omentto
Major: Chemistry

While laser-induced breakdown spectroscopy (LIBS) is an attractive technique because of its portability, ease of execution and built-in sample preparation, the technique suffers from poor precision. When compared to other plasma emission techniques, primarily inductively coupled plasma (ICP), its higher relative standard deviations increase its limits of detection. So much so that LIBS is primarily used to detect only the major elements of a sample. Depending on the spectroscopic properties of the element, some trace identification is possible, e.g. magnesium. Much of this imprecision stems from the coupling of the sampling, atomizing and exciting processes. For ICP analysis, the sampling is accomplished through digestion and the atomization and excitation occur in an almost static plasma. All three of these processes occur almost simultaneously in the laser-induced plasma (LIP) which is complicated by its dynamic nature.

Since each plasma lasts only several tens of microseconds, a limited amount of information is available from each interrogation. Accordingly, sometimes thousands of plasmas are formed during a single acquisition of data. As each of these plasmas is slightly different in its evolution, the analytically relevant radiation varies between them.

The goal here, then, is to develop a unified system that can interrogate these LIP's with as many spectroscopy techniques as is possible. Each technique lends more insight into the spatial and temporal structure within the plasma. A spatially selective emission strategy alongside two laser probe methods are evaluated for the purpose of mapping the plasma's evolution in space and time.

Moreover, by using a fast detector coupled with fast electronics, an attempt at the direct experimental evaluation of time-resolved collisional rate constants at several delays of plasma evolution is described. This is believed to be the first time such an attempt has been made within a LIBS plasma.

CHAPTER 1 SCOPE OF STUDY

Introduction to LIBS

As an analytical technique, LIBS is very straightforward instrumentally; however the physics behind the phenomenon are complex [1]. The basic and most common setup consists of a solid-state Nd:YAG laser operating at the fundamental wavelength of 1064 nm. The laser beam is focused through a convex lens to produce a point focus with a power density greater than 0.5 GW/cm^2 [2]. A breakdown of this kind on the surface is composed of a mixture of material and ambient atoms and ions as well as their counterparts, free electrons. Plasma formation begins with the intense emission of continuum followed by analytical line emission of ions and atoms as the prior recombines with lower energy free electrons. These plasmas are characterized by electron number densities near 10^{17} cm^{-3} and temperatures beginning near 20000 K and settling to 8000 K [3, 4]. Emission from the plasma is collected by a lens system, optical fiber or some combination therein. Detection depends on the application, but the most common is a spectrograph equipped with charge coupled device (CCD) array detector.

The concept of using a focused laser beam for the production of an emissive plasma was made reality very shortly after the production of the first lasers. In 1962, Brech and Cross were the first to present data from such an arrangement, though they did not publish [5]. LIP continued to be a focus of research, although the topics shared more with fundamental physics [6-8]. Despite the quick inception, some years passed before the technique developed much stand alone activity in spectroscopy. The name, LIBS, did not surface for twenty years [9]. With the establishment of the technique for

analytical chemistry [10, 11], the figures of merit were quickly established and the advantages of LIBS were highlighted, noninvasive [11], no sample preparation [10], and field portability [12].

By this time, much was known about the various regimes of laser power density and their applications to machining and metal working [13], however there was not a unified field of researchers using the technique for analytical chemistry. The spectroscopy of these interactions grew with advent of gated detectors. This coevolution stemmed from the continuum emission at the birth of the LIP. Bremsstrahlung from the free electrons emits a strong, short-lived continuum which covers the visible and UV spectrum. For this reason, integrating detection such as photographic plates are difficult to apply to LIBS detection. Initially, the gated detector was a photomultiplier tube (PMT) or photodiode array (PDA) with a pulsed power source. A PMT that was saturated by the initial continuum could be made blind at those times. Unfortunately, this still prevented spectrally resolved detection. Additionally, PDAs did not have the sensitivity of a PMT which limited their application to strong lines.

LIBS found a true partner in CCDs. Once the solid-state array detector become widely available in the 1990s, their application to imaging and spectroscopy was immediate. With the subsequent addition of intensifiers (ICCD), the sensitivity of the detector was sufficient for even weak lines and the array of pixels was 2-dimensional. Not only could the CCD resolve lines spectrally but spatially in the direction parallel to the grooves of the diffraction grating for a conventional Czerny-Turner spectrograph.

Throughout this time, laser sources were becoming more reliable and compact. Thorough studies of wavelength and pulse duration properties of LIP made the

application of LIBS more successful [14]. As with any technique, LIBS is not a panacea [15]. Although the laser properties are better controlled and understood, the interaction between laser pulses and material is strongly dependent on the material and surroundings [16-18]. Minimizing this effect with the proper marriage of material and laser properties ensures that LIBS does not become a pariah. This could very quickly be true if researchers ignore the noise present in all LIBS analyses [19].

Laser-Induced Fluorescence

Another laser technique, laser-induced fluorescence (LIF), had to wait several years before it could be applied to atomic spectroscopy. In this context, it is also referred to as laser excited atomic fluorescence (LEAF). As the absorption band of atomic states is very narrow, atomic LIF needed a continuously tunable laser [20]. Once this tool became available, study into atomic fluorescence induced by a laser source began [21, 22]. At that time, it was still known as Selective Excitation Spectroscopy, and what we know as Saturation was named Infinite Temperature Equilibrium. Over the next two decades, atomic fluorescence was applied to most atom reservoirs, flames [23], furnaces [24], glow discharges [25, 26], ICP [27], hollow cathodes [28] and LIP [10, 29]. Diagnostics were thoroughly studied for single and double probe geometries [30] as well as their application to ionization spectroscopy [31, 32].

As can be seen from the citations above, some ten years after the first application of tunable dye lasers to atomic fluorescence, a system was developed that used LIP-LIF. Kwong and Measures named their technique Trace (Element) Analyzer Based on Laser Ablation and Selectively Excited Radiation (TABLASER) [33]. This early work focused on the application of atomic fluorescence in a LIP for the construction of

calibration curves. Certainly, using the plume of a LIP as an atom reservoir for atomic fluorescence increases the sensitivity of the measurement over LIBS [34]. Measures continued some LIF work in LIPs [31, 35], but the method was dominated by LIF on small molecules as well as atoms by the electronics industry throughout the 1980s [36-38]. As was mentioned previously, the 1990s saw a collaboration form between LIBS applications and CCD detectors. Accordingly, the first resurgence of literature for LIBS-LIF frequently uses a camera to image atomic fluorescence from a sheet of excitation [39-41]. Primarily these papers are concerned with the spatial distribution of species within the plasma plume. Such information can optimize the analytical use of the plasma. Others obtain the spatial information by setting an observation height and measuring the fluorescence as a function of time [42-44].

In the late 1990s, a couple of papers surfaced with an interesting application for LIBS-LIF. The authors measure isotope ratios from fluorescence shifts in Li and U. The first application, to Li, uses a dye laser [45]. This is consistent with the bulk of the work done in the field to that date. Application of this technique to U was accomplished with a diode laser as the excitation source [46]. This appears to be one of the only applications of a diode laser for LIF within a LIP.

LIBS is still an analytical technique, so many papers that combine these methods hope to refine calibration curves to reduce the LOD for this direct sampling method [47-50]. To this point, much of the research had been done in a vacuum chamber where the ambient gas species and pressure had been closely controlled. The turn of the century also saw a rise in the application of this two-laser technique to atmospheric conditions for solids [51, 52], aerosols [53], and liquid jets [54]. In recent years, the

calibration curves have been obtained by optical parametric oscillators (OPOs) [34, 55-57]. From the literature, it seems these continuously tunable lasers are replacing the conventional dye lasers used in most previous papers.

Finally, a distinction should be made for atomic fluorescence within a LIP. There are two other techniques that share the same basic instrumental setup but differ greatly in their physical principles. First, double-pulse LIBS contributes energy to the plasma through the formation of another breakdown within the rarified atmosphere of the first [58]. This is not a tunable or selective technique. Secondly, Resonance Enhanced LIBS (RELIBS) is very similar to atomic LIF within LIBS. The major difference between the work contained herein and RELIBS is the target of the selective excitation [59-61]. Enhancement from RELIBS comes from exciting the major component within the plasma and allowing that deposited energy to distribute to the minor elements [62]. An apparent fluorescence is detected for almost all minor elements. This fluorescence is tunable over the absorption of the major element. While the excitation is selective, the fluorescence is not. The work completed here selectively excites only single atomic or ionic species. Also, RELIBS should be made distinct from Resonant Laser Ablation [63]. Here the ablation laser is tuned to an electronic transition to an analyte within the matrix. In this schematic, no secondary probe laser is used.

Instrumentation

General Geometry

The goal of this research is to examine a laser-induced plasma from as many spectroscopic angles as is possible. To this end, an experimental setup is required that could accomplish traditional LIBS emission measurements as well as atomic

fluorescence and absorption. The overall geometry is shown in Figure 1-1. Each of these experiments also needed to be completed with spatial or temporal resolution.

As was stated above, the setup revolves around a laser-induced plasma. The data presented in this thesis is collected from a laser-induced plasma formed by a pulsed, Nd:YAG laser (BigSky Ultra). This ablation laser operates at a fundamental wavelength of 1064 nm with a pulse width of 7 ns. It is possible to vary the laser pulse energy up to a maximum value of 78 mJ. The plasma is formed by focusing the laser through a plano-convex lens with a 2" focal length.

Emission and fluorescence spectra are collected using plano-convex lens pairs to alternately collimate and focus the image onto the slit of the monochromator or spectrograph. This arrangement is necessary over a single lens as the spacing between the plano-convex lenses is arbitrary so long as the plasma is well placed at $1f$ of the collimating lens. In this fashion, the monochromator and spectrograph can be placed arbitrarily away from the plasma source. A common alternative to this arrangement is the collection of emission by a single lens. In that configuration, both the object and image would be placed $2f$ from the lens. If both detectors are restricted to a $4f$ distance from the source, depending on the lens, proper placement of both detection systems would be overly complicated. Additionally, this lens combination gives higher resolution than a single bi-convex lens [64]. The plano-convex lens pairs arrangement also allows for convenient filtering in the collimated region.

The monochromator and spectrograph are positioned off axis from one another. In other words, both detection systems could have been placed 90° with respect to the fluorescence excitation. However, this orientation would preclude the detectors from

being used for any absorption measurements. Accordingly, the monochromator is placed at a larger angle away from the incident laser beam used for atomic fluorescence. Because of small changes in the observation regions of the two detection systems, the laser and sample are mounted on an x-y-z stage. The entire plasma source could be moved to be centered at the focus of either the monochromator or spectrograph.

Fluorescence Excitation

The optical probe used for the fluorescence studies is a dye laser (Scanmate 1, Lambda Physik). The cavity of the Scanmate dye laser is defined by a front mirror and diffraction grating. Wavelength selection by the diffraction grating allows the dye laser to be tunable across the fluorescence of the dye. A circulator pump constantly moves the dye through the cell to avoid damage and subsequent burning by the probe laser. Primarily, two laser dyes are used in this study. A green dye, Coumarin 540A (C540A, Exciton), is used within the tunable range of 520 – 600 nm when diluted in methanol. A blue dye, Coumarin 450 (C450, Exciton), is used within the tunable range of 430 - 480 nm when diluted in methanol. Alignment within the dye laser determines the spectral purity of the laser pulse. Amplified spontaneous emission is a side effect of the geometry within the dye laser optics. With the proper alignment, this can be minimized, but affects the bandwidth of the dye laser output. The C540A dye output is frequency doubled to reach the 280 nm regime for probing a lead transition. This laser output is used to induce laser fluorescence inside of a hollow cathode lamp at 405.781 nm with excitation at 283.305 nm. While the hollow cathode emission is constant, the fluorescence induced by the dye laser is transient, making it easily discernable from the hollow cathode emission. Within the hollow cathode lamp, the dominant broadening is

assumed to be Doppler at 600 K. Equation 1-1 predicts a line width of 0.4 pm when M is the molecular mass of lead and λ is 283.305 nm [65]. When an excitation scan is completed across the fluorescence from the hollow cathode lamp, Figure 1-2 shows a width of 4 pm.

$$\frac{\Delta\nu}{\nu} = \frac{\Delta\lambda}{\lambda} = 7.16 \times 10^{-7} \frac{\sqrt{T}}{\sqrt{M}} \quad (1-1)$$

Therefore, the dye laser output is an order of magnitude wider than the absorption profile of the lead within the hollow cathode lamp. From this estimation, the real width of the laser is taken to be the 4 pm measured in Figure 1-2. In addition to measuring the spectral width of the dye laser, this work makes a quick investigation into the spectral width of the atomic lead line at 283.305 nm. Figure 1-3 reproduces the laser profile from Figure 1-2 alongside the normalized Gaussian fits of excitation scans of lead within a LIP at several delays. Clearly, the line width decreases with the increase in delay. In contrast to the hollow cathode source, the laser profile is narrower than the atomic transition at 1 μ s. Since these profiles are not deconvoluted, the profiles at 5 and 10 μ s cannot be said to be spectrally wider than the laser profile, but they are certainly equal. While we only consider Doppler broadening within the hollow cathode, the LIP will have more contributions such as Stark broadening from free electrons. The trend from 1 to 10 μ s shows that the reduction in temperature and electron number density between these delays significantly contributes to the reduction of the line width.

One other consideration for the spectral intensity of the laser is the spacing of longitudinal modes within the laser profile. As the dye laser cavity has a set length, different wavelengths of light will coherently interact with themselves at different integers of $n\lambda$. When the cavity length, L , is long compared to the wavelength of light,

these integer values become very large. Therefore, small variations in the wavelength value can be compensated by the integer value, n , such that the following relation holds.

$$\Delta \nu = \frac{c}{2L} \quad (1-2)$$

where c is the speed of light. This expression defines the frequency spacing between longitudinal modes within the laser output. For a laser output centered on a wavelength, Equation 1-2 gives the spectral spacing of the modes that allow lasing within the cavity defined by length, L . So, for a small cavity, the modes are widely spaced and the allowed lasing wavelengths are widely spaced. This corresponds to regions of lower intensity between the modes. When the cavity length increases, the modes become more closely spaced and the intensity output versus wavelength or frequency has fewer fluctuations. The laser width calculated above, 4 pm, corresponds to a frequency width of 15 GHz. Equation 1-2 predicts a frequency spacing of modes within a 35 cm cavity to be 430 MHz. A simple division shows that there are 35 longitudinal modes within the half-width of the dye laser. Therefore, no significant intensity variations should occur over the spectral width of the dye laser.

These two dyes are used in two separate dye laser cavities. The concentration dependence of the focusing and steering optics makes it unrealistic to operate two, alternating dye cells within the same housing. Accordingly, the excimer laser beam had to be split to simultaneously pump both dye lasers. The excimer laser (LPX 200, Lambda Physik) is a xenon chloride excited complex laser with a wavelength of 308 nm. The maximum pulse energy is 110 mJ/pulse with a pulse width of 30 ns. A 50/50 beam splitter coated for 308 nm separated the laser to pump both dye lasers. High-reflective mirrors for 308 nm are used to steer the laser beams into the dye laser housings. A

significant amount of cell damage was experienced during the early stages of this work. To avoid this, no more than 20 mJ/pulse is given to either dye laser. Accordingly, the excimer laser is operated with an average pulse energy of 40 mJ/pulse. Since following this guideline, significantly less dye cell damage has been observed.

Figure 1-4 shows how the pulse shape of the dye laser strongly depends on the temporal behavior of the excimer laser. The dye laser energy also strongly depends on the input pump energy from the excimer laser and the concentration of the dye circulating through the cell. Given the pump energy stipulation above and a concentration of 1 mM C540A, the output energy at 566 nm is 400 μ J/pulse. With a concentration of 1 mM C450, the output energy at 455 nm is 600 μ J/pulse. The properties of the dye lasers are summarized in Table 1-1.

Spectrograph

Images and spectra are taken with a 500 mm Czerny Turner spectrograph (SP500, Acton). To match the $f/\#$ of 6.5, a 1" lens with a focal length of 7" is used to couple the light into the spectrograph. The entrance slit is variable as well as the grating used. Three gratings are mounted on a turret within the spectrograph. Depending on the desired resolution at the focal plane, the diffraction grating could be changed between 1200, 2400, and 3600 grooves/mm. For all of the work contained within this document, the 2400 grooves/mm is used. This choice was made based on the trade-offs associated with each grating. As the line density increased, the resolution of the spectrograph also increased. However, this increase in resolution came at a cost to the throughput of the instrument. Additionally, as could be deduced from the increase in resolution, the bandpass of the spectrograph decreases with the increase in line density. This is apparent when one considers that the detector spacing is set by the

pixel size. Any increase in resolution must, then, come from a wider physical separation of wavelengths. So, in the UV and blue spectral regions, a 2400 grooves/mm grating may have a bandpass of 7 nm while the 3600 grooves/mm grating would cover 3 nm across the detector.

This spectrograph is not equipped with an exit slit coupled to a PMT. Only an intensified charge coupled device (ICCD) (ICCD-576S, Princeton Instruments) is used for detection on this system. A CCD is an array detector. It has many thousands of individual detectors organized in a 2-dimensional grid that is well-suited to applications in imaging and spectroscopy. Each pixel has a square cross-section with a side length of 23 μm . When used in conjunction with a spectrograph, one dimension retains spatial information while the other dimension is used for discrimination of wavelengths. For applications that desired some physical resolution, the 'image' on the camera is retained, and the distribution of intensity at a given wavelength represents the physical distribution of emitters in the observed volume. The intensifier is a multichannel plate (MCP) to allow for fast response times. A voltage is applied to the MCP when the signal needs to be collected. At all other times, the MCP has no voltage gradient applied across its channels which eliminates any cascade amplification of electrons. In this fashion, the signal to the CCD can be gated on or off by the MCP. During the time that the MCP is gated on, the CCD integrates the amplified light signal transmitted by the intensifier.

Irising of the CCD image results if the lower limit of the integration time is approached. At such sort integration times, the center of the MCP never reaches the appropriate voltage to induce cascade amplification within the channels. The outermost

channels do have this amplification. The resultant image has a dark center where little or no amplification occurred. To avoid this side effect of short integration times on the MCP, the shortest gate width used in this work is 100 ns. The MCP is driven by a high-voltage pulse generator (PG-200, Princeton Instruments). Any external trigger given to this detection system is applied to this controller. The internal delay, gate width, and MCP voltage are set on the PG-200. Once the MCP is gated 'on', a signal is sent to the CCD controller (ST-138, Princeton Instruments). The CCD is set to integrate for 5 ms, ensuring that all photons generated by the MCP are collected.

CCD Binning

It is possible to sum the intensity of several pixels in the physical axis (at a given wavelength). This region is referred to, in the software, as the region of interest (ROI). The extent of this ROI is specified in the software that controls the camera readout. Summing can be executed on the CCD chip or within the software after the entire CCD chip had been read. Both binning options have their restrictions. Binning on chip requires that the total summed intensity be less than the well capacity of the shift register (last pixel of each row used to read out the charge to the computer). Since the shift register is a pixel, it can hold a charge of 65,000 counts. So, if one column of pixels within the ROI being summed has an accumulated charge greater than one pixel, or 65,000 counts, that region has to be summed within the software after readout. Summation of this sort introduces noise into the spectrum.

When the camera is set to bin pixels in the software, each pixel is read out individually through the cable connecting the camera to the camera controller. This is significant as the analog-to-digital conversion is done within the camera controller and not within the camera. Therefore, it is possible for the analog signal to pick up noises

as it is transmitted through the readout cable, much like an antenna. As each column is transmitted, the pixel intensities are superimposed over the interference picked up by the cable. The problem is exacerbated when columns are binned by the software and the in-phase interference gives the background a ripple. This ripple has a peak-to-peak intensity on the same order of magnitude as some signal peaks. In order to avoid this issue, the amplification of the signal is controlled in such a way as to avoid completely filling the shift register during on-chip binning. Figure 1-5 shows the dramatic increase in signal-to-noise when the output is binned on chip.

The amplification of the CCD image is controlled by varying the voltage applied to the MCP in front of the CCD chip. There is an extra controller, PG-200, that applies the voltage pulse to the MCP. With this controller, the MCP voltage can be varied from 500 V to 900 V. To quantify the response of the MCP at different voltages, a DC light source is monitored. A light emitting diode is chosen as the source because of its flat response with respect to time. So, the spectrograph is set to the zero-order, and the intensity reaching the CCD is measured with respect to the applied voltage to the MCP. Each response is normalized to the response at 500 V, the minimum, and plotted against the applied voltage in Figure 1-6. A power series is fit to the data which can be used to calculate the relative response for any given voltage.

Monochromator

A crossed Czerny Turner VUV monochromator (Model 218, McPherson) is used in this work. The system is not pumped down to vacuum as all of the desired wavelengths are reachable under atmospheric conditions. The focal length is 300 mm with an $f/\#$ of 5.3. Accordingly, a 1" lens with a focal length of 5" is used to couple the light into the

monochromator. Resolution within the monochromator is set by the variable entrance and exit slits and the 1200 grooves/mm diffraction grating.

Two detectors are used with the monochromator. A photomultiplier tube (PMT) sensitive to the UV\Visible wavelengths (R955, Hamamatsu) is used for slower response measurements. The PMT power supply provided voltage up to 1 kV (226, Pacific Power Supply). Signal from this detector is typically read out by a 500 MHz digital oscilloscope (TDS520A, Tektronix).

Faster detection is accomplished with a MCP-PMT (R1564U-07, Hamamatsu). A separate high voltage source is required for the MCP-PMT. This power supply (PS350, Stanford Research) is capable of applying steady voltages up to 3 kV. The signal through this detector is amplified by the much shorter transit-time of the multichannel plate. This gives the MCP-PMT a resolution in the sub-nanosecond range. Accordingly, a 6 GHz digital oscilloscope (TDS 6604, Tektronix) is used to read the signal from this detector.

Timing

Timing within the components of the setup is accomplished with a digital delay generator (DG535, Stanford Research) shown in Figure 1-1. The ablation laser is controlled externally by TTL pulses from the DG535. External triggers for the flashlamp and Q-switch are supplied with an interpulse delay of 165 μ s. This delay between the firing of the flashlamp and Q-switch is the optimal spacing set by the manufacturer. The internal delay between the Q-switch trigger and the plasma formation is 185 ns.

A third channel is used to send a TTL pulse to trigger the excimer laser. The internal delay between the external trigger of the excimer laser and the output of laser light is 885 ns. Therefore, if both lasers are fired simultaneously, the shortest delay

between the plasma formation and the fluorescence probe would be 700 ns. Since this setup needs to be as versatile as possible, the excimer laser is triggered independently of the Q-switch within the ablation laser. By this logic, the excimer laser, and subsequently the fluorescence probe, could be fired even before the plasma formed. The fluorescence could be probed at any time during the life of the plasma. Unfortunately, this leaves the system vulnerable to the jitter present in the excimer laser. Although the trigger sent to the excimer has negligible jitter in the time domain, the output from the excimer laser can vary up to 50 ns. More simply, the maximum time difference between any two observed laser outputs is 50 ns. These laser pulses all averaged a delay of 885 ns. The delays described in this section are summarized in Figure 1-7.

For time-resolved data collection on an oscilloscope, a photodiode is placed in the excimer pump beam to trigger collection. In this fashion, the plasma formation seemed to jump around on the scope up to 50 ns away while the fluorescence signal from the probed atomic or ionic transition remains stationary in time. Averaging of the fluorescence signal is accomplished in this way.

Fluorescence work with the time-integrated camera is completed with the intensifier gate time set wider than the maximum 50 ns jitter present in the excimer beam. This restriction coincides, conveniently, with the minimum gate requirements to avoid iris-ing within the intensifier. From the fourth channel on the DG535, a synchronous pulse is sent to the PG-200 when the excimer is triggered. The 885 ns internal delay of the excimer laser is then matched within the PG-200 such that the

MCP is gated 'on' during the excimer laser pulse. During the fluorescence work, that gate width is 100 ns.

Absorption Source

The instrument constructed for this work is also capable of absorption measurements. These are realized using much the same logic as that of Dr. Lauly during his dissertation work [66]. LIP's are made in the same manner as previously described. Unlike the previous sections, the timing is not dictated by the DG535. While the delays are still regulated by the delay generator, the master trigger comes from a triangle waveform generator (Meterman FGC3, Wavetek) operating at 10 Hz and a variable peak-to-peak voltage. Typically, this voltage is kept at 2 V. The triangle waveform is split to trigger the delay generator as well as drive the piezoelectric tuning arm of a diode laser (TEC 500, Sacher Lasertechnik). The diode laser is driven by a modular laser drive (MLD 1000, Sacher Lasertechnik) equipped with current, temperature and tuning controls. It is possible to tune the central wavelength of diode laser with this controller while the triangle wave input from the waveform generator causes the output wavelength to oscillate about that center.

Laser output is steered through a cold Cs cell as well as a Ar filled galvatron (L2783-82ANE-PB, Hamamatsu). The galvatron is a see-through hollow cathode lamp. The cathode is mounted sideways between two Brewster angle windows to allow optical access to the discharge. As the diode laser passes through the two atom reservoirs, atomic absorption can be used to establish a wavelength reference for absorption measurements within a LIP. Laser intensity is monitored by a PMT (R928, Hamamatsu) mounted on a 0.1 m monochromator (H10, ISA America Inc.). The PMT voltage is monitored by an oscilloscope operated at a 1 M Ω input impedance. Such a high

resistance is used to amplify the slow signal coming from the continuous-wave diode laser. Figure 1-8 shows an example of these wavelength references. There are two Cs transitions separated by 9.1 GHz. Additionally, the Ar transition is set 8.9 GHz from the nearest Cs transition. Since the frequency spacing of the transitions is well known and the time scale is monitored by the oscilloscope, the trace in Figure 1-8 is a convenient conversion from time to frequency. Also, note the time scale of the tuning in the figure. The triangle wave that drives the tuning of the laser diode is operated at 10 Hz. Therefore, a single ramp of the diode takes 50 ms. From the spacing shown below, a scan rate of 1.75 GHz/ms can be calculated. Since the laser diode is continuously scanned, some attention must be paid to the rate at which it will change during a plasma event. Typically, plasmas are investigated on the scale of μs . So, by reducing both the numerator and denominator by three orders of magnitude, the laser diode will scan 1.75 MHz/ μs . Recall that the atomic transitions within the plasma from Figure 1-3 are on the order of 4 pm. That corresponds to 15 GHz at 283.305 nm. Therefore, the diode would need to scan for 5,000 μs to reach the half-width of the atomic transition. On the time scale of the plasma formation and evolution, the diode laser can be said to be spectrally stationary.

When operating the dye laser, the wavelength selection corresponds to a physical manipulation of a grating. Such a tuning method is independent of all other instrumental considerations and can be operated asynchronously to all other components. The diode laser tuning is time dependent. Therefore all other timing considerations must defer to the triangle wave driving the piezoelectric tuning arm. For this reason, the delay generator is triggered by the waveform generator output. The ablation laser is

triggered by the same logic as described above. Oscilloscope acquisition cannot be triggered by the excimer output in this scenario. Since the probe laser is continuous in this operation, the acquisition trigger comes from the plasma formation rather than the probe incidence. So, the trigger to the Q-switch of the ablation laser is also sent to the 500 MHz scope. For this preliminary work, no other delays are introduced into the system, and acquisition of absorption data by the PMT is only studied at the onset of the plasma formation.

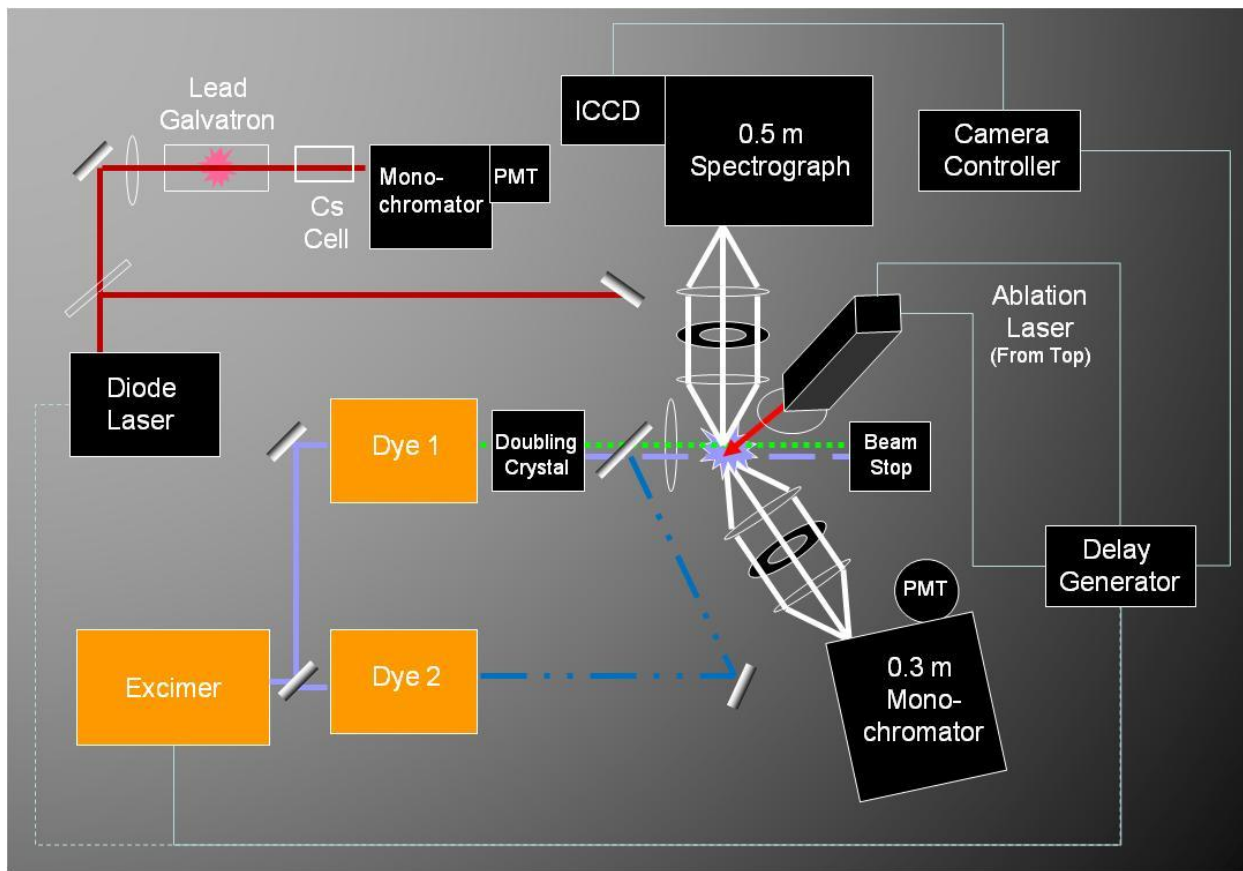


Figure 1-1. General schematic for the proposed instrument.

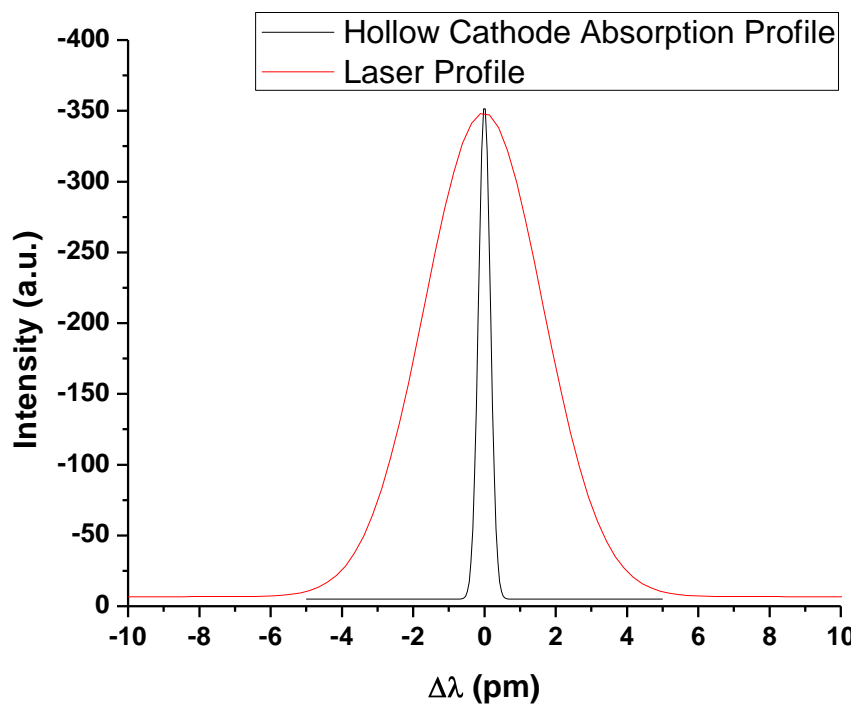


Figure 1-2. Spectral width of dye laser centered at 283.305 nm.

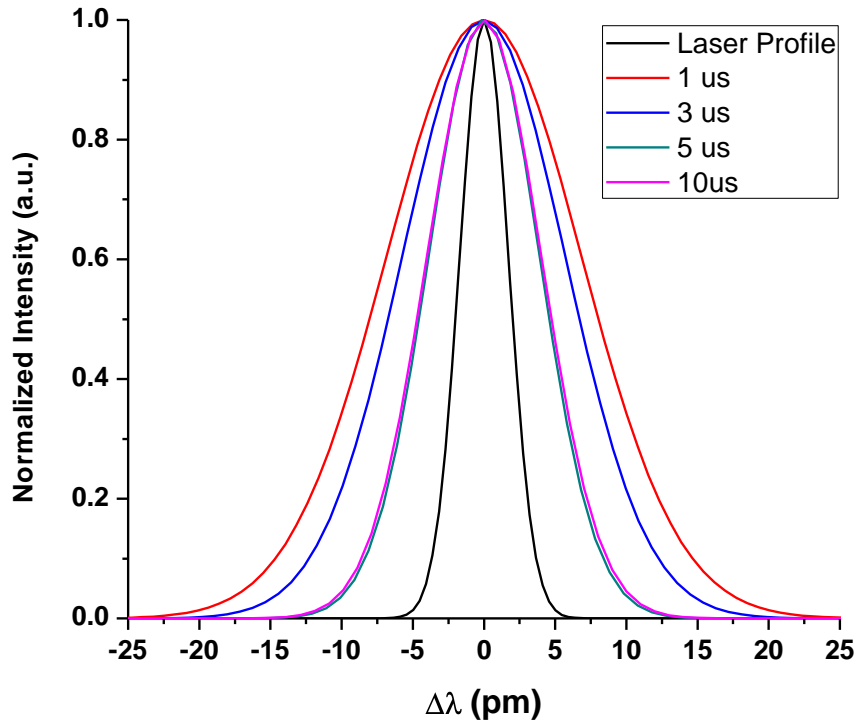


Figure 1-3. Absorption profiles of lead in a LIP at several delays after the plasma formation. Profile shapes are taken by monitoring fluorescence at 405.781 nm while the excitation wavelength is scanned across 283.305 nm.

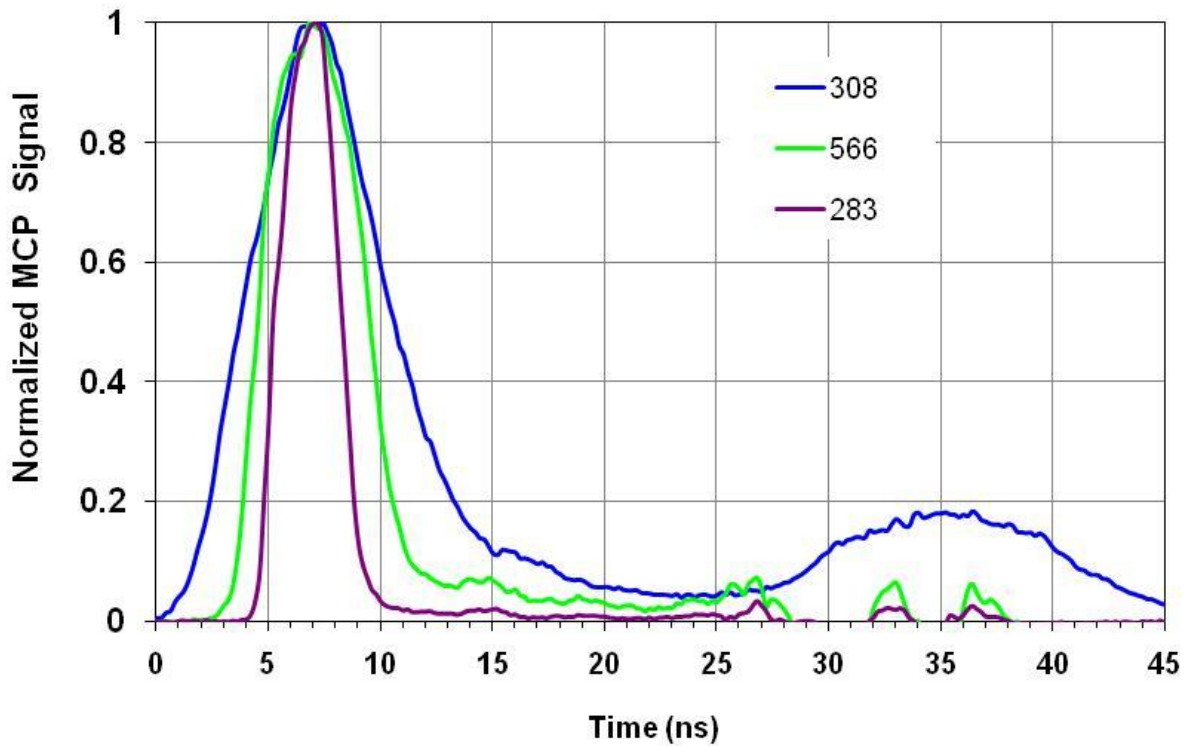


Figure 1-4. Time profiles of the excimer, dye laser, and doubled dye laser pulses.

Table 1-1. Properties of the dye lasers used in this study.

	Exciton Product Name	Peak Lasing Wavelength (nm)	Concentration (mM) in Methanol	Max Pulse Energy (μ J)
Dye Laser 1	Coumarin 540A	550	1	400
Dye Laser 2	Coumarin 450	450	1	600

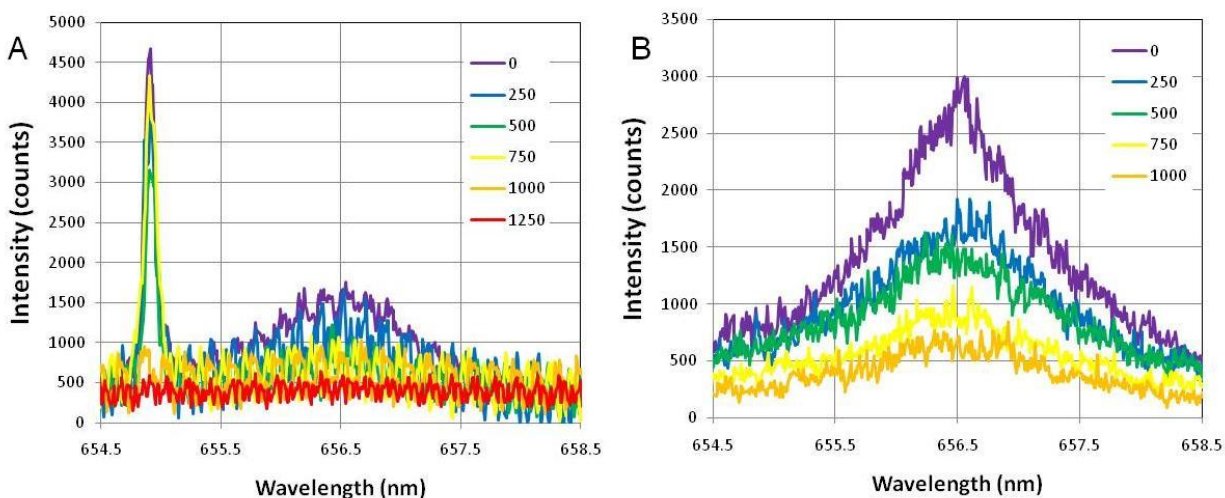


Figure 1-5. Effect of on-chip binning for the CCD. A) Binning within the software. B) Binning on the CCD before readout.

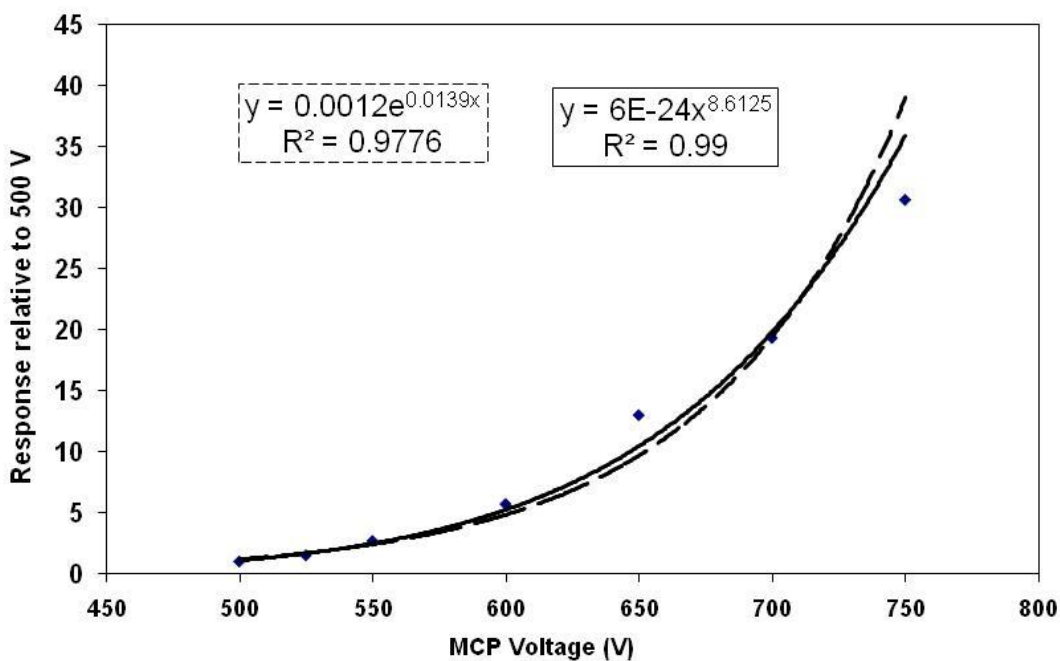


Figure 1-6. MCP response to an LED as a function of applied voltage. Responses normalized to signal at 500 V.

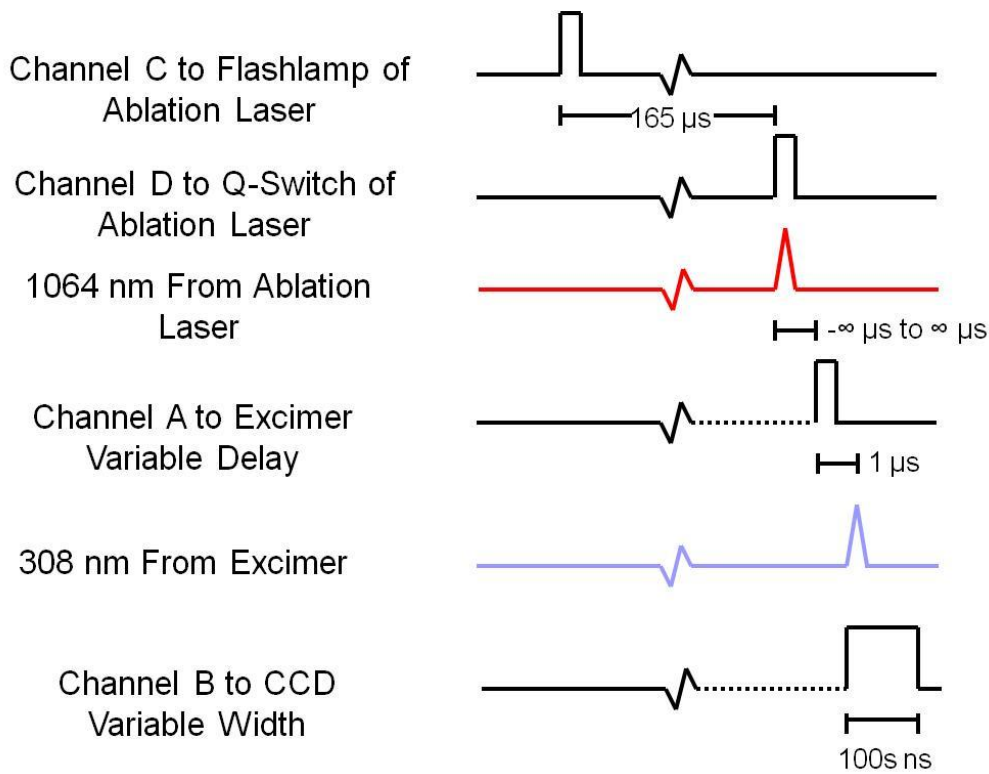


Figure 1-7. Timing schematic for triggers and lasers.

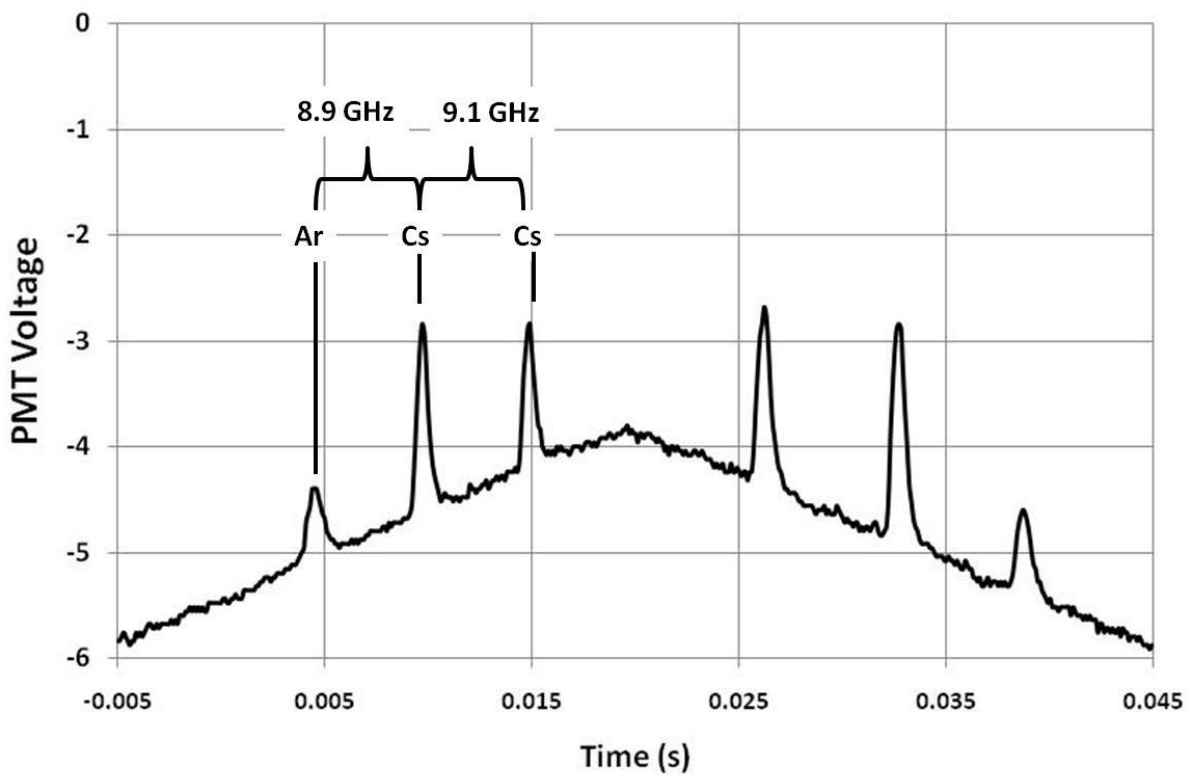


Figure 1-8. Conversion between time and frequency for tuning the diode laser.

CHAPTER 2 SPATIALLY RESOLVED EMISSION

Motivation

When LIPs are simulated, certain symmetries are assumed. Be it cylindrical or spherical, the symmetry of the simulation still requires some basic, radial distribution of temperature, electron number density and analyte number density. In many cases, these are taken to be Gaussian [67, 68], parabolic or flat [69]. To establish if these assumptions hold any water, an emission experiment is devised to evaluate the distributions within the LIP. Additionally, spatially integrating a plasma has been shown to generate apparent temperatures that do not reflect local temperatures [70]. The LIP transitions from a hot center up to 20,000 K to ambient temperature and pressure within a few millimeters. Accordingly, the temperature at any given point within the plasma plume is likely to be very different from a point further from the plasma center. This gradient in temperature affects the atomic and ionic populations and, therefore, the emissive properties of that point within the plasma.

Conventionally, the image of the plasma is formed on the slit such that a horizontal slice is selected out of the image [4, 71, 72]. In this way, an image is formed on an array device that could be parsed into spatially resolved sections [73]. Based on this work, a toroidal and Gaussian distribution have been proposed for neutral atoms and first ions of iron at 3 μs , respectively [70]. For this work, the temperature and electron number density are found to mimic the ionic distribution with peak at the center of the plasma plume. The vertical distribution was also studied and shown to be generally higher in the center of the plume. There appeared to be some bimodal structure to the distribution. At 6 μs , both the atomic and ionic species are measured to share the

toroidal distribution [72]. Additionally, the temperature distribution was found to be generally Gaussian with a flat top at the plasma center.

Since the plasma being imaged onto the slit is an extended source (a source with depth), there are photons imaged onto the slit that may not have come from that vertical section of the plasma. This concern led to the development of a new collection method for the emission spectra. Instead of conventional imaging lenses transmitting the light to the spectrograph slit, two pinholes are used to select a cylinder within the plasma volume. This light is transmitted through a fiber optic cable to the spectrograph. Additionally, a shorter delay time is investigated, 1 μs , in comparison to the work done by Aguilera and Aragon [4].

Temperature and Electron Number Density Considerations

Temperatures presented in this work are calculated using a Saha-Boltzmann plot. This combines the relative distribution of two, neighboring charge states to generate a plot of intensity vs. upper energy level of the transition. The slope of such a construction gives the temperature that produces the described distribution. Certain benefits accompany using this approach, and these along with the mathematic principles are explained here. The construction of a Saha-Boltzmann plot begins with the assumption of a local thermodynamic equilibrium that supports a Boltzmann distribution of atoms within their excited states. Such a distribution is described by

$$n_p = \frac{n_T g_p}{U(T)} e^{-\frac{E_p}{kT}} \quad (2-1)$$

where n_p is the number density (cm^{-3}) of the atoms in state p , n_T is the total number density (cm^{-3}) of the atomic species, g_p is the degeneracy of state p , $U(T)$ is the partition function, E_p is the energy (eV) of state p , k is the Boltzmann constant ($\text{eV}\cdot\text{K}^{-1}$), and T is

the temperature (K) of the plasma [74]. This expression can be combined with the radiant power (W) emitted by the analyte within the plasma given by

$$I = A_{pq} h \nu_{pq} n_p V \quad (2-2)$$

where A_{pq} is the Einstein coefficient for spontaneous emission (Hz), h is Planck's constant (J•s), ν_{pq} is the frequency of the transition (Hz), and V is the volume observed (cm^3) within the plasma. Combining these expressions for number density of analyte in state p with the relation between ν and λ , wavelength (cm), gives

$$\frac{I\lambda}{g_p A_{pq}} = \frac{n_T hcV}{U(T)} e^{-\frac{E_p}{kT}} \quad (2-3)$$

where c is the speed of light (cm/s). Taking the natural logarithm of both sides gives Equation 2-4.

$$\ln\left(\frac{I\lambda}{g_p A_{pq}}\right) = \ln\left(\frac{n_T hcV}{U(T)}\right) - \frac{E}{kT} \quad (2-4)$$

This equation holds the obvious symmetry to $y = mx + b$ which represents a linear relation between x and y . Additionally, this relation is amenable to graphical interpretation of many emission lines of an analyte within a plasma. The slope, which is proportional to the inverse of the temperature, produces a good temperature as it is derived from several emission lines within the source, and the y -axis intercept gives the number density for that emitter.

Using this same logic and the Saha expression for ionization equilibrium, a similar relation can be derived that covers adjacent ionization states [75]. Beginning with the Saha equation

$$\frac{n_e n_i}{n_0} = \frac{2 \left(\frac{\pi m k T}{h^3} \right)^{3/2} U_i(T)}{U_0(T)} e^{-\frac{E_{IP} - \Delta E_{IP}}{kT}} \quad (2-5)$$

where n_0 , n_e and n_i are the neutral, electron and ion number densities, respectively, m is the electron mass (g), E_{IP} is the ionization energy and ΔE_{IP} is the ionization energy depression. A correction factor must be applied to the ionization energy because the Debye length replaces infinity in its calculation. After substituting in Equations 2-1 and 2-2 from above and rearranging, the combined Saha-Boltzmann relation is

$$\frac{I_j}{I_p} = \frac{A_{jk} g_j \lambda_p}{A_{pq} g_p \lambda_j} \frac{2 \left(\frac{\pi m k T}{h^3} \right)^{3/2}}{n_e} e^{-\frac{E_j - E_p + E_{IP} - \Delta E_{IP}}{kT}} \quad (2-6)$$

where the transition from $p \rightarrow q$ is atomic and the transition from $j \rightarrow k$ is ionic. Taking the natural logarithm of both sides after some rearrangements gives

$$\ln \left(\frac{I_j \lambda_j}{A_{jk} g_j} \right) - \ln \left(\frac{I_p \lambda_p}{A_{pq} g_p} \right) = \ln \left(\frac{2 \left(\frac{\pi m k T}{h^3} \right)^{3/2}}{n_e} \right) - \frac{E_j - E_p + E_{IP} - \Delta E_{IP}}{kT} \quad (2-7)$$

The execution of this relationship is more sophisticated than the simple Boltzmann plot as knowledge is required of the electron number density within the observed plasma region. Again, the slope of the plot gives the temperature of the plasma, but as can be seen from the derivation, the relation holds only when comparing ion to neutral emission intensities. However, this allows for a much larger spread in upper state energies which increases the accuracy of the temperature. Since the plasma easily ionizes metal vapor, several ionic lines appear in the spectra collected for this study. So, to facilitate the evaluation of temperature from Saha-Boltzmann plots, the spectrograph is scanned over nine spectral windows that contain both atomic and first ionic lines of several elements. The nine windows used are listed in Table 2-2 along with the relevant lines within each.

One of these windows covers the emission of the hydrogen alpha line at 656.279 nm. This line is very convenient for the evaluation of electron number density via Stark broadening [76]. Part of the reason that hydrogen lines have found such popularity in electron number density calculations is their linear Stark effect [65, 77-79]. Because of its simple electronic structure, hydrogen's electron has a much more simple interaction with the free electrons that induce the Stark broadening used in the calculation. More complex atoms depend quadratically on the distance of the free electron, while the limit to the interaction between a free electron and hydrogen can be taken as the Debye length within the plasma [65]. Additionally, the quadratic Stark effect is asymmetric, making interpretation more complicated. For this work, the equation proposed by Griem and reproduced as Equation 2-8 is used along with the constants calculated from theoretical hydrogen line profiles [80].

$$n_e = C \left(\frac{1}{T} \right)^{3/2} \lambda^3 \quad (2-8)$$

Clearly, this is not the optimal position in which to be. The Saha-Boltzmann plot depends on knowledge of the electron number density and the electron number density calculation depends on knowledge of the temperature, the constant C being dependent upon both. Fortunately, the dependence upon these two values is weak. For instance, an initial guess of 10,000 K and 10^{17} cm^{-3} for temperature and electron number density, respectively, generate a C of $3.61 \times 10^{15} \text{ \AA}^{-3/2} \text{ cm}^{-3}$. If the temperature is changed to 20,000 K, C changes to 3.88×10^{15} , and, if electron number density had been changed to 10^{18} cm^{-3} , C becomes $3.23 \times 10^{15} \text{ \AA}^{-3/2} \text{ cm}^{-3}$. This weak dependence makes the first assumption less critical, and the value of $3.61 \times 10^{15} \text{ \AA}^{-3/2} \text{ cm}^{-3}$ is typically used as it is derived from common LIP properties.

Experimental

A 200 μm pinhole is mounted 210 mm in front of a fiber optical cable. The fiber optic cable is a bundle of 19 fibers with an individual diameter of 200 μm . The bundle has a diameter of 1.3 mm. Finally, the plasma is positioned 8 mm away from the front aperture. This is all summarized in Figure 2-1A. From these figures, some simple trigonometry gives what will be referred to as the angle of acceptance. This angle is the largest that would be accepted into the optical train and be detected. For a lens, this angle is easily calculated from the $f/\#$, the inverse tangent of the aperture radius divided by the focal length. The two pinhole system has no real focus, but there is still an angle described by the relation of the two apertures. Tracing a line from the bottom of the fiber optic cable entrance to the top of the pinhole, an angle is defined that describes how much light is detected from undesired sections of the extended source. So, a direct comparison between these two angles (for the lens and the two aperture setup) gives an idea of how selective the collections methods are. For the optical train described above and shown in Figure 2-1B, an $f/7$ lens used with the spectrograph has an angle of acceptance of 0.0714 radians as measured from the optical axis. The two aperture system described above has an angle of acceptance of 0.0036 radians. Obviously, the two aperture setup is more discriminating than a conventional lens collection.

Given these parameters, it is possible to calculate the diameter of the cylinder whose emission is accepted into the fiber optic cable. This diameter is strongly dependent on the distance between the front pinhole and the observed volume. The distance used here is 8 mm. At this separation, the angle of acceptance added an additional 56 μm to the diameter of the observed region. Therefore, at the center of the

plasma, the diameter of the observed area is 256 μm . Assuming the plasma had cylindrical symmetry with a diameter of 2 mm, the diameter of the observed area at the front and back of the plasma is also calculated as 250 μm and 264 μm , respectively. This plasma size is taken from previous work done by Benoit Lauly of the Winefordner research group [66]. Taking these values into consideration, the two aperture collection system is moved in steps of 250 μm . An electronically controlled x-y-z stage (Encoder Mike Controller 18011, Oriel) is used to precisely scan the apertures over the profile of the plasma. Once the first aperture is positioned the set distance away from the plasma, the electronic stage is stepped by 250 μm in the x-z plane according to the raster depicted in Figure 2-2. Such steps sizes are well within the stage's limitations as the motors driving each axis are capable of 10 μm steps.

The central point of the plasma, corresponding to point 0x0 in the diagram of the raster is determined by a two-step process. For the z axis, a Helium Neon laser is mounted behind the two-aperture system. The fiber optic cable is removed and the laser beam passed through the fiber mount to the front, 200 μm aperture. The laser is moved vertically, along with the two-aperture system, until the beam grazes the surface of the sample and a clear diffraction pattern is visible on the other side. This diffraction pattern results from passing the laser beam through the restricting aperture. The x axis zero is determined by placing the fiber optic cable back into the mount within the two aperture system. While observing plasma emission at 1 μs , the spectrograph is set to 0-order. By scanning the apertures horizontally, the most intense point along the axis is taken to be the plasma center. This reference point is stored as 0x0 within the electronic controller of the x-y-z stage.

The 19 individual fibers are subsequently lined up in a slit for the exit of the fiber. The f-number of these fibers is matched to the SP500 used in this work. The spectrograph slit is opened to transmit the entire fiber slit. Effectively, a 200 μm entrance slit is used. By selecting such a small region for observation, the ICCD requires an integration time of 500 ns to accumulate adequate signal. A delay time of 1 μs is used to coincide with other data planned to be taken. The spectra are binned on chip and 300 laser shots are collected for each spectral window at each spatial point. A fresh sample surface is presented to be analyzed for each group of 300 spectra. An aluminum standard, D33, is used with a well-known composition listed in Table 2-1.

Taking this known composition, nine spectral windows are selected because they contain atomic and ionic emission lines to be used for the constructions of Saha-Boltzmann plots within a program developed as a calibration-free methodology for LIBS, LIBS++ software first described by Ciucci [81, 82]. The central idea of the CF-LIBS software is to generate Saha-Boltzmann plots for several different elements with strong emissivities within the plasma. From these plots, a reliable plasma temperature can be derived. The software generates Saha-Boltzmann plots for every element with identified lines within the spectrum provided. During the final analysis, certain temperatures can be ignored if too few lines are identified or misidentified. This is the case for manganese and iron, respectively. Manganese had too few lines and many lines identified as iron were likely other elements. Therefore, the temperatures presented here only consider the Al, Si and Mg lines identified within the nine windows collected.

Results

The raster used in the collection of spectra for this work is limited to one half of the plasma profile. Because of concerns over day-to-day reproducibility, a single raster is completed in one day, restricting the profile collection to one half. Therefore, the collection began at 0x0 and moved toward the edge of the plasma. In this way, cylindrical symmetry is assumed and the behavior on the maps shown below is extrapolated to the other side.

For each point in space, a spectrum is pieced together from the nine spectral windows observed, generating a temperature and electron number density for each point. These are mapped out within the two-dimensional grid that defines the two-aperture raster. The temperature map in Figure 2-3 shows a hot center 500 μm above the sample at 1.28 eV which corresponds to 14900 K. The local temperature near the surface is consistently about 1500 K below the temperature at $z = 250 \mu\text{m}$. This depression of temperature agrees with the maps produced by Aguilera and Aragon [4]. Additionally, they observe a lack of symmetry within the distribution of temperature at atmospheric pressure. The observed time window is slightly later than that used here, but the trends are certainly similar.

Figure 2-4 shows that the electron number densities are more sporadic in their distribution. Like the temperatures, the density near the surface is consistently lower than the rest of the plume, again observed by Aguilera [4]. Additionally, both properties share an apparent hot spot in the top right corner. It is very possible that the plasma does not maintain cylindrical symmetry as the shape of the plasma depends on the laser beam profile [83]. Since the beam profile was not known during this work, it is assumed that this consistent displacement of temperature and electron number density

results from a real structure within the plasma plume. This asymmetric form likely results from the beam profile as each spatial point is collected at a different point on the sample surface. While the sample surface can affect the propagation of the plasma, this should not be so structured and repeatable as is observed in the images [84].

The temperatures mapped above come from line intensities generated by the CF-LIBS software. These integrated line intensities are easily extracted to map the emission intensity of the major and minor components. For illustration, two major component are mapped, Al at 85% and Si at 9%, as well as a minor component, Mg at 0.04%. At this delay, 1 μ s, the ionic distributions seem to follow the conventional idea of the plasma plume, a mushroom cloud. The two major components, Al and Si, track each other very well in Figures 2-5B and 2-6B, with a very similar structure in their relative emission maps. The lower concentration magnesium ion, shown in Figure 2-7B, shows a much more even spread of intensity over the profile of the plasma. The three elements, aluminum, silicon and magnesium, have very moderate ionization potentials, 6.0, 8.2 and 7.4 eV, respectively. Despite the 2 eV difference between silicon and aluminum, their relative intensities map very well which reflects that no new ionization is occurring at this delay. Additionally, the temperature map shows that the predicted temperatures are well below those necessary to affect that change in ionization state.

The atomic populations show the same correlation as the ionic. Aluminum and silicon agree in their distribution about the center of the plasma plume in Figures 2-5A and 2-6A, respectively. All three species exhibit a much higher density near the surface of the sample. Again, this agrees well with the temperature distribution which has its

lowest values just near the surface. These arguments agree that the plume has the mushroom cloud shape with the cold vapor filling in underneath the rising hot vapor.

Conclusions

While much more spatially selective than imaging, the experimental setup suffered from a limited spectral interrogation. Each spectral region required so many laser shots, that practical limitations on sample size and interrogation time inhibit the investigation. An obvious improvement to the setup would be the use of an echelle spectrometer. With such a spectrograph, the CF-LIBS functionality could be used to full potential by collecting an entire spectrum for each spatial position. By removing the need to stitch together spectral windows, the number of plasmas required for the raster is reduced by orders of magnitude. Additionally, at these short delays, the plasma is evolving very quickly. A 500 ns gate width on the ICCD could cause some of the spatial resolution to be lost as the plasma expands through the observation volume. The solution to this issue is be the addition of an ICCD with more sensitivity than the present model used. With a higher sensitivity, a short gate width would be possible. This would increase the temporal resolution which is tied to the spatial resolution when the plasma plume is expanding at these short delays. Despite the practical limitations of the setup, good agreement is observed with previous imaging work done to map temperature and electron number density [4].

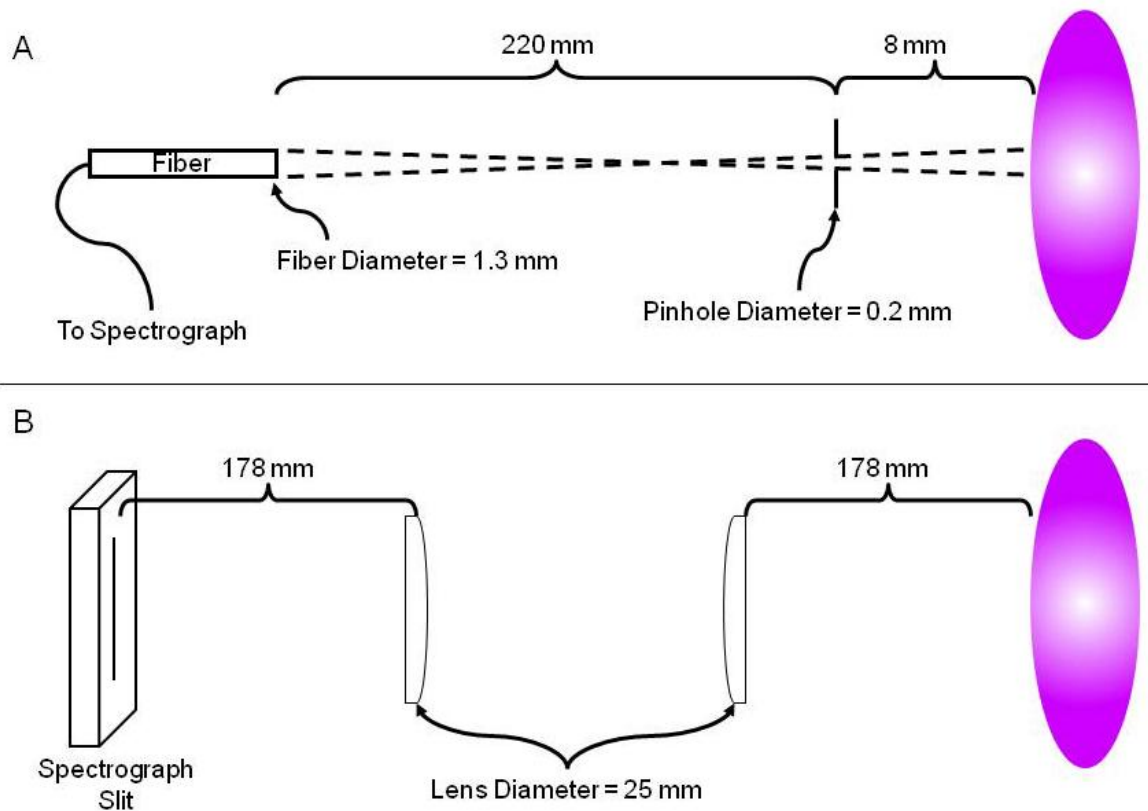


Figure 2-1. Trigonometry for optical emission collection. A) For the two-aperture system proposed. B) For the conventional lens collection.

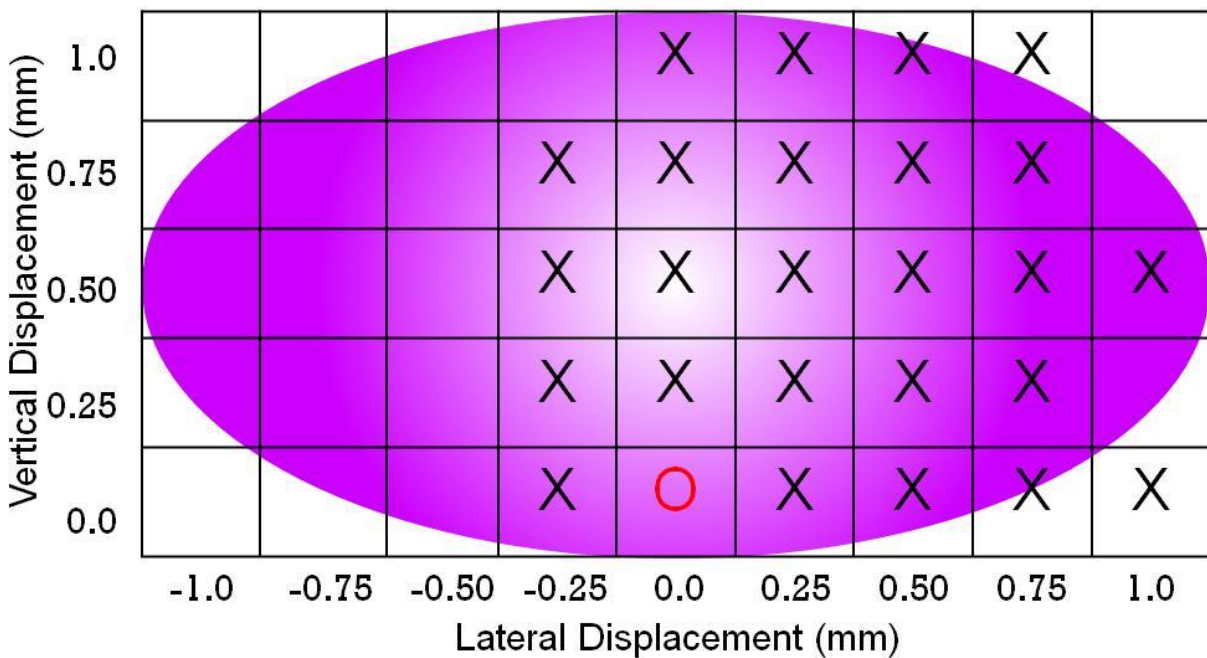


Figure 2-2. Diagram of raster across the plasma profile.

Table 2-1. Composition of the D33 aluminum alloy used in this study in mass percent.

<u>Element</u>	<u>Percent Composition</u>
Al	84.92
Si	8.54
Cu	2.89
Fe	1.15
Zn	0.59
Ni	0.5
Mn	0.4
Pb	0.14
Ti	0.055
Sn	0.048
Cr	0.047
Mg	0.038

Table 2-2. Central wavelengths for the nine spectral windows used in this study along with the relevant lines and associated spectroscopic quantities.

Central Wavelength (nm)	Emission Wavelength (nm)	Emission Species	E_k (cm ⁻¹)	A_{ki} (x10 ⁸ s ⁻¹)
263.0	258.588	Fe II	38660.04	0.810
	259.373	Mn II	38543.08	2.680
	259.940	Fe II	38458.98	2.200
	260.569	Mn II	38366.18	2.700
	261.187	Fe II	38660.04	1.100
	261.382	Fe II	39109.31	2.000
	261.801	Fe I	45913.49	0.400
	262.567	Fe II	38458.98	0.340
	262.829	Fe II	39013.21	0.860
	263.132	Fe II	38660.04	0.600
	265.248	Al I	37689.41	0.133
	266.039	Al I	37689.41	0.264
	277.930	Fe II	62322.43	0.760
	278.369	Fe II	62083.11	0.700
281.5	279.553	Mg II	35760.88	2.600
	279.827	Mn I	35725.85	3.600
	280.270	Mg II	35669.31	2.600
	281.619	Al II	95350.60	3.830
	283.951	Fe II	79439.47	0.990
	285.213	Mg I	35051.27	4.910
	302.063	Fe I	33095.94	0.402
	305.007	Al I	61843.54	0.321
	305.468	Al I	61747.56	0.449
	305.714	Al I	61843.54	0.750
303.0	306.429	Al I	61691.46	0.820
	306.602	Mn I	49888.01	0.160
	324.725	Cu I	30783.69	1.370
	327.376	Cu I	30535.30	1.361
325.0	356.537	Fe I	35767.56	0.380
	360.0	Al II	123423.40	2.496
360.0	361.876	Fe I	35611.62	0.730
	385.637	Fe I	26339.69	0.046
	385.991	Fe I	25899.99	0.097
388.0	386.259	Si II	81191.34	0.280
	390.068	Al II	85481.35	0.005
	390.552	Si I	40991.88	0.118
466.0	466.368	Al II	106920.56	0.530
656.5	656.279	H I	97492.30	0.441

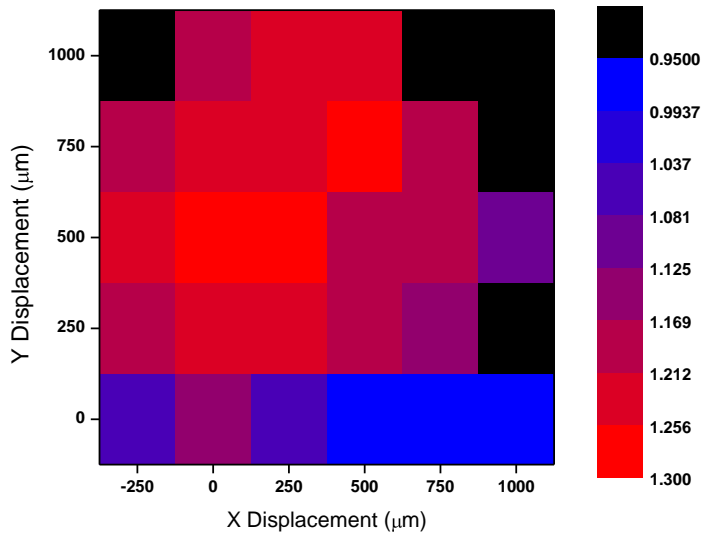


Figure 2-3. Map of the T determined from the Saha-Boltzmann plot in CF-LIBS. Note that the scale is eV.

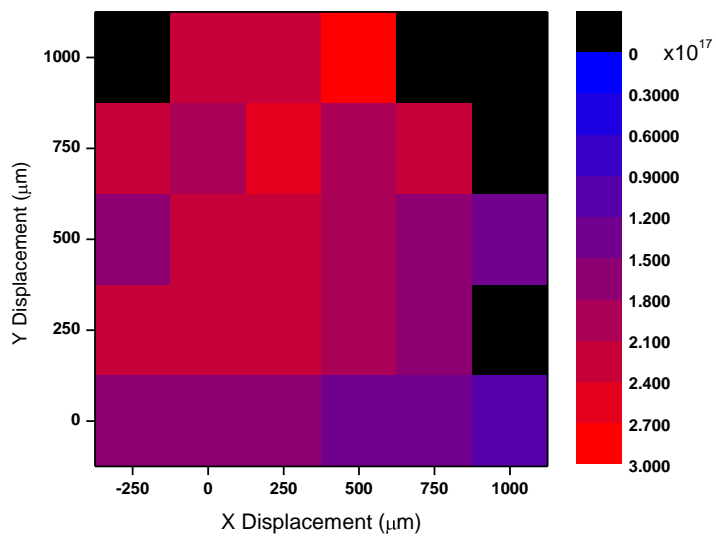


Figure 2-4. Map of the electron number density from the fitting of the H-alpha emission line. Note that the scale is $\times 10^{17} \text{ cm}^{-3}$.

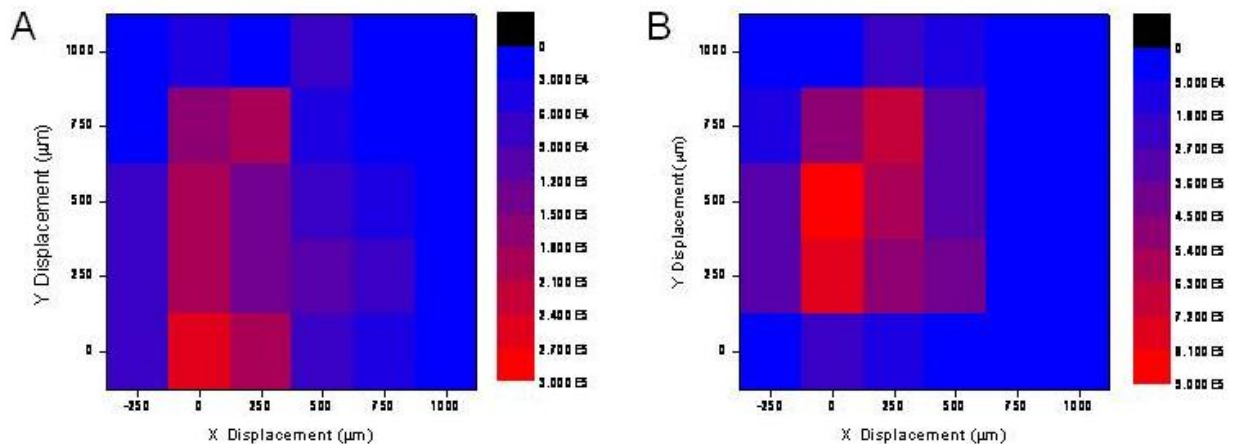


Figure 2-5. Maps of the aluminum distribution within the plasma. A) Atom. B) Ion. Both scales show integrated line intensity in counts.

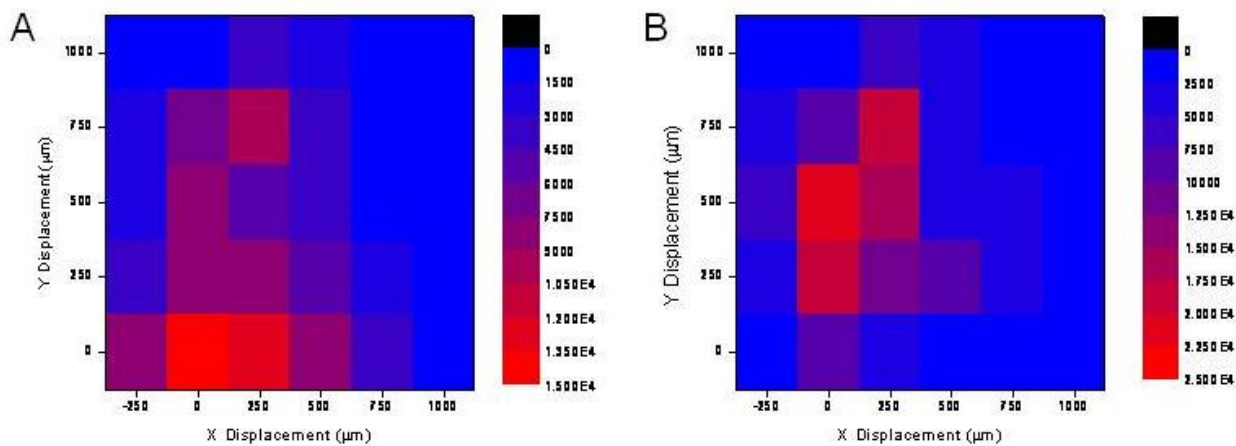


Figure 2-6. Maps of the silicon distribution within the plasma. A) Atom. B) Ion. Both scales show integrated line intensity in counts.

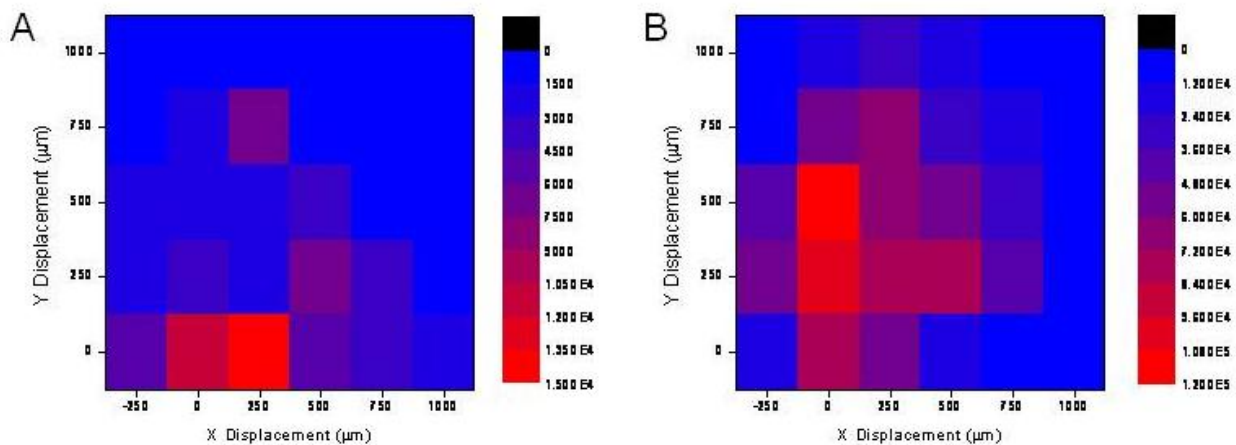


Figure 2-7. Maps of the magnesium distribution within the plasma. A) Atom. B) Ion. Both scales show integrated line intensity in counts.

CHAPTER 3 SCHLIEREN IMAGING

Motivation

Another important check for any simulation of a LIP in atmosphere is the formation and propagation of the shockwave. This effect is generally omitted for early theoretical work done in vacuum [85, 86], but ambient gas properties become significant at atmospheric pressure [87]. This significance holds for both the ablation process [88, 89] and the excitation process within the plasma [3]. At these higher pressures, the sudden formation of a plasma on the sample surface creates a shockwave that is readily measured optically. For simulations of atmospheric breakdown, this is an easy check for agreement with experimental results.

The measurement of shock fronts is much older than the advent of the LIP. Accordingly, there are many well defined methods for imaging the phenomenon [90, 91]. The two main camps are shadowgraphy and schlieren. Experimentally, these two techniques are very similar, siblings. However, there are some fundamental differences in their sensitivity that clearly discriminate them. Shadowgraphy is sensitive to the second derivative of the refractive index with respect to space while schlieren is sensitive to the first. Additionally, the experimental application of schlieren requires the addition of a cut-off within the system. This requirement will be explained more. Clearly, schlieren is a more sensitive technique as it responds to smaller gradients, however, the gradients found within shockwaves are large enough that they lend themselves very well to shadowgraphy [92].

Within the LIBS community, shadowgraphy and variants therein are more common than schlieren applications. The most basic form of shadowgraphy, unfocused, has

been used to calculate shock velocities, plume temperatures and electron number densities and the behavior of shockwaves within a cavity [84, 93, 94]. A focused shadowgram images a plane some millimeters in front of the perturber. This technique has been used to acquire sharper shadowgrams of shock waves under different atmospheres [95, 96]. Shadowgraphy also shares quite a bit with interference techniques. It is essentially one arm of a two-beam interferometer. This logic has been used for papers that study both number densities and shockwave expansion with the same setup. The shadowgrams are acquired by blocking the reference arm of the interferometer. Michelson interferometers have been used by Schittenhelm and Vogel [97, 98], and Mach-Zehnder interferometers have been used more recently by Sobral, Hauer and Thiyagarajan [99-101].

Schlieren applications are more difficult to come by as many times the author still refers to the method as shadowgraphy [102, 103]. Despite this common confusion, there are still some applications using schlieren to investigate LIBS [104-106]. Cristoforetti investigated the pre-ablation scheme of double-pulsed LIBS using schlieren to study the coupling of the two plasmas and shockwaves [105]. Vogel conducted a fundamental study of schlieren cutoff techniques for the imaging of laser ablation on tissues. These schlieren images have the highest contrast and resolution of any LIBS application to date [106].

With all of the evidence that an imaging system can give useful insight into the LIP, it is desired to apply this method to this multidisciplinary setup. However, the schlieren system should not interfere with the regular workings of the emission and fluorescence setups. Therefore, a design for the schlieren system is attempted that

leaves the emission optics untouched. Only two optical elements and a probe laser are introduced. Once the technique was refined, the probe laser was removed and a dye laser used for LIF served as the probe laser, eliminating the extra instrumentation.

Premise of Schlieren Imaging

Schlieren imaging is a technique that can measure the density gradient of some perturbing volume when interrogated with collimated light. Practically, the angle of deflection for a refracted beam of light is directly proportional to the gradient of refractive index within the perturber. These two physical properties, density and refractive index, can be easily related for gases by

$$n - 1 = k_{GD}\rho \quad (3-1)$$

where n is the refractive index, ρ is the gas density and k_{GD} is the Gladstone-Dale coefficient. For air at standard temperature and pressure, k_{GD} is $0.23 \text{ cm}^3\text{g}^{-1}$ for visible wavelengths [92]. The refractive index change measured is a result of the density change that originates, in this case, from a laser induced plasma.

To better describe the phenomenon, begin by defining a three-dimensional frame of reference where z is axis of propagation of the light, parallel to the geometric beam of light. The x and y axes are, then, the horizontal and vertical axes perpendicular to the direction of travel for the light beam. In one dimension, if there exists a gradient in the refractive index $\delta n/\delta x$, then the angle of refraction for any light beams interacting with that point in space is defined by

$$\varepsilon_x = \frac{L}{n_0} \frac{\delta n}{\delta x} \quad (3-2)$$

where ϵ is the angle of refraction, L is the width of the perturbation along the optical axis and n_0 is the refractive index of the surroundings. A similar equation holds for the y axis. So density disturbances must be in the plane perpendicular to the optical axis. Any refractive index gradients along the optical axis do not affect the beam in this way.

There are two, basic classifications of schlieren systems, lens and mirror. For both systems, the fundamental concept is the same, but their implementations differ. The obvious appeal of a mirror system is its freedom from chromatic aberrations and large scale applicability. Many executions of this technique have used flash lamps that produce a short, continuum pulse of white light to be used as the light source for interrogation. Chromatic aberration within a schlieren system can fundamentally undermine that instrumentation as will be shown later. Also, large telescope mirrors are much easier to procure for schlieren imaging on the human scale. Lens systems suffer from the aforementioned chromatic aberration, but they are much easier to setup and align than their mirror counterparts. Additionally, for the application described in this work, a schlieren imaging system with lenses is very similar to certain emission collection optics. Accordingly, a lens system is assembled for this work as there are simple ways to circumvent the chromatic aberration issue.

A lens schlieren system is summarized in Figure 3-1 and begins with the light source being collimated by a lens. In a perfect world, this light source would be a point source. However, as that is a difficult approximation to make for most lamps, a point source can be improvised by imaging the lamp onto a pinhole. The light from that pinhole can, then, be collimated by the first lens within the schlieren system. Next, position the perturbing volume within the collimated light from the source and position a

focusing lens for the collimated light. This second lens also acts as a collimator for the light that is refracted by the perturbing source. Accordingly, it should be placed 1 focal distance away from the perturbing volume. Once the source light has been focused behind the second lens, a cutoff is introduced to block either the refracted light that is now collimated or the focused light from the source. Here, chromatic aberration from a continuum source can cause problems. If the cutoff is to be placed to block the focused source light, that position is ambiguous for white light. A final lens forms an image of the collimated, refracted light on the detector.

The cutoff mentioned is the most important aspect of the optical train for schlieren imaging. Depending on the light source, there are many forms the cutoff can take. Typically, the cutoff edge needs to be perpendicular to the angle of refraction for the light. To describe it in more detail, imagine a cylindrical lens that will refract light in one direction while leaving the light undisturbed in the perpendicular axis. Now, the lens is oriented with its cylindrical axis vertically, which causes a beam of light that passes through it to be dispersed horizontally. If a cutoff is to be introduced as a horizontal knife edge, the vertical displacement of the knife edge would cut off the same amount of intensity regardless of the cylindrical lens existence. However, if the knife edge is mounted vertically, the intensity it blocks with each horizontal displacement varies strongly with the presence of the cylindrical lens. So, for the knife edge to be effective, the direction of displacement needs to be perpendicular to the edge of the cutoff. This is the major factor that decides the structure of the light source and cutoff in schlieren measurements. The relation between the source and cutoff determines whether the refracted light or unperturbed light is imaged, dark field or bright field, respectively.

To appreciate the difference between the two fields of imaging, bright and dark, Figure 3-2 compares the cutoffs used in each technique with respect to the mask applied to the light source. Bright field imaging will allow the unperturbed light to pass on to the detector. With the described optical train, an image of the source mask should be made at the location of the cutoff. Without any perturbing density gradient, this is true. Therefore, a cutoff that matches the source mask should only pass light that is unaffected by any density change, and the bright regions of the image plane will correspond to portions without significant density gradient. On the other hand, the dark field cutoffs in Figure 3-2 will only allow all other light to pass. Light that remains unchanged will hit the dark field cutoff. Only light refracted by the perturbing density gradient will pass on to the detector. So, the bright portions of the image will correspond to the density gradient perturbing the collimated light.

In the present work, there is no source image for the collimated light as its source is a laser beam. The image formed at the focus of the first lens is, simply, a point focus. Accordingly, for this work, the cutoff is, generally, a pinpoint for dark field and an iris for bright field. This is also fortuitous for the structure of the perturbing plasma. As the shockwave is a hemisphere, light is displaced at all angles away from the sample surface instead of linearly as in the cylindrical lens proposed above. Therefore, a pinpoint cutoff for dark field imaging allows the refracted light at all angles around the hemisphere to be imaged. The only exception is the light that is displaced toward the mount of the pinpoint. To illustrate this point, a horizontally mounted pinpoint is moved about the focus of the unperturbed laser light. Figure 3-3 shows the transition from dark field to bright field schlieren imaging. As mentioned previously, the light refracted

laterally, hits the pinpoint and its mount. There are two dark regions on either side of the shockwave image where this is absorbed. Alternately, Figure 3-4 shows the transition from bright field to dark field imaging by moving that same pinpoint vertically into the focus of the unperturbed light.

Sedov-Taylor Blast Wave

Point explosions have been well studied since the 1940s, and the first experimental data used to check the theoretical expansion of a strong shock wave into atmospheric conditions were from nuclear test explosions [107]. Since this early work on atomic bombs, Sedov-Taylor blast wave studies have been done on phenomena as large as supernovae remnants and as small as LIPs. For those studying and modeling LIP's, the Sedov-Taylor model is useful in describing the density and temperature profiles behind the shockwave as well as its motion through space [104]. For the present work, the aspect of most concern within this model is the expansion speed of the shock wave. This relation, given by

$$R = \left[\left(\frac{75}{16\pi} \frac{\gamma - 1}{3\gamma - 1} \right) \frac{E}{\rho_0} \right]^{\frac{1}{5}} t^{\frac{2}{5}} \quad (3-3)$$

where R is the radius of the shockwave, γ is the specific heat ratio, E is the energy deposited, ρ_0 is the density of the surrounding gas and t is time. If γ is taken to be 1.3, as is commonly assumed, the constant becomes 0.96 [108]. So, any work done to measure the shockwave using a schlieren setup should show three relations: The radius should grow as a power function of exponent 0.4 with respect to time; the radius should grow as a power function of exponent 0.2 with respect to deposited energy; and

the radius should decay as a power function of -0.2 with respect to the density of the surrounding gas.

Experimental

Successful schlieren images are collected in two ways. Both setups used the BigSky Ultra for the formation of the LIP, DG535 for timing and the SP500 set to 0-order. Schlieren images are detected by the ICCD coupled to the spectrograph. In this configuration, the spectrograph becomes a glorified turning mirror for the imaging laser, and a bandpass filter is required to spectrally select the imaging laser and reject plasma emission. The collection lenses for conventional emission and fluorescence studies remain in their same configuration. A cutoff is placed at the focus of the first lens, the collimating lens near the plasma source. The cutoff in this experiment is simply a hex wrench mounted such that the tip of the wrench blocked the focused probe beam. A micrometer controlled x-y-z stage enabled the cutoff to be moved into and out of the focus to optimize the schlieren images.

The first iteration of this work was completed along with the spatially resolved emission measurements described above. The motivation for this is to have two sets of data that corresponded to the same laser pulse energy, sample irradiance, temperatures and electron number densities. Therefore, the expansion of the shockwave measured correlates exactly to the plasmas that generate the emission profiles. A nitrogen laser is triggered by the delay generator such that the delay between the plasma formation and the probe laser is very well controlled. The timing jitter on the nitrogen laser output is 75 ns. Accordingly, the gate width of 100 ns for the ICCD is wider than the jitter expected from the probe laser. Jitter in the probe laser also necessitated single shot measurements. No averaging is done to generate the

schlieren images, so each image came from a single LIP. The probe laser beam is large enough that no beam expander is necessary for it to interact completely with the plasma shockwave. Here the laser replaces the source and the first two lenses shown in Figure 3-1. As their sole purpose is to form a cylinder of collimated light, the laser is an adequate replacement for those first few optical components. The simplified optical setup for the present schlieren imaging is illustrated in Figure 3-5.

In the second iteration, the coumarin 450 dye laser is used as the probe laser. With the change in wavelength from the 337 nm nitrogen laser, a bandpass for 460 nm is installed in place of the 337 nm bandpass. As the dye laser is tunable over this range, the central wavelength is scanned to the maximum transmission of the bandpass filter at 460 nm. Since the dye laser is pumped by the excimer, the dye laser output suffers from the same fluctuations as the excimer. The jitter quoted previously, 50 ns, for the excimer required a trick for the timing. For the nitrogen laser, the delay displayed on the DG535 is taken as the time difference. However, this is not the best solution when using an excimer as the probe. To account for this, an extra measurement is taken simultaneously by the monochromator equipped with the PMT. The monochromator is set to the wavelength of the dye laser output. Then, the PMT voltage is monitored on an oscilloscope during each image collection. The plasma formation is indicated on the PMT voltage trace by the spectrally ubiquitous continuum, and scatter from the probe laser appears as a second peak. It is a small thing to measure the delay between these two pulses on the PMT voltage trace. So, for each schlieren image taken of an individual LIP, a measured delay is recorded. These delays are used to construct the curves of growth for the shockwave. Additionally, a slit cutoff

is introduced in place of the pinpoint cutoff used previously. The slit is mounted horizontally which allows for light refracted towards the sample surface to be imaged. In this configuration, the top of the shockwave is very clearly imaged for measuring its displacement from the sample surface.

Results

Time Dependence

First, the time expansion of a shockwave is verified using the schlieren setup. A LIP is formed with the ablating laser set to 69 mJ/pulse. The time between the plasma formation and probe laser is varied from 50 ns to 6 μ s. The distance travelled by the shockwave is measured from the sample surface to the top of the shockwave normal to the surface. A single pixel column is selected for measurement, and the shockwave peak or dip is recorded for that pixel column. The peak or dip depends on the use of dark field or bright field imaging. Figure 3-6 shows a typical image used in the bright field configuration. The red circle highlights the dip in intensity that marks the shockwave. Using these measured values along with the delay time, a curve is constructed.

Figure 3-7 shows the time evolution of a shockwave created by a laser power of 69 mJ/pulse under atmospheric conditions. Clearly the general trend is acceptable with respect to the growth of the shockwave, but the exponent is too large to agree with theory. The power of 0.45 should be at 0.4 for a perfect marriage to the Sedov-Taylor blast wave theory. However, there is evidence that the shockwave from a LIP does not exactly mimic this theory [109]. Rather, the exponent of time should be larger, ~ 0.42 in the work by Wen.

As can be seen from Figure 3-6, this first experiment is done using the bright field arrangement. To confirm that the choice of field would not affect the expansion measured with the schlieren technique, another set of images are collected in dark field. Figure 3-8 shows a typical dark field image with the intensity peak of the shockwave highlighted by the red circle. The work done in dark field, in Figure 3-9, shows the same time dependence as that done in bright field. In fact, the data overlap when plotted together as can be seen from their fitted trendline equations.

Energy Dependence

The second dependence investigated is the relation with deposited energy. From Equation 3-3, it is apparent that the radius of the shockwave should grow as a power function of exponent 0.2. This relation holds only if the delay is fixed at a value. Therefore, the delay chosen must be large enough that the jitter within the probe laser is less significant while remaining small enough that the shockwave is easily measured on the CCD. A delay of 1 μs is chosen, and the actual delays of the schlieren images are recorded in the event that scaling is necessary. Figure 3-10 shows the proper growth with respect to deposited energy, but the theoretical scaling disagrees at low energies. This behavior was also reported by Callies [104]. Pulse energies that approach the breakdown threshold have a significant fraction of their energy deposited before the plasma formation, or breakdown. Because this energy deposition occurs before the plasma formation, and subsequent shock wave formation, it is lost to sample heating. For the present experimental setup, no plasma formation occurred for a pulse energy of 5.7 mJ/pulse. Therefore, the threshold lies between 5.2 and 9.7 mJ/pulse.

Density Dependence

The third relation expressed in Equation 3-3 lies between radius and surrounding gas density. To examine this more closely, the sample is placed within a gas chamber capable of a modest vacuum, 5 mbar. No positive pressure work is completed in this study. As the other parameters need to be constant for this work, a delay is set to 1 μ s with a pulse energy of 40 mJ/pulse. At this pulse energy, Figure 3-10 shows a good agreement with the scalar predicted by the Sedov-Taylor relation.

From Figure 3-11, there is good agreement between the observed shockwave radius except at the lowest pressure. It appears that the shockwave at 50 mbar is moving faster than the predicted value for this density. If a trendline is fit to the data, the power exponent is 0.23 rather than 0.2. So, it is possible that this is simple experimental error, or there is some more physical reasoning. There are two other variables held constant for this calculation. Time, most certainly, is not drifting in such a way as to cause this disagreement. As stated in the last section, the breakdown threshold can affect the actual energy deposited which could cause an apparent divergence from theory. If the energy deposited were to increase relative to higher pressures, then the shockwave could travel farther than predicted for the data point at 50 mbar. However, it has been shown that for nanosecond laser pulses at 1064 nm, the breakdown threshold slightly increases with a decrease in pressure [110]. This would contradict the reasoning above, as less energy would contribute to the point explosion. Perhaps this trend could be more accurately explained if more data points were collected at lower pressures, below 50 mbar. Unfortunately, the density gradients at these lower pressures are more difficult for the schlieren system to detect as their absolute magnitudes are being reduced. Because of this, the images of the shockwave

collected below 50 mbar do not show a distinct shockwave boundary. Any distance measurement done in this regime would be guesswork and subject to extreme error.

It was stated previously that schlieren imaging is a more sensitive method directly proportional to $\delta n/\delta x$, and a schlieren system should be capable of imaging even at these lower pressures [102]. Therefore, it is proposed that this inability to detect shockwaves below 50 mbar is the result of the optical train used to capture the schlieren image. For a lens type schlieren system, the sensitivity is directly proportional to the focal length of what is the first imaging lens in my setup. This lens is the third lens in the optical train from Figure 3-1.

$$S = \frac{dC}{d\varepsilon} = \frac{f}{a} \quad (3-4)$$

Here, S is the contrast sensitivity, $dC/d\varepsilon$ is the rate of change of contrast with respect to refraction angle and a is the height of the source image. Simple trigonometry shows that a longer focal length lens in this position of the optical train results in a greater overall displacement from the optical axis for the refracted beams. Therefore, measurement of smaller angles of refraction is possible with the same cutoff.

Conclusions

A simple, lens-type schlieren system is superimposed over a conventional optical emission setup. Successful schlieren imaging is possible without deconstructing any aspect of the emission collection optics or any alteration to the instrumentation. The only changes made to the optical train are the addition of a cutoff and bandpass filter for the probe laser. These components are easily removed to resume the normal operation of emission spectroscopy. The schlieren images of LIP shockwaves agree with the Sedov-Taylor expansion and the modifications found in the literature.

The system could be improved with longer focal length collection optics and a higher resolution CCD detector. Conventional schlieren systems do not use scientific cameras as the time resolutions comes from the probe laser delay. Additionally, the intensification of the CCD image introduces losses to the resolution. However, these two alterations would affect the emission studies done with the system and are not implemented. Using the system as is, a future project could scan the cutoff in the plane that contains the focused source image. Knowing the optical geometry of the refracted ray collection, a density map could be constructed by measuring the intensity of the refracted beams as a function of displacement from the optical axis. This displacement, assuming the light is well collimated, could generate the angle of refraction which gives the gradient of the index of refraction for that point. By building a map of these angles, a density distribution could be integrated.

If changes were to be made to the schlieren system such that the optical emission setup is to be interrupted, a future investigation using this technique and the process described above to reconstruct density distributions could be done for a magnified image of the plume projected on to a CCD detector. This would give very good insight into the structure of a LIP.

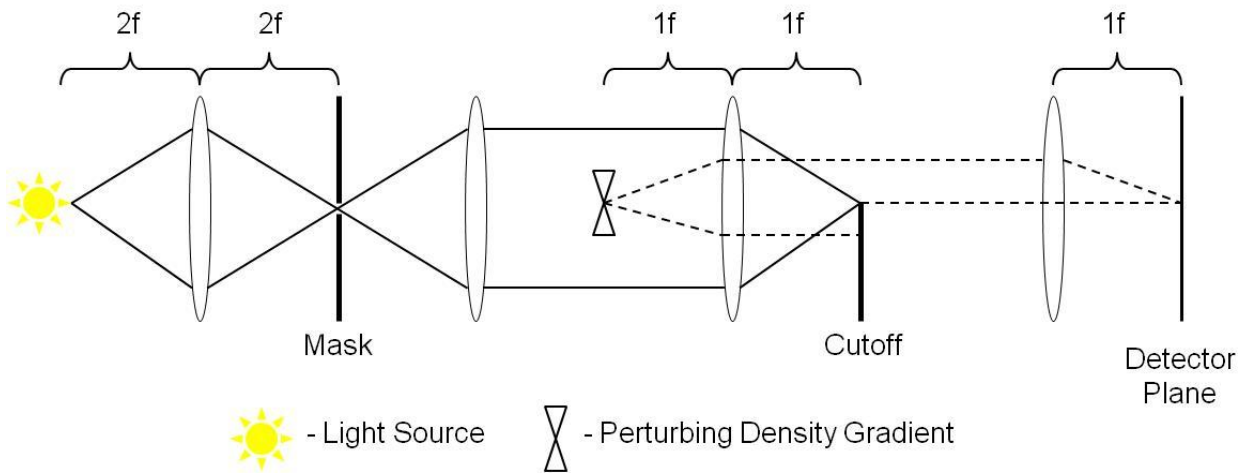


Figure 3-1. Schematic for a generic lens schlieren system working in the dark field.

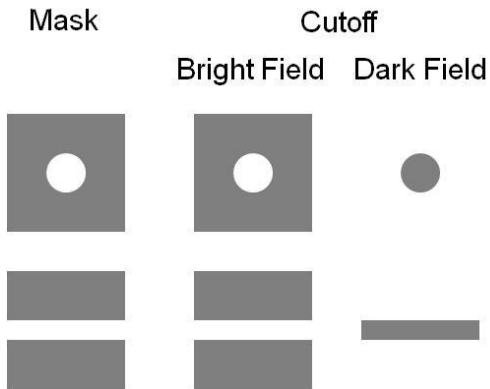


Figure 3-2. Comparison between bright and dark field cutoffs for schlieren imaging.

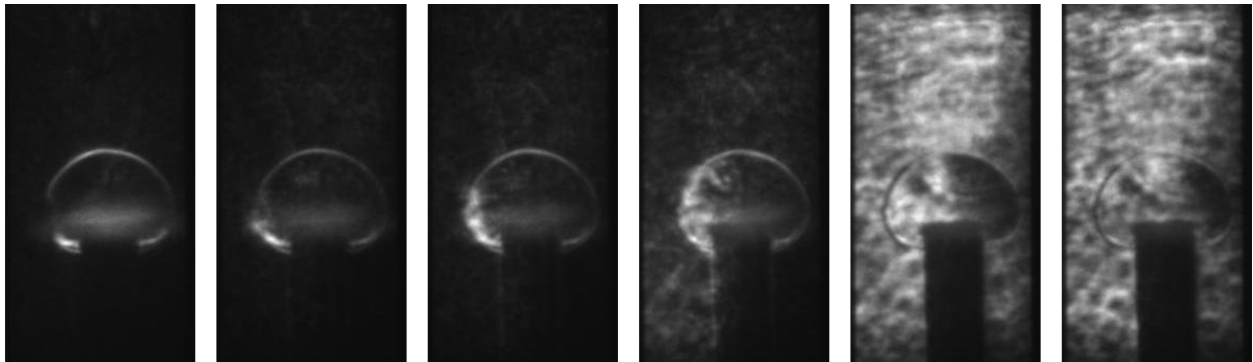


Figure 3-3. Progression from dark to bright field schlieren by moving a horizontally oriented pinpoint cutoff horizontally.

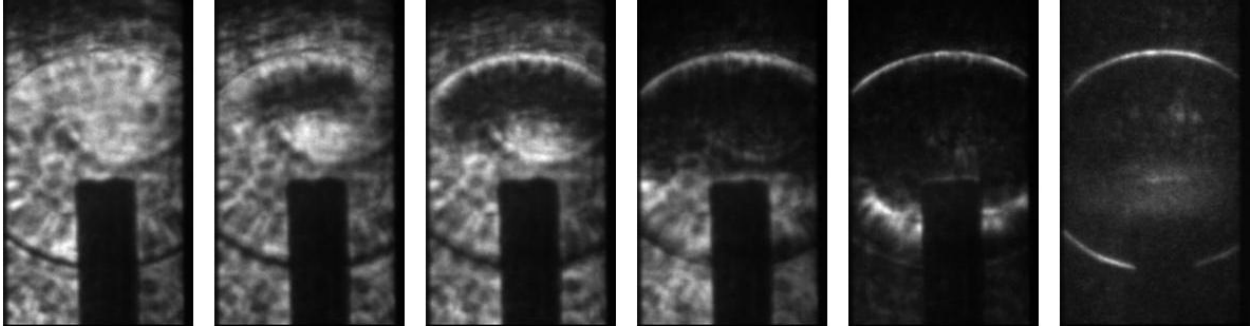


Figure 3-4. Progression from bright to dark field schlieren by moving a horizontally oriented pinpoint cutoff vertically.

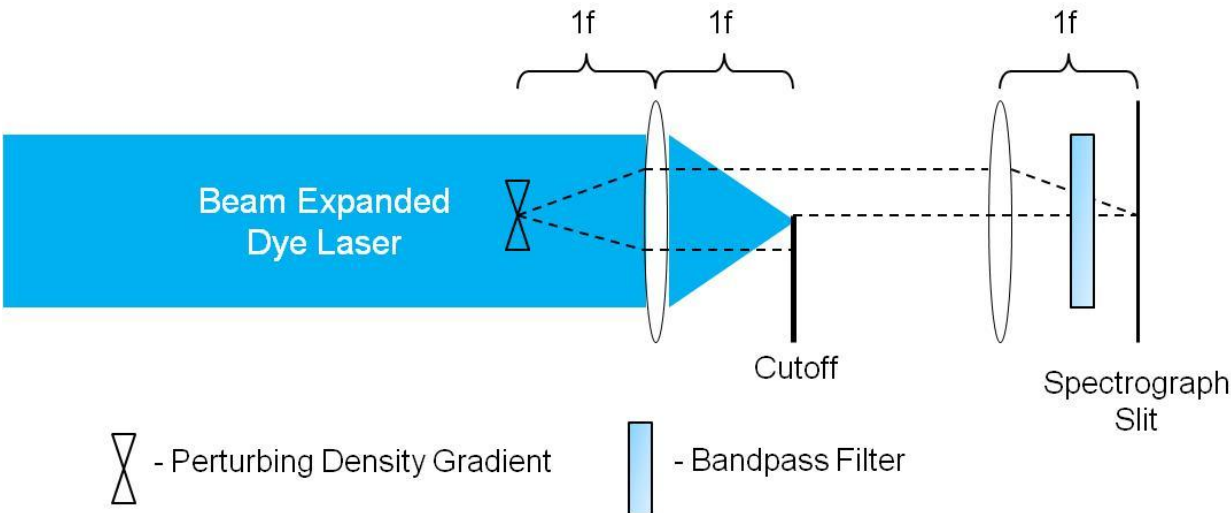


Figure 3-5. Schematic for the optics used in the schlieren imaging for this work.

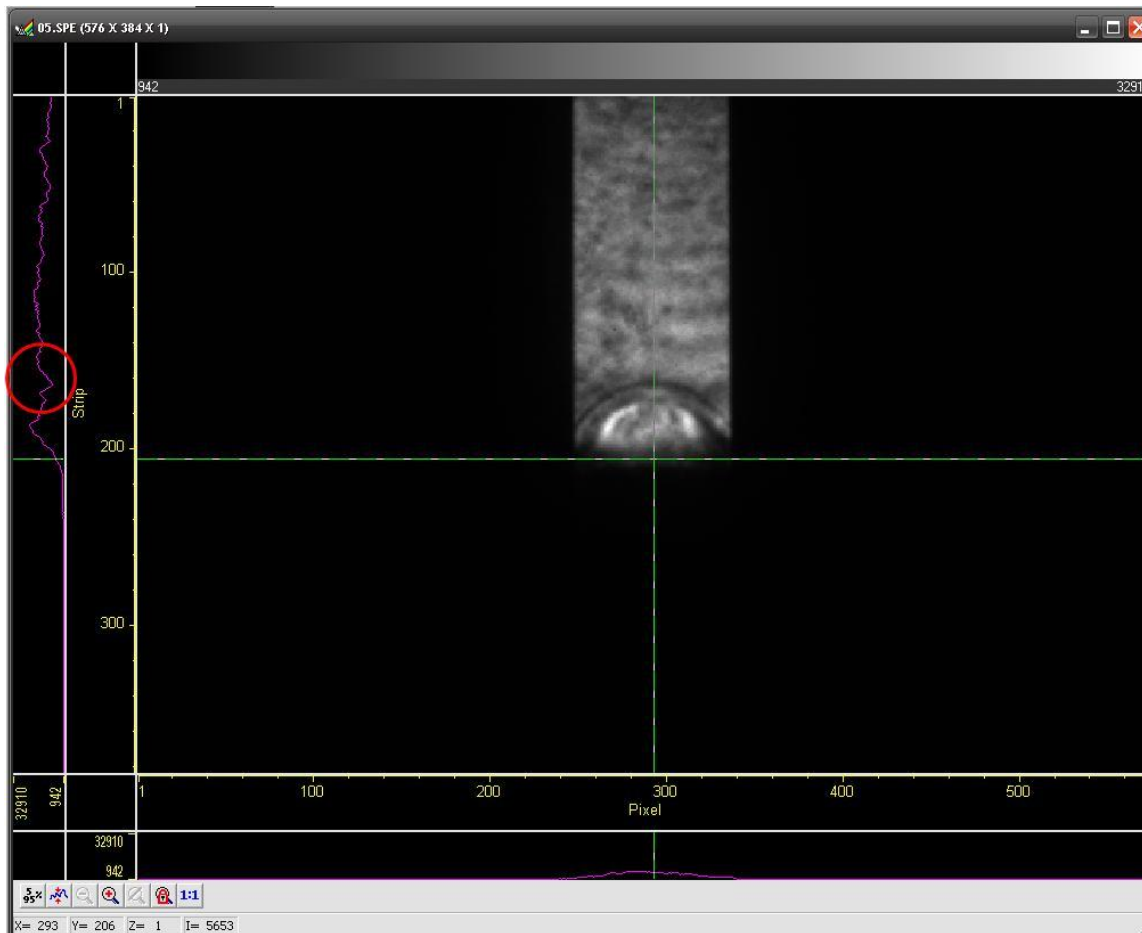


Figure 3-6. Image taken from WinSpec32 for measuring the propagation of the shockwave by bright field schlieren imaging. The red circle indicates the reduction of intensity by refraction.

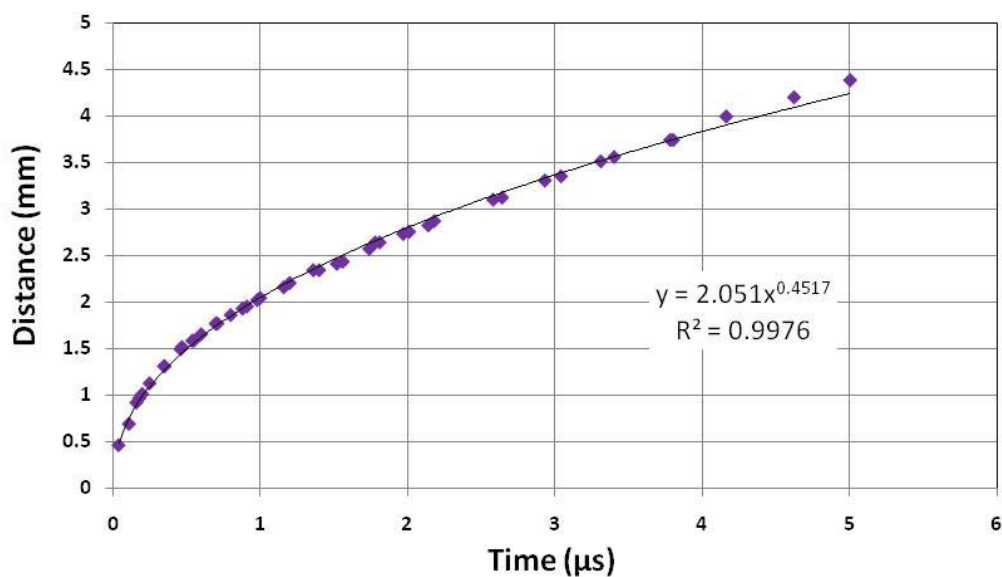


Figure 3-7. Shockwave expansion by bright field from a LIP formed with 69 mJ/pulse.

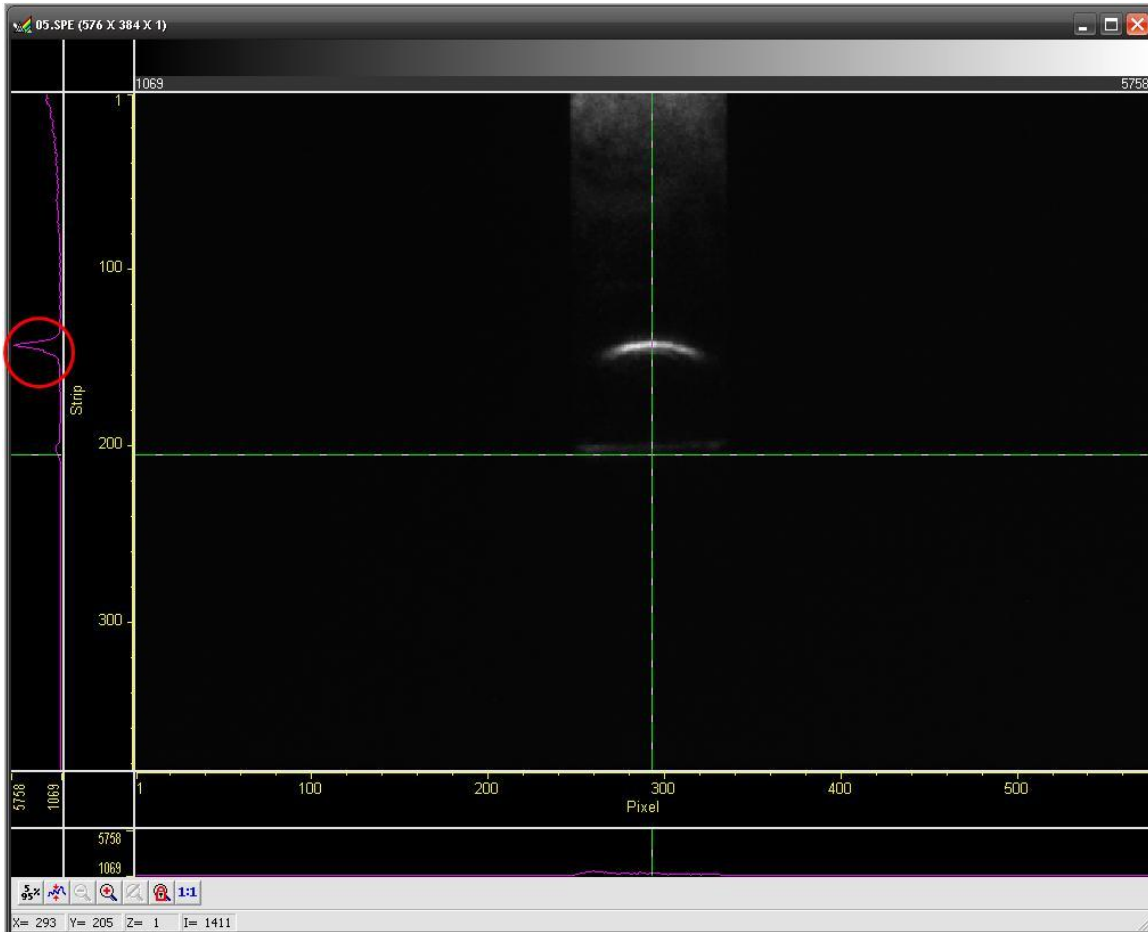


Figure 3-8. Image taken from WinSpec32 for measuring the propagation of the shockwave by dark field schlieren imaging. The red circle indicates the increase of intensity by refraction.

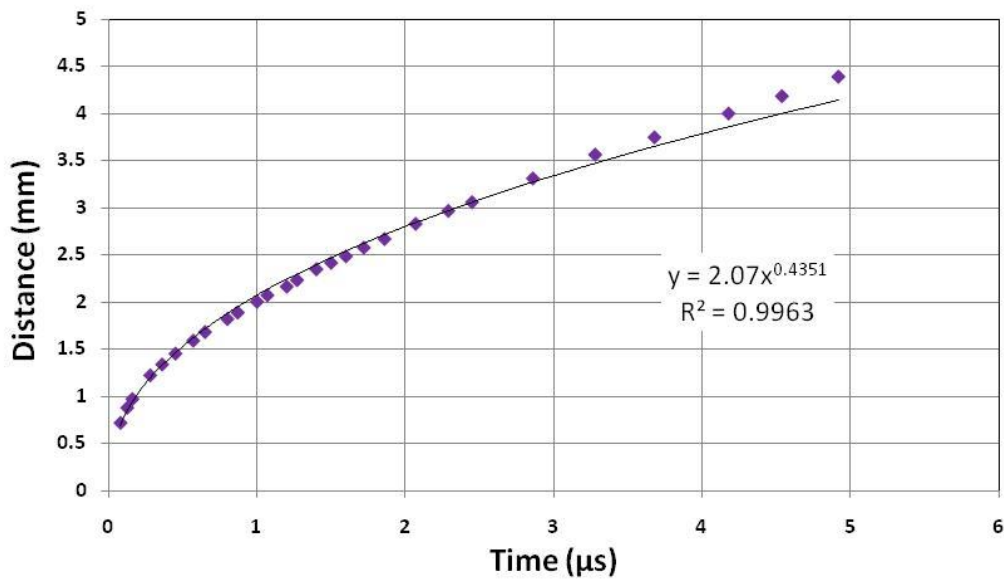


Figure 3-9. Shockwave expansion by dark field from a LIP formed with 69 mJ/pulse.

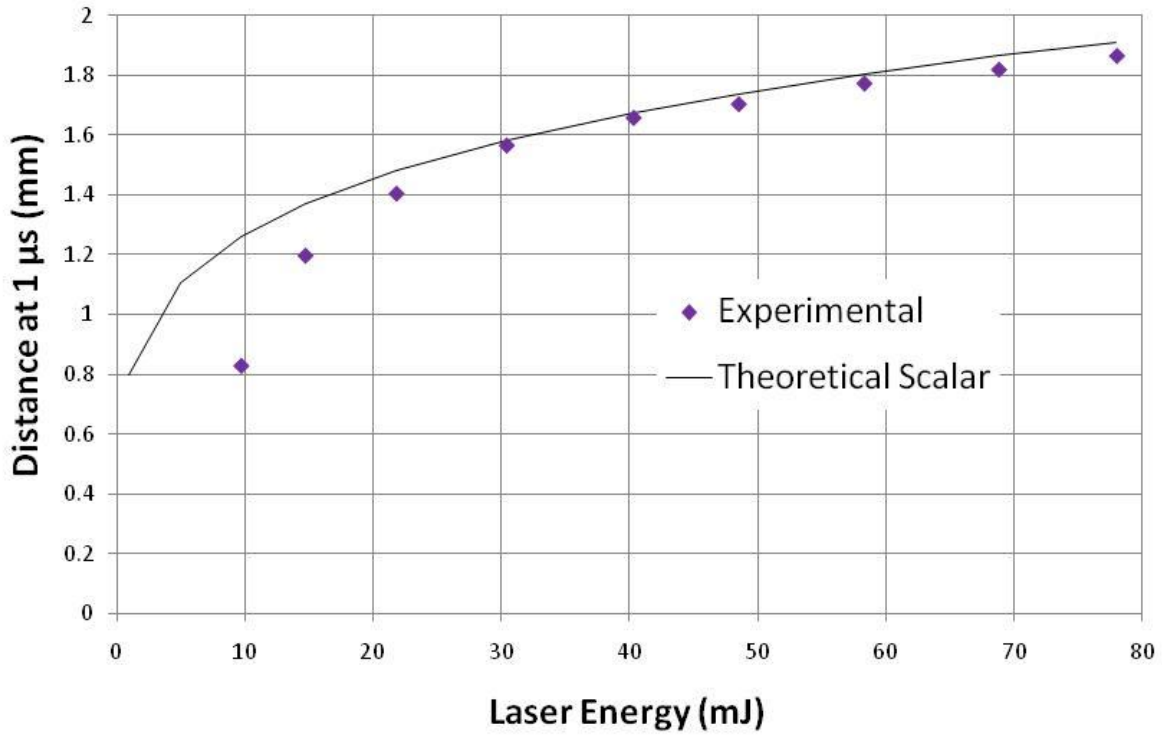


Figure 3-10. Energy dependence of the shockwave produced by a LIP at atmospheric pressure.

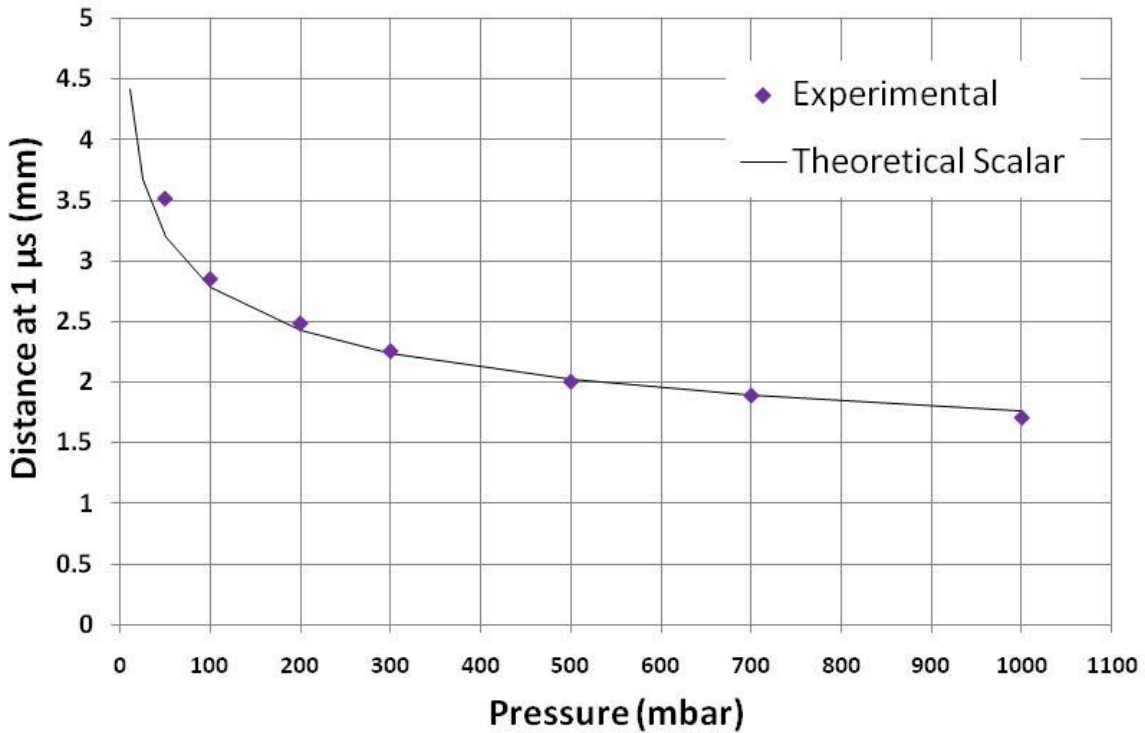


Figure 3-11. Density dependence of the shockwave produced by a LIP at 49 mJ/pulse.

CHAPTER 4 SPATIALLY RESOLVED LASER-INDUCED FLUORESCENCE

Motivation

While mapping emission intensities is a very straightforward method of investigating analyte distributions, it only interrogates the excited states. Following Boltzmann's distribution, at 8000 K, the population is about 0.13% for an excited state with degeneracy of 3 and a resonant emission in the blue, 450 nm. In many cases, transitions begin at an even higher energy level such as $35,000\text{ cm}^{-1}$. Maintaining the degeneracy and atomic identity, for the partition function [111], the population of this excited state falls to 0.012%. Considering there are other levels also populated according to the thermal distribution, the ground state will still have an order of magnitude higher density than excited states. Therefore, it behooves the investigator to probe the ground state as well. There are two attacks for that sort of investigation. First, it is possible to measure the absorbance of an incident light source. A fraction of the light is absorbed and represents the density of analyte within the probed volume. In some cases, this absorption will result in the excitation of an emissive excited state. With the appropriate magnitude of spontaneous emission coefficient, the fluorescence from that level is informative in the same way. The magnitude of the fluorescence also represents the density of analyte. From a signal-to-noise perspective, the fluorescence is a more attractive signal as it is possible to conduct the investigation with minimal background given the right conditions. However, absorption is more widely applicable as it does not require the transition to be emissive. Ultimately, fluorescence is chosen for this investigation for its easy comparison to thermal emission and its freedom from artifacts induced by refraction.

As was discussed earlier, the application of LIF to LIBS is executed in the late 1970s. The combined method LIBS-LIF was known as TABLASER [33]. At that time, it was used to construct working curves for impurities in foodstuffs [10]. In the 1980s the technique began its function as a diagnostic for LIP [31, 37, 112]. By 1990, Planar LIF (PLIF) was established as a spatially resolved diagnostic tool within LIPs. These applications applied to atoms [39-41, 113], ions [114, 115], radicals [116] and oxides [41, 117]. As an alternative to the spatial resolution given by imaging a plane of excitation, time-of-flight measurements can be conducted at a set height. The time varying signal of fluorescence for a given position has been used to study the distribution of atoms [42-44, 118-120] and oxides [43] in LIPs.

In accordance with the overall goal of this project, the method of data collection for the spatially resolved LIF needs to be compatible with the existing setup. The ICCD is already coupled to the spectrograph for other emission work. Decoupling the detector from the spectrograph requires significant calibration when the two are subsequently reunited. It would be possible to configure the detection system in much the same way as the schlieren imaging. Unfortunately, this significantly limits the species available for investigation by fluorescence as the bandpass filter needs to be customized to the fluorescence wavelength. Therefore, the configuration for this work is a sort of hybrid between the two historical methods described. Essentially, the volume observed is much like a time-of-flight measurement. It remains fixed in space and observes the changes in time. Like the PLIF experiments referenced above, the detector still retains a spatial dimension. The fluorescence is resolved spectrally, but the second dimension of the ICCD detector resolves either vertical or horizontal distributions. Also, like the

PLIF experiments, the excitation is not a point source. In this way, the detection scheme is easily customizable to any analyte with a strong fluorescence in the visible or ultra-violet regions.

In conjunction with the spatially resolved emission measurements described earlier in this document, the spatially resolved fluorescence measurements aim to investigate the distribution of atom and ion species within the plasma plume. Complimentary to the earlier work, the fluorescence measurement can map the unexcited lower level populations of the analyte. Additionally, the experiment does not stop with the cooling of the plasma. While emission measurements are contingent upon this point, fluorescence investigations can continue well after the plasma temperature falls. This means that the fate of the atoms and ions produced by the plasma formation can be determined even if they cease to emit.

Experimental

Laser-induced fluorescence measurements are made within a LIP. The formation of the plasma is consistent with the previous sections of this document. A Nd:YAG laser operating at the fundamental wavelength of 1064 nm with a pulse width of 7 ns forms the plasma. Tunable dye lasers are introduced at 90° with respect to the incident ablation laser and collection optics. With this geometry, the probe laser illuminates the plasma from the side. The extent of the probed volume depends on the focusing optics of the dye laser. Two foci are used; a conventional plano-convex lens generates a point focus and a cylindrical lens generates a plane of excitation. For spatially resolved work, the cylindrical lens excitation is the obvious choice as it enables simultaneous acquisition of fluorescence from every height within the plasma. A point focus would limit the vertical range of fluorescence within the plasma.

Two excitation schemes are used in this project. First, atomic distributions of lead are studied in a plasma generated on a multi-component glass (SRM 1412, NIST) that contains 4.4% lead by mass. To interrogate lead atoms, an excitation at 283.305 nm probes the direct line fluorescence at 405.781 nm. Second, ionic distributions of barium are studied in a plasma generated on an 'ancient' glass (Brill C, Corning) with 11% barium by mass. Excitation is at 455.403 nm and direct line fluorescence is monitored at 614.171 nm.

The delay between the ablation pulse and fluorescence pulse is varied from 500 ns up to 30 μ s. Fluorescence detection for this project is accomplished with the spectrograph equipped with an ICCD. The plasma is imaged onto the slit such that a vertical slice is spectrally resolved for detection by the camera. When horizontal slices of the plasma are imaged, a glass dove prism is introduced into the optical train at 45°. Such an orientation turns the image of the plasma 90°. Therefore, a horizontal slice of plasma is selected. Again, as the jitter in the timing of the probe pulse limits the accuracy of the delay, the ICCD gate is set to a wide 100 ns. As there is some variability with the dye laser intensity, 49 spectra are collected and averaged to generate a single fluorescence image. This averaging is done by manipulating the data in software. No on-chip accumulations are used. Additional post-processing is necessary as the time-integrated measurements did not distinguish between thermal emission and fluorescence. To remedy this issue, emission spectra are taken and averaged in the same manner for each delay. The two signal magnitudes are then subtracted to generate the fluorescence intensity.

As stated above, the end result is an array with spectral resolution in the x-axis and vertical resolution in the y-axis. The entire intensity could be integrated over the vertical range or parsed into smaller regions. Binning the entire vertical limits of the plasma at each delay generates a trend for the plasma on the whole. By selecting smaller regions of the image to be binned, the spatial distribution of the analyte can be deduced. This second assertion relies on the assumption of saturation. Any variation of a fluorescence intensity in the vertical axis could result from a real analyte density change or a difference in probe laser fluence. A thorough check of this assumption would require the testing and construction of a saturation curve where the fluorescence intensity is measured as the excitation fluence is varied over several orders of magnitude. This process is approximated by measuring the fluorescence intensity with and without a neutral density filter of optical density 0.3. Such an optical density would half the excitation fluence which would half any linear fluorescence that resulted. If the excitation is strong enough such that saturation is achieved, the fluorescence intensity would remain unchanged and the fluorescence would accurately represent the analyte density. This behavior is checked for the fluorescence studies in lieu of the construction of an entire saturation curve.

The selection to be binned is determined from images at early and late stages of the plasma evolution. The vertical extent of the plume examined in this study is summarized by Figure 4-1. Emission at an early delay is juxtaposed with the fluorescence later in the plasma expansion. An integration height is set to 140 pixels which corresponded to 3.22 mm. When studying the plasma plume as a whole, the entire 140 pixel region is summed. Ten pixel segments are binned for vertical resolution

which results in 14 spatial points. Each point covers 230 μm . Figure 4-2 shows how the emission and fluorescence images are parsed relative to the emission at 0.5 μs . Parsing is done in the LabVIEW environment using a virtual instrument written in lab. The front panel of the program is shown in Figure 4-3. Two functions are served by this program. First, the region of interest (ROI) can be refined using the images which are shown before and after ROI selection. Secondly, it bins the data from each of the 50 frames and outputs the intensity versus wavelength for convenient treatment in a spreadsheet. It is more economical to take whole images of the plasma and electronically divide the data later. Experimentally, it is feasible to collect each vertically binned region by resetting the ROI and collecting all new spectra, however, this strategy would consume much more sample and time.

Results

Atomic Fluorescence

Before the investigation into the spatial distribution of atomic lead within the plasma, the integrated behavior of the entire plasma is evaluated for comparison to the resolved data. Figure 4-4 shows an obvious relation between the thermal emission and fluorescence intensity. At very early delays, $< 1 \mu\text{s}$, the transition seems to be already saturated. Very little fluorescence is observable at those early delays. However, the fluorescence sharply rises as the excited states begin to depopulate from their thermal levels. The fluorescence peaks at 7 μs and decays slowly, exhibiting measureable intensity past 50 μs while the thermal emission has decayed to background levels near 25 μs .

When parsing the emission data, the time-of-flight is apparent at heights just over 1.5 mm. The first temporal point, 500 ns, is too late within the plume expansion to be

more spatially selective for this observation. In Figures 4-5A and B, the emissive plume clearly expands over 1 mm within those first hundreds of nanoseconds. As the observation region reaches 3 mm in Figure 4-5C, the delay in the emission peak to 3 μ s is apparent. Emission behavior at late delays within the plasma are summarized in Figure 4-6. The intensity scale is reduced in Figure 4-6B to show the long lived emission around 1 mm. The fluorescence traces in Figure 4-7 experience the opposite trend. The fluorescence at 3 mm above the surface peaks with the emission and quickly falls by 10 μ s. As the observation region is moved down, towards the sample surface, the fluorescence peak moves to later delays. At the limit when it reaches the sample surface, the peak fluorescence seems to be nonexistent. The peak fluorescence is quickly reached and maintained until very late delays.

At these delays after the plasma has formed, the plume has run its course, radiatively, but the species within it are still traveling out as a result of the explosion. Therefore, the loss of fluorescence is likely the result of the lead atoms expanding out of the observed volume. This leads to the conclusion that the analyte is more quickly expelled from the observation regions high within the plasma. Emitters within the higher volumes likely have greater kinetic energy, as they have travelled farther since the ignition of the plasma. Therefore, their velocity removes them from the probing laser more quickly than those analyte atoms at a lower elevation. These atoms have travelled a smaller distance and escape the probe laser at much later delays.

Ionic Fluorescence

Vertically resolved

On the whole, Figure 4-8 shows the barium ionic emission and fluorescence behave very similar to the lead atomic with some small differences. Figure 4-9 shows

three characteristic curves from the parsed data. Similar to the atomic data, the emission curves higher in the plume have their emission peak delayed to 1 μs . However, unlike the atomic data, emission does not seem to depend on the vertical location within the plasma. All points within the height of the plume seem to change at the same rate in Figure 4-10. While their relative intensities may be different, they share the same behavior in time.

Figures 4-9 and 4-11B show the fluorescence peaking much sooner, 3 μs , and sustaining that intensity past 10 μs . Additionally, the peak fluorescence for the ionic species is only 40% of the emission peak intensity. For the atomic transition, the peak fluorescence achieved 90% of the emission peak intensity. The thermal emission has reduced to background levels before 20 μs and the fluorescence is gone before 30 μs . These shorter lived trends make sense as the ionic species are expected to disappear sooner from recombination within the plasma [121]. Reflecting the trend seen in the emission data, vertically resolved fluorescence within the ionic population of barium is much less dynamic than its atomic counterpart. While there is an obvious vertical distribution difference as evidenced by the intensity change, each region seems to change in the same way with respect to time.

Horizontally resolved

The ionic barium fluorescence within the horizontal slice has a very interesting temporal distribution shown in Figure 4-12. At first glance, the fluorescence seems to be suffering from some post-filtering from the surrounding barium ions. This concern is quickly checked by the collection of another curve with a much lower concentration of barium, 0.5% by mass. The temporal distribution in Figure 4-13 corresponds to this concentration. The same structure of fluorescence depression around 5 μs is observed

even at the much lower concentration. It is believed that this feature is real.

Additionally, Figure 4-8 shows that it is shared by the vertically resolved fluorescence.

If the depression does not result from a reduction of the fluorescence at that time, then it is reasonable to account for the intensity rise with a rise in local temperature which ionizes barium to this state. This hypothesis is unlikely as the temperatures at these delays are well below the 5.2 eV required to ionize atomic barium. Much higher temperatures are possible from the effects of an internal shockwave; however, Wen predicts that the internal shockwaves have expired by this delay [109]. Another possible explanation for the depression is fluorescence quenching. It is possible that collisions within the plasma are contributing to a significant amount of quenching at these delays. Later delays may be free of phenomenon as the electron energy distribution shifts to lower energies and collisions become less frequent resulting from recombination with ions.

When looking at the parsed horizontal data in Figures 4-14, 4-15 and 4-16, the negative numbers indicate the displacement from the center of the plasma away from the dye laser. Positive numbers indicate moving from the plasma center towards the incoming dye laser. Emission profiles from Figure 4-15B of these two regions show that the plasma plume is asymmetric. There is a steeper intensity gradient towards the incoming dye laser. This reflects the trend seen in the spatially resolved emission from Chapter 2. However, in that context, the perspective is not the same, merely the trend for an asymmetric plasma holds.

The elevation observed for this data is as near the center of the plasma at 1 μ s as possible. Emission intensities are monitored until they fell to several percent of their

peak values to determine the top and bottom of the emissive plasma. The midpoint between these two minima is taken as the center of the plasma. Again, Figure 4-15A shows a time-of-flight trend as the emission peaks move to delays past 1 μs for the spatial points ± 1.38 mm. Like the vertically resolved data, there does not seem to be a strong spatial dependence for the time evolution of emission intensities.

The fluorescence curves are summarized in Figure 4-16A. The strong depression of fluorescence around 5 μs is shared by all points along the horizontal axis investigated here. Like the emission curves, the fluorescence has a much steeper rise on the side near the incoming dye laser. Figure 4-16B shows this very well. Unfortunately, Figure 4-16B also shows a nearly linear decrease in fluorescence intensity for the 5 μs dip observed in the individual plots. This could indicate that the laser is not saturating and the intensity is being absorbed. However, the fluorescence intensity is being reduced linearly as is highlighted by the red circle in Figure 4-16B. If the laser intensity is being absorbed, it must decay exponentially according to Beer's Law. If the laser is not saturating and the intensity is decaying according to this relation, then the fluorescence should respond linearly and decay exponentially as well. A possible explanation for this linear decrease in fluorescence intensity has been proposed by Vidal [122]. Here, fluorescence behavior is modeled under conditions of arbitrary optical depth. When the excitation transition is assumed to not be optically thin and the incident irradiance is large, a deviation from the Beer-Lambert Law is predicted. In their model, the incident irradiance is reduced linearly with x rather than the exponential decay of a low incidence irradiance.

The trend for the fluorescence to increase at even later delays is likely to be due to the decrease in excited state barium as is evident from the emission. This behavior is investigated for the entire plasma and is observed to decay to 0 by 50 μ s. Barium's lower ionization energy requires that a very low energy electron recombine with the ions. Because of this, the ions persist for tens of microseconds. This observation may raise some concern when comparing with the atomic lead data above. It must be remembered that this behavior is observed within a horizontal slice of the plasma while the plots above show the vertical distribution of lead. For a proper check of this behavior, the horizontally resolved experiment should be reproduced with the lead sample. It can be inferred that such an experiment would see atomic fluorescence persist much past the ionic fluorescence of barium.

Conclusions

These experiments give insight into the distribution of atoms and ions within the plasmas at much longer delays and larger spatial regions than emission. The atomic population tends to shift to lower elevations as time progresses while the ionic fluorescence maintains the same relative distribution of density. In both cases, the fluorescence intensity decays in the tens of microseconds. The ionic fluorescence shows an intensity dip near 5 μ s that is mirrored in the horizontally resolved fluorescence. This depression is less substantial at the periphery of the plasma. There is some disagreement between the horizontally resolved and vertically resolved curves. At the center of each, they should agree with respect to time as they are, theoretically, probing the same volume. Therefore, the discrepancy between the two, the lasting ionic fluorescence present in the horizontal data, must result from a different plasma structure. The most significant difference between the two data sets is the servicing of

the ablation laser between their collection. When the laser is serviced for a new flashlamp, the cleaning of the optics required a realignment of the cavity. Such an optical change can change the beam profile.

Future work includes the need to directly compare horizontally resolved atomic data to the ionic data presented above. While the data above is believed to be real and free from any artifacts, the long lived ionic fluorescence could be confirmed by longer lived atomic fluorescence.

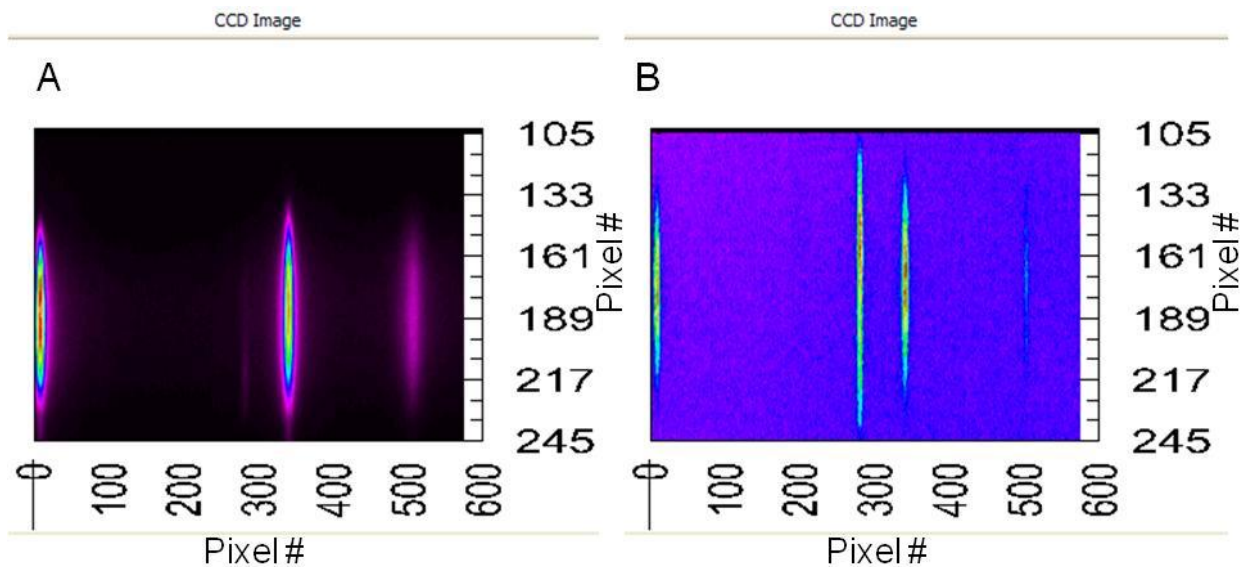


Figure 4-1. Examples of the vertical extent of the plasma at two delays. The scales at the sides indicate the pixel number of the camera. The strong emission in A is Sr II. A) Emission at 0.5 μ s. B) LIF at 7 μ s.

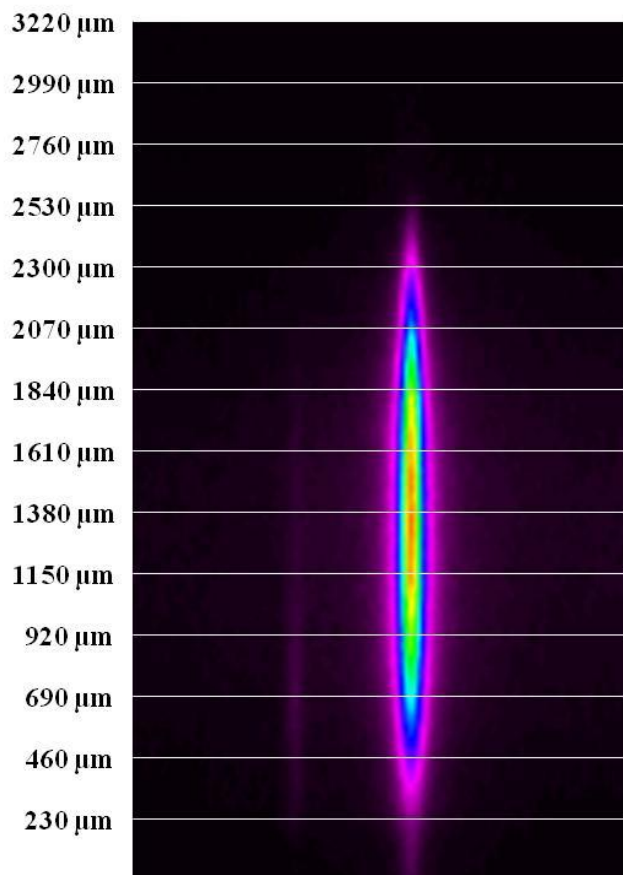


Figure 4-2. Diagram of the vertical separation of data within the CCD image at 0.5 μ s.

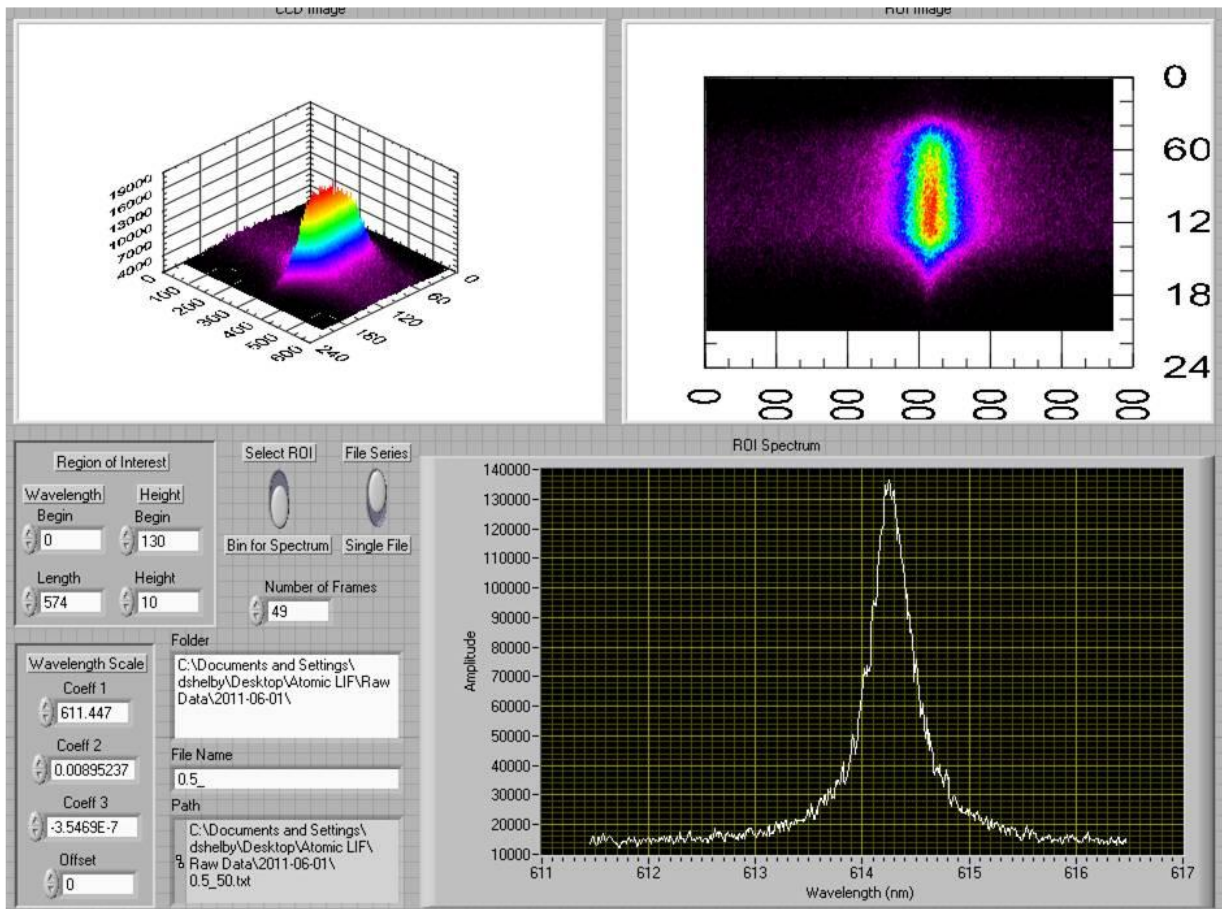


Figure 4-3. LabVIEW VI used to select ROI's and parse data within for spatial resolution.

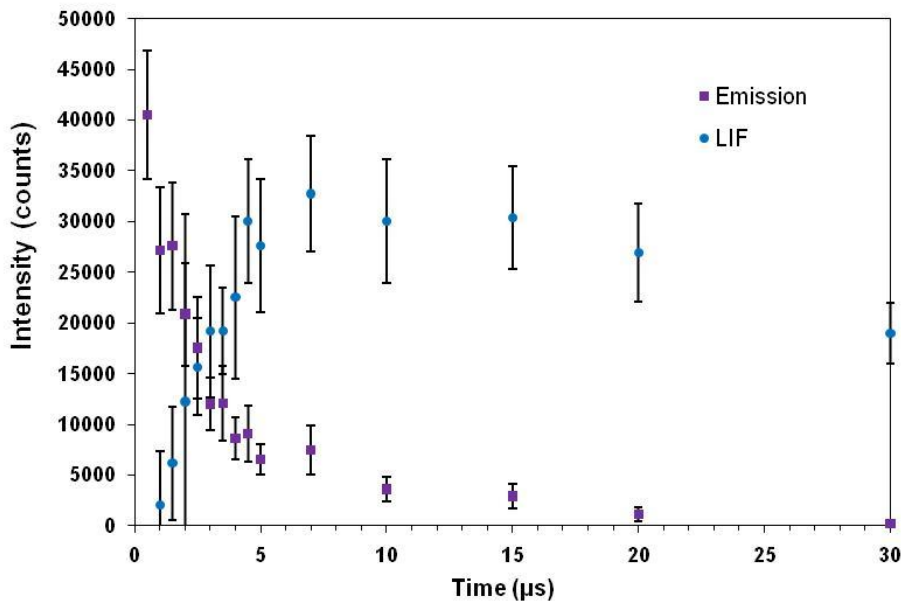


Figure 4-4. Spatially integrated Pb I emission and fluorescence signals at delays.

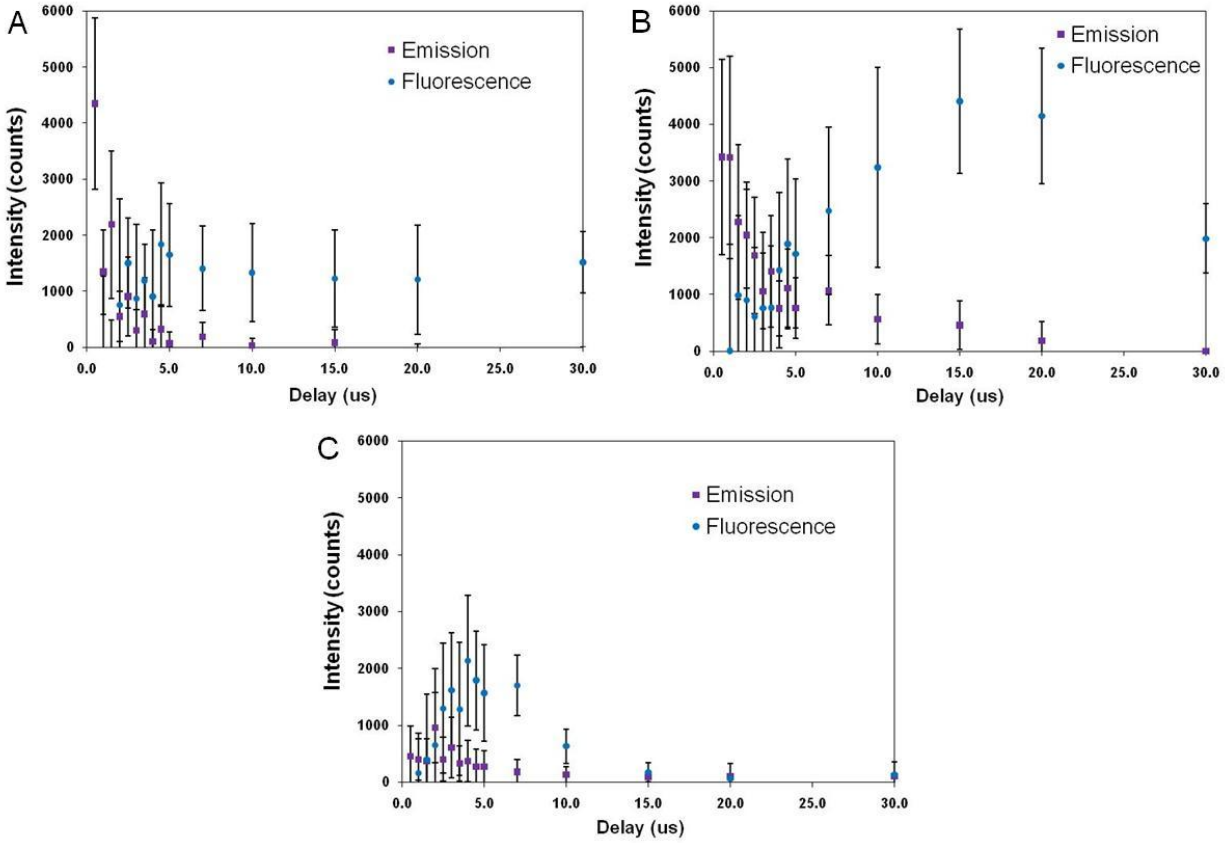


Figure 4-5. Examples of the Pb I parsed emission and fluorescence curves obtained at three heights within the plasma. A) 0.46 mm. B) 1.61 mm. C) 2.99 mm.

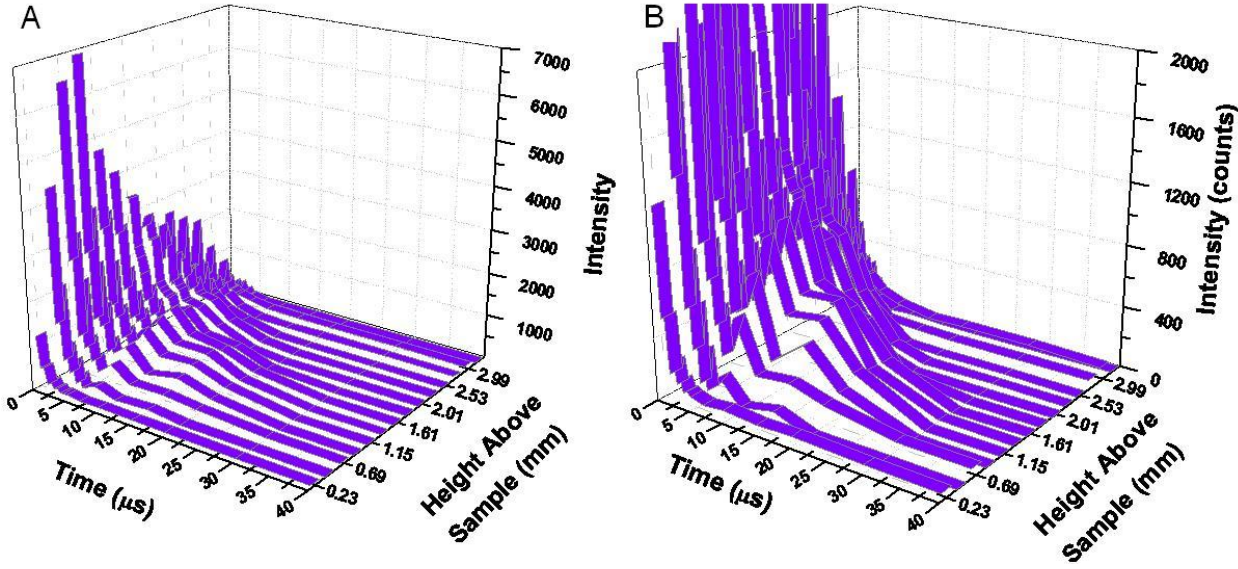


Figure 4-6. Waterfall plot of vertically parsed Pb I emission data. A) Entire intensity range. B) Intensity scale limited to 2000 counts to highlight the contour of thermal emission.

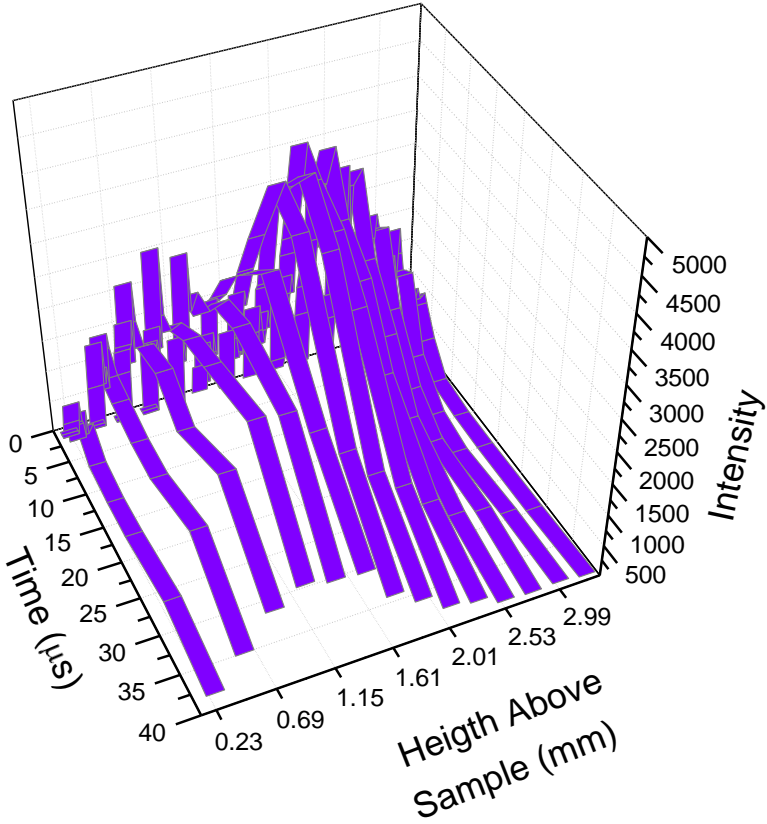


Figure 4-7. Waterfall plot of vertically parsed Pb I fluorescence data.

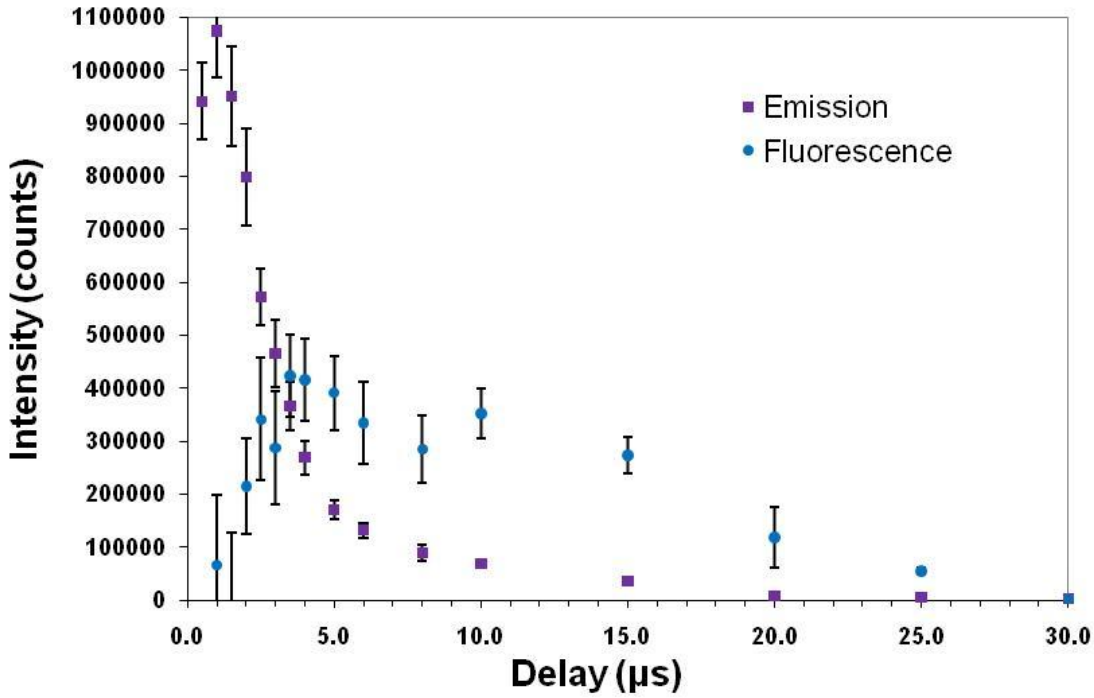


Figure 4-8. Spatially integrated Ba II emission and fluorescence signals at delays. The spatial integration is along the vertical axis within the plasma.

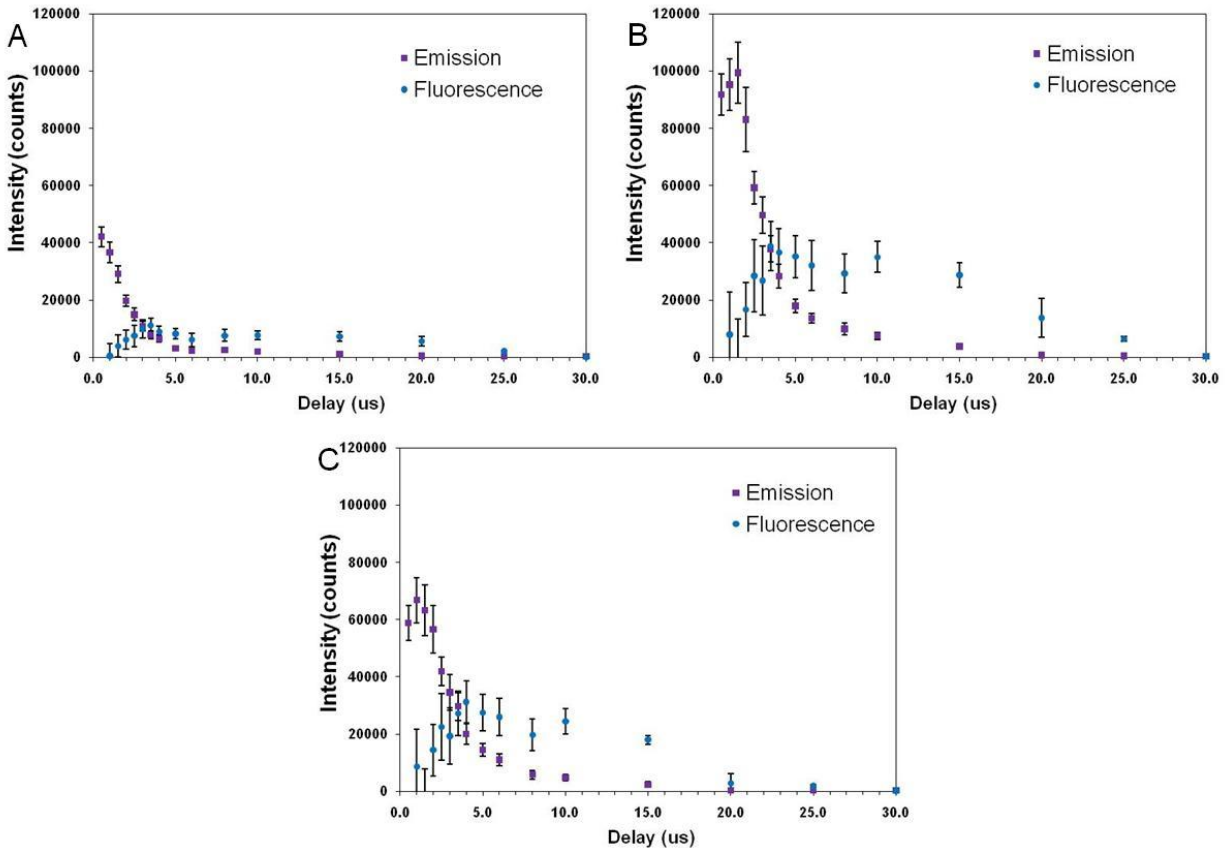


Figure 4-9. Examples of the Ba II vertically parsed emission and fluorescence curves obtained at three heights within the plasma. A) 0.46 mm. B) 1.61 mm. C) 2.99 mm.

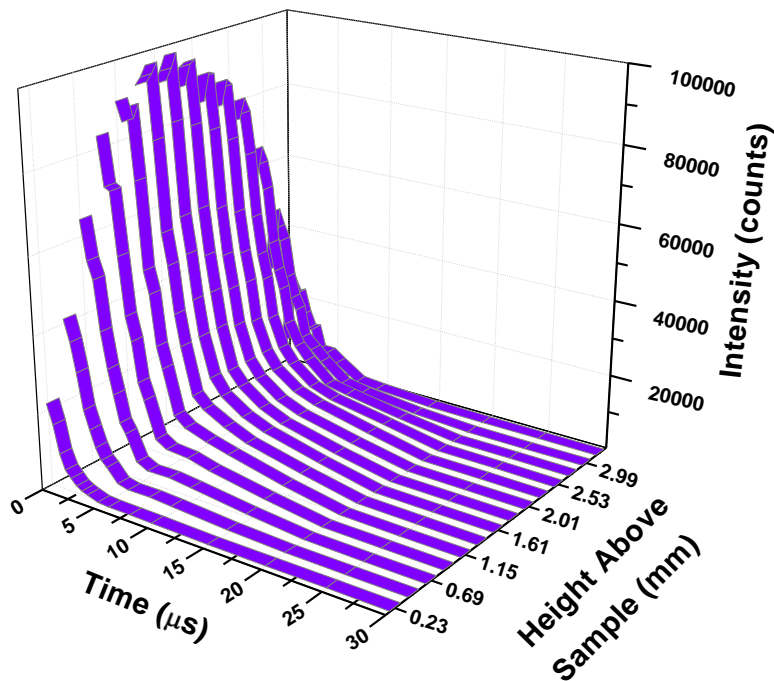


Figure 4-10. Waterfall plot of vertically parsed Ba II emission data.

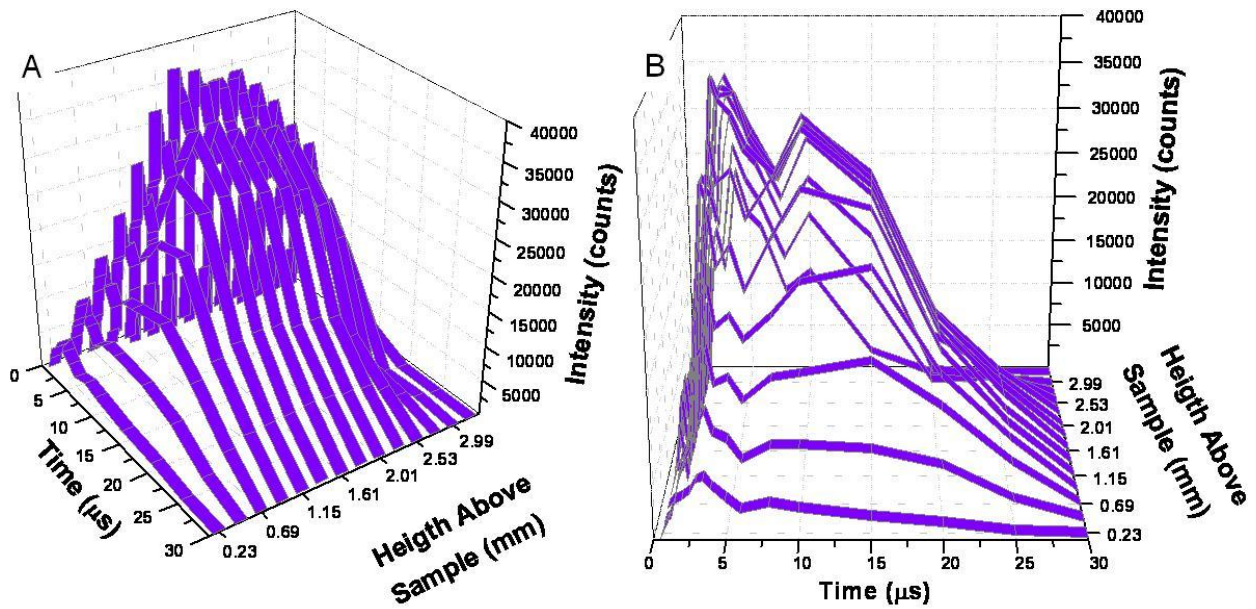


Figure 4-11. Waterfall plot of vertically parsed Ba II fluorescence data. A) Perspective on the decay of the fluorescence with height. B) Perspective on the persistent dip in fluorescence with respect to time.

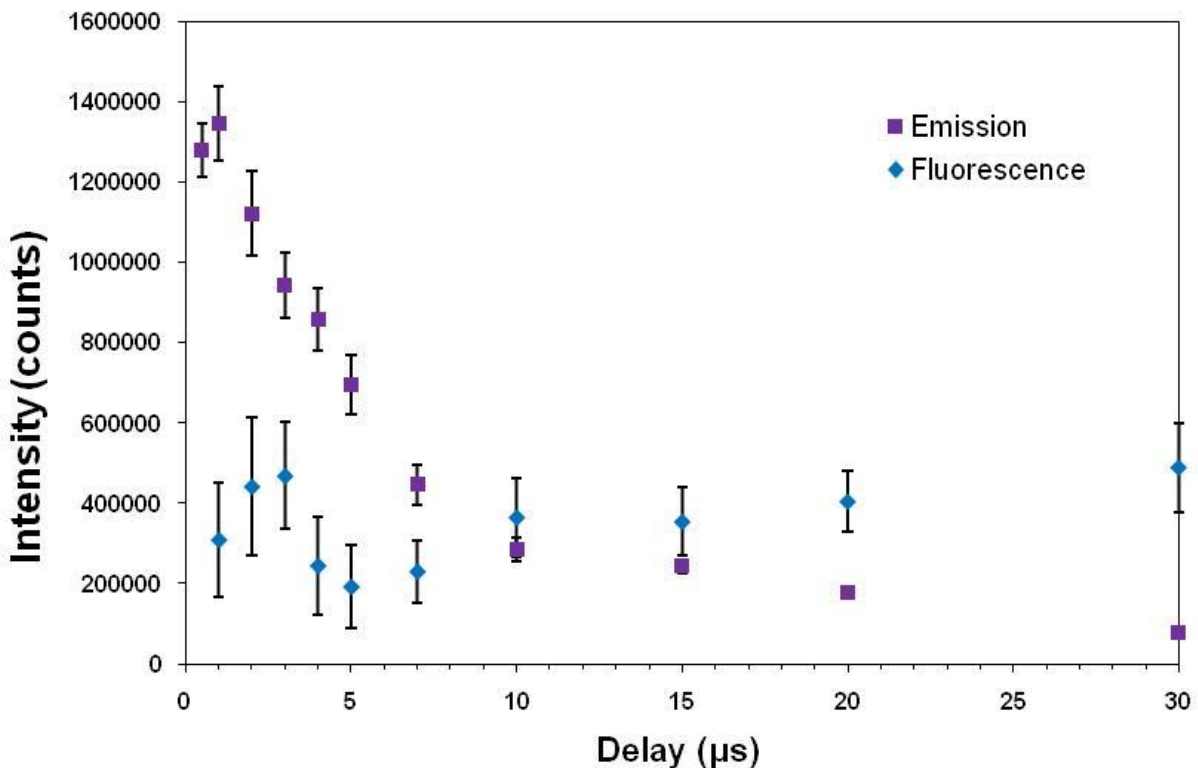


Figure 4-12. Spatially integrated Ba II emission and fluorescence signals at delays from a LIP of 11% Ba by mass. The spatial integration is along a horizontal axis within the plasma.

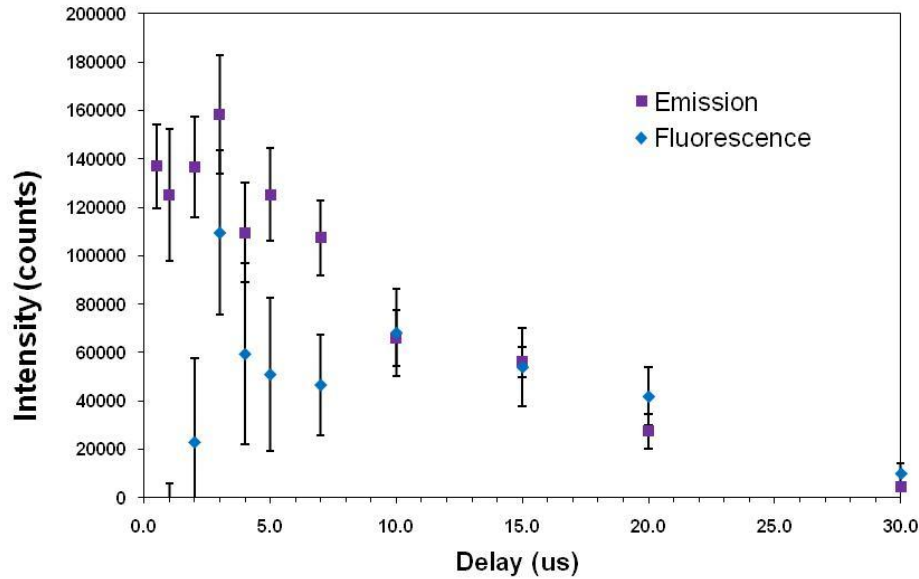


Figure 4-13. Spatially integrated Ba II emission and fluorescence signals at delays from a LIP of 0.5% Ba by mass. The spatial integration is along a horizontal axis within the plasma.

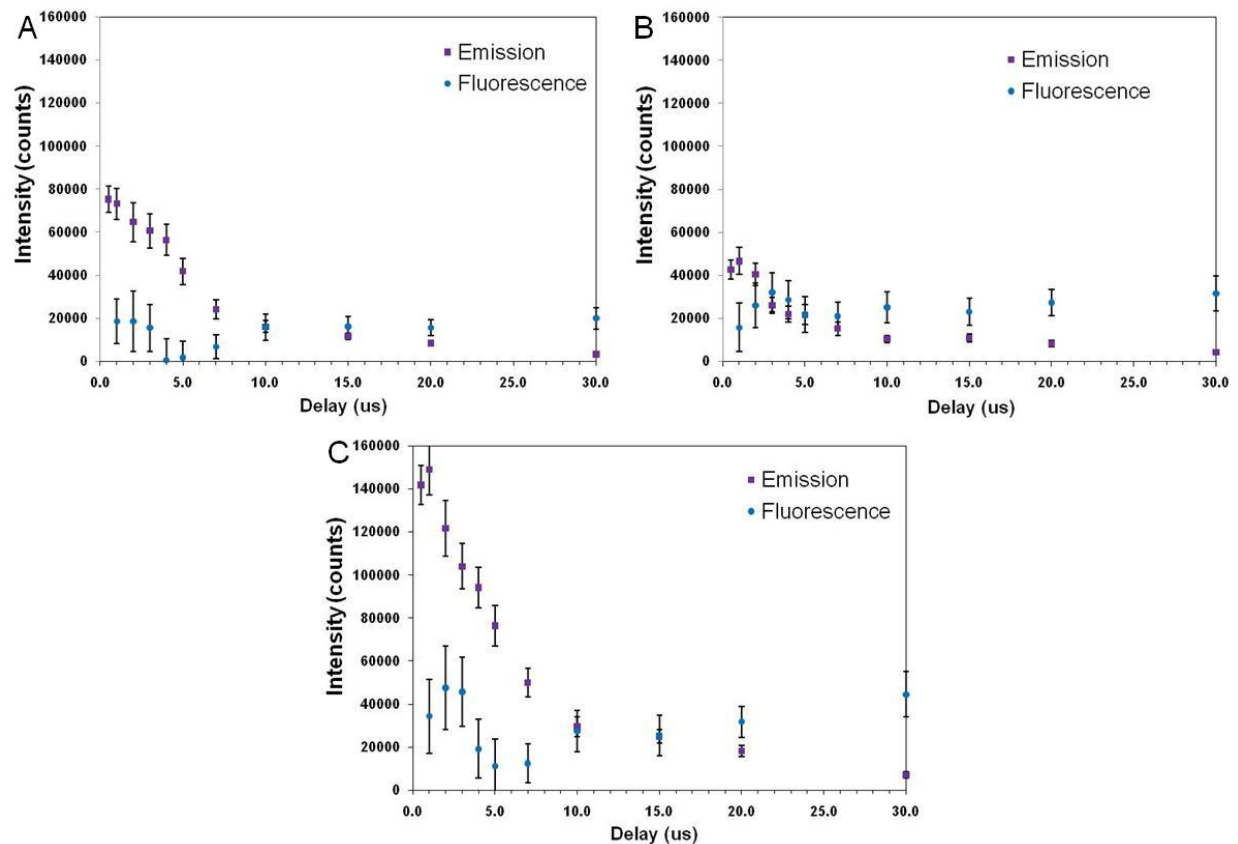


Figure 4-14. Examples of the Ba II horizontally parsed emission and fluorescence curves obtained at three positions within the plasma. A) -1.15 mm. B) 1.15 mm. C) 0 mm.

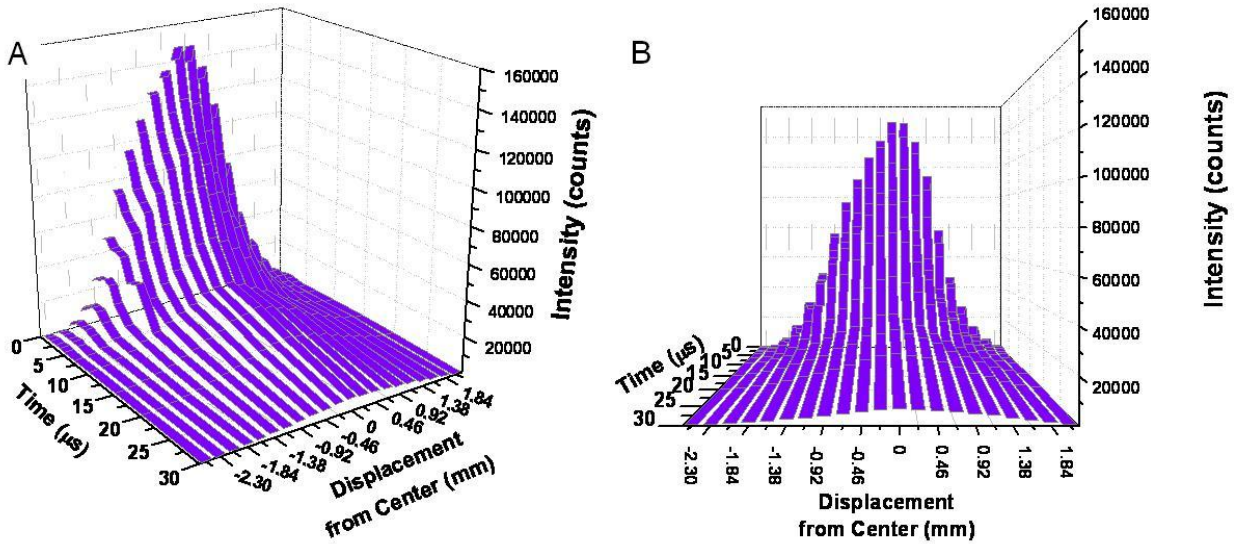


Figure 4-15. Waterfall plot of horizontally parsed Ba II emission data. A) Perspective of the decaying ionic emission. B) Perspective of plasma asymmetry.

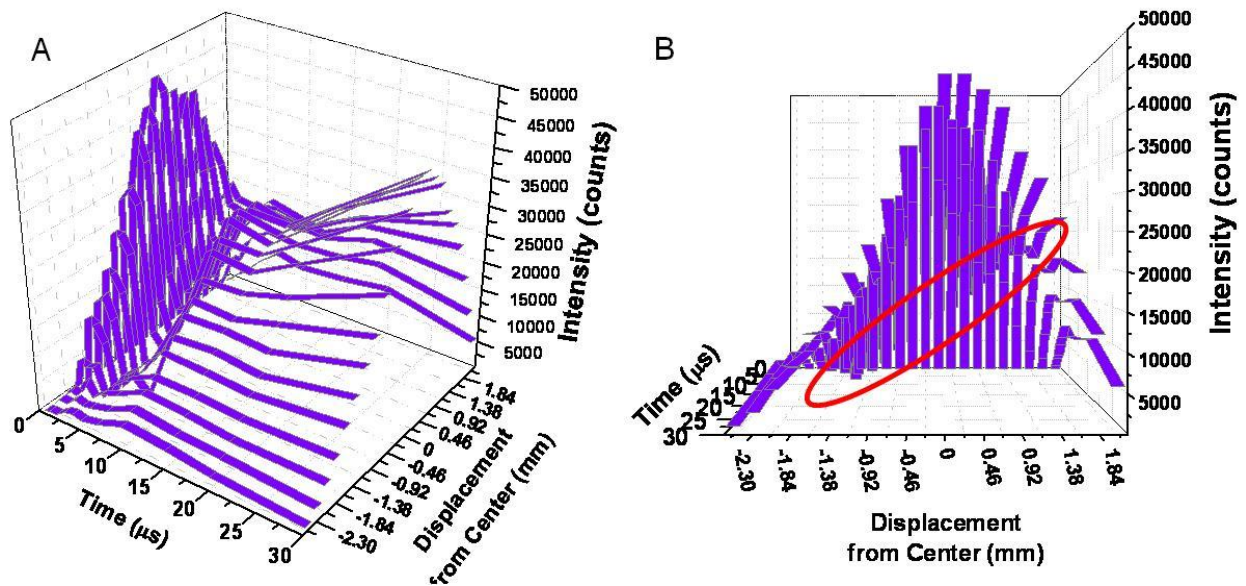


Figure 4-16. Waterfall plot of horizontally parsed Ba II fluorescence data. A) Perspective of the fluorescence with respect to time. B) Perspective of fluorescence asymmetry.

CHAPTER 5 TIME-RESOLVED LASER-INDUCED FLUORESCENCE

Motivation

Shortly after the advent of the continuously tunable dye laser, Measures proposed its use for selective excitation of atomic transitions [21]. In this paper, Measures also covers some applications for which this method may be applied. Many of the applications require time resolution on the scale of the laser pulse used to excite the atoms. During this time in the field of atomic spectroscopy, time resolution typically meant the execution of a fluorescence lifetime measurement. Accordingly, Measures' proposed methods for plasma diagnostics using LIF of atomic states required the measurement of multiple lifetime decays after the excitation pulse. Measures derived some math that could be used to evaluate local temperatures and electron number densities based on the observed fluorescence decays of multiple levels. In addition to the theoretical work, Measures and Kwong conducted some of the first practical research into time-resolved fluorescence inside a laser ablation plume [29]. They proposed a method for determining atomic lifetimes of chromium within a LIP. This use of the combined techniques for lifetime measurements has continued to today for other atoms [123] and even oxides within the plume [124].

While Measures proposed to use time-resolved LIF to evaluate temperatures and electron number densities, Burgess saw the potential to evaluate basic spectroscopic properties of atoms and ions [125]. Again, using time-resolved LIF and a consideration for population and depopulation rates within the plasma, Burgess proposed a method to measure spontaneous emission coefficients within a plasma source. For this work, long pulse lengths approached steady-state values after an initial saturation of levels. How

the system responded after the initial population equilibrium gave insight into the energy level environment around the two levels of the transition. A measure of these decay rates allowed for an evaluation of the Einstein coefficient, A . Additionally, this work in plasma LIF accounts for significant collisional coupling between neighboring states within an atoms electronic structure.

Since these early considerations of LIF, the technique has been used with success in other atom sources such as flames and ICP [126]. From this continued work, it has become evident that time resolution within the pulse length of the probe laser is important [127]. With this powerful tool, investigations have been made into the use of LIF for temperature measurements that build upon the proposal of Measures [30]. Zizak's summary shows that most methods require two probing steps. Additionally, for some applications, these two excitation steps need have to a well controlled delay. Keeping the same experimental conditions but changing the goal, two step excitation work was also done in ionization spectroscopy [32]. While complicating the experimental setup, it is clear that time resolution on the order of the pulse length for the probing laser allows for some powerful techniques. Looking at the techniques listed by Zizak, such an experimental setup also allows for the investigation of so called 'thermally assisted fluorescence'. These are levels also observed by Burgess that have a population spike from collisions with the probed transition.

Those considerations are also important for this work. Collisional phenomena like this have been studied before in a LIBS plasma [128], but Okano's investigation stopped at integrated fluorescence intensities. It seems that no research has been done to determine the delays between these fluorescence traces, rather just their

relative intensities. When comparing the volume of work done with LIBS-LIF, it is clear that time-resolved studies lack in coverage behind spatial and sensitivity investigations. Here, it is proposed to investigate more phenomena like that seen in Okano's paper [128]. Time-resolved atomic fluorescence within the plasma plume will be used to determine temperatures and collisional coupling within the plume.

Temperature Measurements

The method proposed for the evaluation of temperature was first introduced by Kunze in 1986 [129]. Like many other methods for temperature calculation, this math depends on the Boltzmann distribution of atoms or ions in their excited states from Equation 2-1. Additionally, the saturation of an optical transition is essential to the calculation. In the most simple terms, the saturation of a generic transition occurs when the population of the lower state is equal to the upper state. Reality is rarely so simple, and saturation in practical terms must account for the degeneracy of states. So, for an optical transition with the degeneracies known for the lower and upper states, saturation is defined by the condition:

$$\frac{n_2}{n_1} = \frac{g_2}{g_1} \quad (5-1)$$

Here, n_2 is the population of the upper level and n_1 is the population of the lower level, and g_1 and g_2 are the degeneracies of the lower and upper levels, respectively. The populations of the two levels at saturation can also be interpreted from the initial, thermal, populations, $n_{1,Th}$ and $n_{2,Th}$ for the lower and upper states, respectively.

$$\frac{n_2}{n_1} = \frac{n_{2,Th} + \Delta n_2}{n_{1,Th} + \Delta n_1} \quad (5-2)$$

With some rearranging, these two equations can be combined in a way that relates the initial upper level population to the increase in population. These two values are selected as they can be readily measured through thermal emission from the upper level and direct line fluorescence.

$$\frac{\Delta n_2}{n_{2,Th}} = \frac{g_2}{g_1 + g_2} \frac{n_{1,Th}}{n_{2,Th}} - \frac{g_1}{g_1 + g_2} \quad (5-3)$$

By including the relation between the lower and upper states from the Boltzmann distribution from Equation 2-1, a final relation between the fluorescence and temperature is realized. Here, the intensities are directly substituted for number densities, according to Equation 2-2, as this is a ratio between the emission and fluorescence from the same transition. Typically, the fluorescence intensity would be dependent on the number density of the lower level from which it is excited; however, in this derivation, saturation of that transition is assumed and the fluorescence comes only from the maximum allowed change in the upper state according to Equation 5-3. The spectroscopic properties of the transition are the same for both quantities and the volume observed for each has been controlled. So, ΔI_2 is the increase in the upper level population and I_2 is the intensity of the thermal emission.

$$\frac{\Delta I_2}{I_2} = \frac{g_1}{g_1 + g_2} \frac{V_{Fl}}{V_{Em}} \left(e^{\frac{E_{21}}{kT}} - 1 \right) \quad (5-4)$$

Recall that E_{21} is the energy difference between the levels involved in the saturation, k is the Boltzmann constant and T is the excitation temperature. In the conversion between number densities and intensity, I_2 and ΔI_2 , most constants cancel. However, while the two quantities share the same constant for spontaneous emission and wavelength, they differ in their observed volumes for emission and fluorescence,

V_{Em} and V_{Fl} , respectively. This consideration has been apparently neglected Kunze in his treatment of mathematics [129]. It has been included here as these two volumes will differ if the entire plasma is not saturated with fluorescence. Ultimately, an expression for the evaluation of temperature is desired. So, some rearrangements of Equation 5-4 can easily be done to generate such an expression for temperature.

$$T = \frac{E_{21}}{k \times \ln \left(\frac{\Delta I_2}{I_2} \frac{g_1 + g_2}{g_1} \frac{V_{Em}}{V_{Fl}} - 1 \right)} \quad (5-5)$$

From this point, the ratio between the fluorescence increase and thermal emission will be called R. If the natural log is taken of each side of Equation 5-4 followed by a derivative, an expression for the relative error of the ratio results.

$$\frac{dR}{R} = \frac{d \left(e^{\frac{E_{21}}{kT}} - 1 \right)}{e^{\frac{E_{21}}{kT}} - 1} \quad (5-6)$$

Applying the chain rule with some rearrangements generates an equation that evaluates the relative error of the temperature calculation based on the relative error within the measured ratio.

$$\frac{dT}{T} = \frac{dR}{R} \left(\frac{kT}{\Delta E} \right) \left(\frac{1 - e^{\frac{E_{21}}{kT}}}{e^{\frac{E_{21}}{kT}}} \right) \quad (5-7)$$

This final expression is the one used to calculate the propagated error from the ratio measurement to the final temperature. Besides the obvious dependence on the measured error, there are two clear dependencies for the temperature error. For the following discussion, the measured error is set at an arbitrary 10%.

Figure 5-1 shows that the calculated error increases with the calculated temperature. From the equation, it is clear that the dependence begins linearly as the ratio of exponentials is insignificant. The range of this linear dependence increases with the energy difference between the levels. At these higher energies, the roll off occurs later as the temperature takes longer to overcome the large energy difference. Eventually, the increase in error ceases to be dependent on the temperature. For the levels used in this study, that maximum error is roughly 9%, but does not occur until unreasonably large temperatures.

The second dependence arises from the energy difference between the two levels involved in the saturation and is plotted in Figure 5-2. Similar logic applies to this relation as in the previous discussion. Initially, the two quantities are inversely proportional. This indirect proportionality rolls off to a minimum value at high energy differences. The rate of this decline to the minimum depends loosely on the temperature as it sets the magnitude of the exponential. By 10 eV, most reasonable temperatures have approached their asymptote between 0.5 and 1.0%. For the energy levels used in this study, that corresponds to a threefold reduction in the relative standard deviation. However, such energies also surpass the ionization potential of barium.

Experimental

The instrumentation and orientation for this work shares heavily with the previous chapter. Accordingly, only the differences will be explained here. The plasma formation and probing are the same. As with the previous work, the probe beam is focused into a plane of excitation. Temperatures are investigated at two heights, and the experiments need to be free from any possible systematic error from spatial effects. A smaller region

of the plasma is collected for this investigation and a point focus would require that the observation volume overlap exactly with the probed volume. These two regions would also have to be moved in unison.

Detection of the LIF signal is accomplished through a 0.3 m monochromator equipped with a 1200 grooves/mm grating and MCP-PMT. Time resolution within the probe pulse is desired which requires this fast detector. In conjunction with the fast response time of the detector, the scope used is a 6 GHz digital oscilloscope. Typically, 500 LIF traces are averaged on the scope and saved to the internal hard drive. To generate an uncertainty for the thermal emission and fluorescence, pixels are averaged within the same trace for the two values. Their standard deviations are taken to represent the noise within the two signals. The scope is equipped with a GPIB (General Purpose Interface Bus, IEEE 488) connection. Through this connection, individual scope traces are collected by the computer for the purpose of analyzing the statistics between plasmas.

The volume of the plasma observed in this setup needs to be restricted as much as is possible. The reasoning for this requirement lies in the proposed temperature calculation. Since the equation depends on the ratio between the thermal emission and fluorescence intensities, the observed volume of both should be equal. Were they not, the ratio of intensities would vary, not because of the induced fluorescence, but as a result of the differing observation volumes. In an attempt to control this limitation, a trick has been introduced into the collection optics shown in Figure 5-3. First, an image of the plasma is formed by a single biconvex lens. The plasma and image are both 2 focal distances away from the lens. An image is formed on an iris which is restricted down to

a diameter of 0.5 mm. A second biconvex lens is used to form an image of the light passing through the iris. This is the image that hits the slit of the monochromator and is used in the time-resolved fluorescence studies.

Temperatures are calculated using fluorescence waveforms from Ba^+ . The same excitation scheme used in the spatially resolved work is used here. The ion is excited at 455.403 nm while emission and fluorescence intensities are monitored at 614.171 nm. It is important that the observed fluorescence is a strong line while not being self-absorbed. A strong emission is required for an adequate evaluation of the thermal population of levels, but a very strong line can sometimes be self-absorbed at higher concentrations. The emission line used here is relatively weak. With an Einstein coefficient for spontaneous emission of 4.12×10^7 Hz, the barium ion line falls within this region.

In addition to temperature calculations, the time-resolved fluorescence measurements lends itself to analyzing the collisional coupling within the plasma. To investigate these properties two excitation and observation schemes are used. The energy levels and transitions involved are plotted in Figure 5-4. Two excitation wavelengths are used as they are easily tunable and correspond to strong transitions. Both probes populate levels with strong direct line fluorescence, and both schemes allow for the collisional population of an excited state at 54949 cm^{-1} . Specifically, the first excitation used is that of the previous chapter at 455.403 nm with fluorescence at 614.171 nm. The second scheme excites at 452.493 nm with the fluorescence 489.997 nm. The collisionally coupled state emits at 389.178 nm. For this part of the study, 500 fluorescence traces are averaged to generate each waveform.

Results

Temperatures

Time-resolved fluorescence waveforms are the work horse for this section. These waveforms are induced by the dye laser output tuned to a transition of the analyte, barium, in this work. The specific output of the dye laser at 455.403 nm with respect to time has no clean distribution as shown in Figure 5-5. Rather, it reflects the temporal shape of the excimer laser pumping it. Temperatures calculated with these LIF traces take their fluorescence increase from the fluorescence induced by the initial peak of the dye laser and their thermal emission as the signal present just before the fluorescence peak.

There is some concern that the erratic power output of the excimer laser could introduce some drift in the dye laser power. If great enough, this drift could alter the shape of the fluorescence waveforms. While unlikely, as 500 laser shots are averaged, the reproducibility of the method is checked by four repetitions of the experiment with 500 averages of 614.171 nm fluorescence on four different sample locations. Figure 5-6 shows the overlay between these four trials. Clearly, any drift present in the excimer laser power does not affect the results generated by this experiment.

From fluorescence waveforms similar to those plotted in Figure 5-6, temperatures are calculated at several delays within the plasma and plotted in Figure 5-7. This particular set of data is collected with the iris selecting a region about 1 mm off of the sample surface. Accordingly, the temperature at the earliest delay time, 1 μ s, is both uncertain and low. This indicates that this spatial region lies at the edge of the emissive plume at that delay. Any measurement taken on the steep gradient of a dynamic system is expected to exhibit this precision decrease. By 2 μ s, the plume has expanded

to encompass that entire region, giving a more reliable temperature measurement. The temperature levels out around 7000 K and maintains that value through the delay of 10 μs .

Next, the iris is moved to image the region of the plasma just grazing the sample surface. Emission intensities are monitored as the iris is moved down, through the image. Temperatures calculated for this height are plotted in Figure 5-8. The volume observed at this height has the most intense emission and highest temperatures as measured by the two-aperture system. As expected, the temperatures at early delays reflect the hotter core of the plasma plume. For the higher elevation, the temperatures settle down to 7000 K by 3 μs . At the center of the plasma, the temperature takes until 8 μs to reach that level.

To verify that these temperatures make sense for this laser irradiance, a Boltzmann plot needed to be constructed based on Equation 2-4. The Boltzmann plot is taken to be the experimental check as it is the widely accepted method for temperature calculation within a plasma source [70, 75, 130]. Its construction is explained in Chapter 2 for the derivation of the Saha-Boltzmann plot used in the CF-LIBS analysis. Sabsabi established the convenient use of a single spectroscopic window for the construction of Boltzmann plots [130]. Centered at 373 nm are 8 iron lines with well-known spectroscopic properties. These lines can be used without any calibration of the instrument response as they are all closely spaced and span 8,000 cm^{-1} , or 1 eV, in energy. While the above plots represent temperatures with a measure of spatial resolution, the Boltzmann plot presented in Figure 5-9 is an integration of the entire plasma. Additionally, the sample used for the fluorescence temperatures is a glass with

a very low concentration of iron. The window and procedure proposed by Sabsabi would not work as an easy check for this sample [130]. So, a different sample containing more iron is placed at the focus of the laser. The aluminum D33 alloy is used. Its composition is shown in Table 2-1. While the different physical properties of the silicon glass and aluminum alloy will cause different plasmas to form, this is simply a check that the temperatures are in the correct order of magnitude and exhibited the same trend. The same ablation laser properties and ambient conditions are used for each measurement.

Again, the temperature at 1 μs is unreliable. It is believed that these early delays may not adhere to the local thermodynamic equilibrium necessary to fulfill the requirements of a Boltzmann plot. Later delays, however, show a very similar trend to the fluorescence temperatures. A temperature of 7000 K is approached near the 7 μs delay and maintained through 10 μs . Since this is an integrated measurement, there will be some overlap between both of the spatially resolved fluorescence temperature measurements.

As was described in the experimental section, much of this work is averaged on the oscilloscope. The model of oscilloscope used in this work does not report the standard deviation of each time pixel when taking the average. As a work around, several pixels are taken in each region, emission and fluorescence, and these values are used to generate errors. Another approach for the evaluation of noise within the signal is to collect 500 individual traces and average them in a spreadsheet program outside of the oscilloscope. Then, a standard deviation between the 500 traces can be obtained for each point in time. Finally, a calculated temperature can be derived from a

single point of emission and a single point of fluorescence. The magnitude and trend of the temperatures in Figure 5-10 agree well with the work done on single traces. The error is obviously much more significant, never dropping below 45%.

However, when the same calculation is made on the similar experiment done with 452.493 nm excitation and 489.997 nm fluorescence, the error within the temperature is much less. Figure 5-11 shows the temperatures at delays for this higher energy excited state. Since these two methods should contain the same experimental error, it may hint that some problems may rest with the use of a resonant line. As will be shown in the next section, the 452.493 nm transition is very clearly saturated at all times. With the fluctuations present in the pulse-to-pulse power of the excimer laser, it is possible that some laser shots may not completely saturate the resonant transition. This could introduce significant error into the calculation when propagating error between shots.

There is a collisionally coupled state that lies $23,997 \text{ cm}^{-1}$ above the level probed by the 455.403 nm. It is a simple matter to measure the fluorescence from this level the results from the dye laser probe. Since this level is collisionally populated with respect to the probe laser, it is not expected to be a saturated transition. Accordingly, it should not fulfill the requirements of the temperature method used on the direct line fluorescence at 614.171 nm. A strong radiative transition from this level has the wavelength of 389.178 nm. By monitoring the emission and fluorescence from this level in the same way that the direct line fluorescence is measured, temperatures can be calculated for several delays. Figure 5-12 shows the temperatures calculated from this fluorescence. The temperatures calculated here are larger than those derived from the direct line fluorescence. Such a trend is expected for a transition that is not saturated.

The observed fluorescence will be interpreted as the increase in population required to equilibrate the two levels. When this value is low as a result of a linear response to excitation, the thermal emission is interpreted as being too large of a contribution. That higher weighting to the thermal emission results in a falsely high temperature.

Removing Volumes from Calculated Temperatures

While there is very good agreement between the saturated fluorescence temperatures and the Boltzmann plot method, the issue of observed volumes cannot be ignored. Equation 5-5 shows the volume dependence of the calculations. For the work above, a value of 1 is assumed. Figure 5-13 illustrates the behavior of the calculated temperature as the volume ratio is increased to a realistic value. The plasma plume can be estimated at 2 mm. This dimension depends on the delay after the plasma formation, but the diameter will be somewhere near this value for most delays considered here. The width of the excitation plane within the plume is close to 0.1 mm. Therefore, the volume corrected temperature corresponds to 5000 K at a volume ratio of 20. While the observed areas are the same, the depth observed for the emission and fluorescence are different. The optics and iris used to restrict the observed volume only works in two dimensions. The third dimension, depth, is controlled only by the volume excited by the dye laser. This issue can be easily avoided experimentally if the dye laser is expanded to induce fluorescence within the entire plasma. In this scenario, the volumes would be equal, and their ratio would reduce to 1. However, for the laser energies and power available with the current dye laser setup, the reduction of laser excitation irradiance brought about by beam expansion would not maintain saturated conditions over the entire excitation volume. The levels would no longer obtain an equal population density, and no temperature could be calculated.

The above correction factor is an estimation that depends on the delay of observation and plasma structure. A more absolute solution would be a mathematic removal of the volume ratio. An expression for temperature without the volume ratio would be possible if the volume ratio could be cancelled by executing the temperature measurement twice. A ratio of these two expressions would eliminate the volume dependence since both expressions would have the same emission and fluorescence volumes. These two measurements would have to be at different wavelengths such that a ratio between the two would not simply reduce to 1. Beginning with Equation 5-4, the ratios and the degeneracies for each ratio will be reduced to R and R' and g and g'. Therefore, a ratio of two Equations 5-4 gives,

$$\frac{R}{R'} = \frac{g}{g'} \frac{V_{Em} V_{Fl}'}{V_{Fl} V_{Em}'} \left(e^{\frac{E_{21}}{kT}} - 1 \right) \left(e^{\frac{E_{21}'}{kT'}} - 1 \right)^{-1} \quad (5-8)$$

where $V_{Em} = V_{Em}'$ and $V_{Fl} = V_{Fl}'$. This removes the volume dependence and generates Equation 5-9. The equation has been rearranged into this form to show the consequences of possible assumptions.

$$\left[Rg' - R'g \left(e^{\frac{E_{21}}{kT}} \right) \left(e^{\frac{E_{21}'}{kT'}} \right) \right] e^{\frac{E_{21}'}{kT'}} = Rg' - R'g \quad (5-9)$$

The first assumption is required to use Equation 5-9 as an evaluation for temperature, and this assumption is that the calculated temperatures, T and T', are equal.

$$\left[Rg' - R'g \left(e^{\frac{E_{21} - E_{21}'}{kT}} \right) \right] e^{\frac{E_{21}'}{kT}} = Rg' - R'g \quad (5-10)$$

From Equation 5-10 it would be possible to calculate a temperature from two measured intensity ratios. The relation is strongly dependent upon the difference between E_{21} and E_{21}' . This fact can be easily illustrated by assuming that these two energy differences are equal or very close, as in our case. If $E_{21} = E_{21}'$,

$$Rg' - R'g \left(e^{\frac{E_{21}'}{kT}} \right) = Rg' - R'g \quad (5-11a)$$

and

$$\frac{E_{21}'}{kT} = 0 \quad (5-11b)$$

This solution requires that there is no transition. Such a stipulation contradicts the measurement itself. Therefore, the two saturated transitions, E_{21} and E_{21}' , must have very different energy differences for the mathematics to hold. In the present work, the energy differences are very nearly the same, resulting in the condition of Equation 5-11b. An actual temperature can only be calculated in this manner for two saturated transitions that are significantly more different than 455.403 nm and 452.493 nm.

Response Times

Evaluating the population dynamics within a plasma which result from a probe laser can shed light on its collisional properties. Four delays are selected for this investigation into collisionally coupled fluorescence with 455.403 nm excitation, 1, 3, 5 and 10 μ s. At each delay, the direct line fluorescence at 614.171 nm is recorded along with the collisionally coupled state emitting at 389.178 nm. Some examples of the measured emission and fluorescence curves at 614.171 nm are shown in Figure 5-14. At 1 μ s the fluorescence appears to maintain for several tens of microseconds. While the emission and fluorescence traces were taken at significantly different dates, the

trend of the emission shows that over the 100 ns window, the emission is flat.

Therefore, the sustained intensity in the fluorescence curve could be a real fluorescence intensity. Such a long lifetime of fluorescence is likely due to the high electron number density at that early delay. The frequent collisions could be transferring atoms into and out of long lived states near the upper energy level of the fluorescence emission. If any of the neighboring states have unfavorable spontaneous emission coefficients, it is possible that the atoms in these levels will retain their energy long enough to repopulate the 614.171 nm upper energy level for some tens of nanoseconds. By 3 μ s in Figure 5-14B, the fluorescence intensity clearly reduces to the level of emission shortly after the probe laser ends. At this delay, there must be fewer collisions to sustain the excited state population past the life of the probe pulse. A proper investigation into the behavior of the fluorescence at each delay requires an analysis with rate equations. Such an evaluation of the data is planned, but this discussion is not included here. These considerations also hold for the collisionally coupled state emitting at 389.178 nm.

The waveforms for 389.178 nm share the same behavior at early delays. Again, the emission curves in these figures are intended to show the trend of the emission at these delays and not the absolute magnitude. Unlike the direct line fluorescence, the collisionally coupled level shows a lasting fluorescence intensity even at 3 μ s in Figure 5-15B. It can be concluded that this highly excited state neighbors more energy 'traps' than the direct line fluorescence upper energy level. Such a conclusion is supported by the increase in the density of states near the ionization potential. By 5 μ s in Figure 5-15C, the 389.178 nm fluorescence reduces to the emission level after the probe pulse

ends. The long life of the fluorescence intensity for 389.178 nm is made very clear in the normalized waveforms of Figure 5-16.

Since this section does not care for the absolute magnitudes of the fluorescence and collisionally coupled emission, the normalized curves are more useful. Figure 5-16 shows the three traces at the four delays. These traces are plotted with the 455.403 nm scatter from the probe laser to show their relative response times. The signals for each trace are normalized to their peak value to show their relative behaviors. When looking at the normalized waveforms, it is important to understand how normalization affects a saturated fluorescence signal. Taking an ideal sigmoid as the excitation step, Figure 5-17A shows how a fluorescence signal is initially linear with the excitation. As the transition nears saturation, the fluorescence rolls off to some steady value. When these two traces are normalized in Figure 5-17B, the fluorescence appears to be emitted before the excitation pulse. However, this is an artifact of the signal processing, but it is a good indicator of saturation.

It is difficult to see the decay of the fluorescence intensity to the background value of thermal emission. The ringing present is attributed to the triggering of the excimer laser used to pump the dye lasers. In theory, a simple dark subtraction could take care of this ringing, but a quick glance at the 5 and 10 μ s delay traces shows the ringing is not a stationary artifact. Accordingly, the ringing must be endured. It is most significant at the low absolute intensity of the 389.178 nm emission.

When looking at these four plots as a whole, one obvious change is the shape of the direct line fluorescence as time progresses from 1 to 10 μ s. At 10 μ s, the two peaks of fluorescence are at their closest values. This indicates that even the second pulse of

the 455.403 nm probe laser is nearing the saturation mark. Since saturation is a rate process, early delays require higher probe laser powers to overcome the depopulation from frequent collisions. As time progresses and the electrons taking part in these collisions lose energy to them, achieving saturation between two levels requires less probe laser power. If the fluorescence were linear with the excitation, the two waveforms would more closely track each other. By this logic, the 1 μ s fluorescence waveform is nearing linearity, but saturation is checked as described in the previous chapter with the 0.3 optical density filter.

The second feature that draws the eye is the response time of each trace. With increasing delay, the gap between the rise of the direct line fluorescence and the collisionally coupled state grows. The gap is measured as the time difference between the half intensity of the two pulses. Since these traces are normalized, the delay in the response time is simply the difference between each time value at 0.5 intensity. The relation is plotted in Figure 5-18. This indicates one of two phenomena. First, the energy distribution of the electrons active in the collisions is shifting to lower energies. Second, the electron number density is falling which reduces the frequency of collisions. Reality being shades of grey, it is likely a combination of these two processes which contribute to the delay in the population of the collisionally coupled state.

These same experiments and considerations are made for the 452.493 nm excitation scheme. Figure 5-19 shows the three traces at three delays, 3, 5 and 10 μ s. Again, the transition to later delays shows the trend for the direct line fluorescence to peak sooner than the probe beam. Like the 455.403 nm excitation scheme, this is taken to represent the saturation of the probed level. Additionally, at all delays shown

here, the pulse shape of the direct line fluorescence diverges greatly from the pulse shape of the probe beam. This is strong evidence for a much easier saturation of the 452.493 nm transition. As mentioned before, good agreement between the probe and fluorescence traces indicates a linear response. A poor overlap between the normalized pulse shapes indicates that the transition is saturated even by the lower power peak 20 ns after the initial pulse.

The difference in response times for this excitation is all very short. The direct line fluorescence originates from a level that is only 0.45 eV below the collisionally coupled state with emission at 389.178 nm. Such a close energy spacing allows for much lower energy free electrons to populate between the two levels. By opening up the possible successful collisions to these lower energy electrons, the difference in response times between 489.997 nm and 389.178 nm is always less than 1 ns. Even at 10 μ s when the response time lags 2.5 ns for 455.403 nm excitation, the collisionally coupled level is populated within a nanosecond when probing with 452.493 nm.

Conclusions

A single-line method for local temperature measurements is proposed. Two excitation schemes are evaluated with good agreement to a Boltzmann plot temperature, an accepted temperature calculation. The next step is to attempt the same evaluations on different analytes within different matrices at different concentrations. It is possible that major elements may not be investigated by this method as a result of pre- or post-filtering by atoms. Also, some attention needs to be paid to noise sources for this calculation as the propagated error strongly depends on the experimental conditions. Perhaps the most important consideration for this temperature calculation is the elimination of the volume dependency. As was shown in

the results, inaccuracies within the volume ratio can cause the calculated temperature to be inaccurate by a factor of 2. However, the method still has good agreement on the order of magnitude. Two resolutions exist for this problem. First, as was described in the chapter, the temperature measurement could be executed on two transitions of varying energy difference. An evaluation of this sort mathematically removes the volume elements. Another solution to this issue lies in the experimental implementation of the method. If a dye laser or OPO of adequate pulse energy could be procured, the measurement could be done with a beam expanded probe. Assuming the probe beam had sufficient energy to saturate the entire plume, the volume of emission would equal the volume of fluorescence when the entire plume is probed.

This method is also applied to the investigation of collision dynamics within the plasma with success. A clear relation is observed between the delay of response times and the energy separation of levels. The exact form of this relation cannot be define without a thorough rate equation investigation. Such an evaluation will be completed in future work. Saturation of the direct line fluorescence is confirmed by normalized waveforms of both excitation schemes.

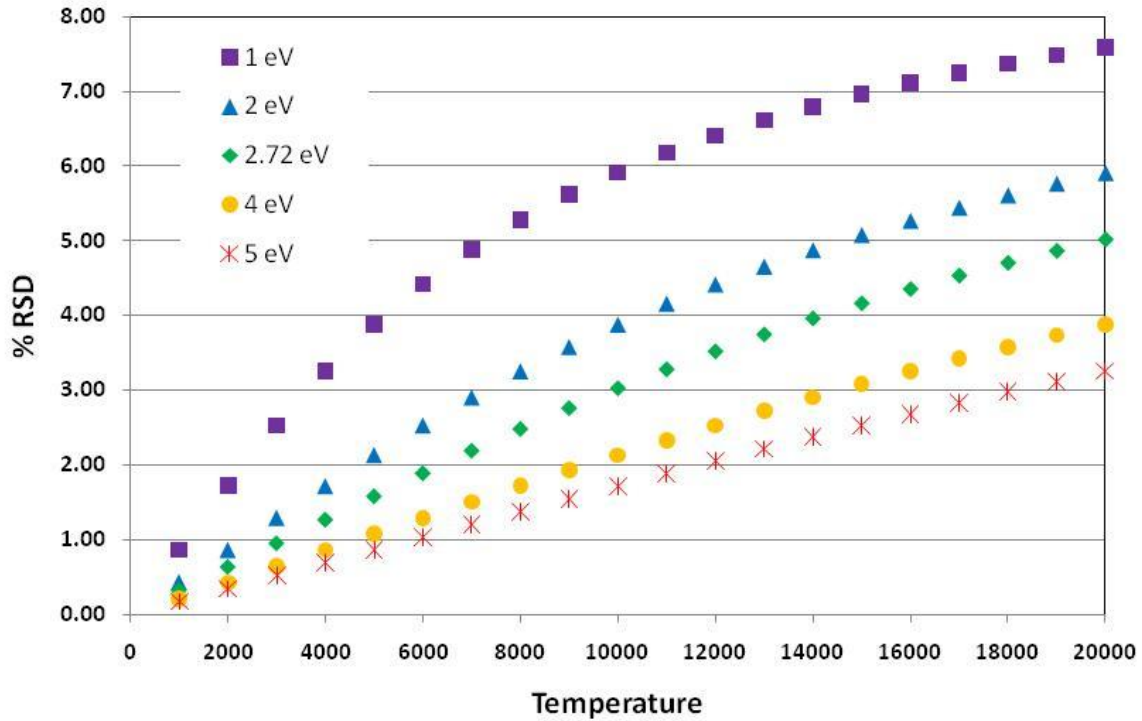


Figure 5-1. Temperature dependence of the precision of the calculated temperature from a 10% error within the observed ratio.

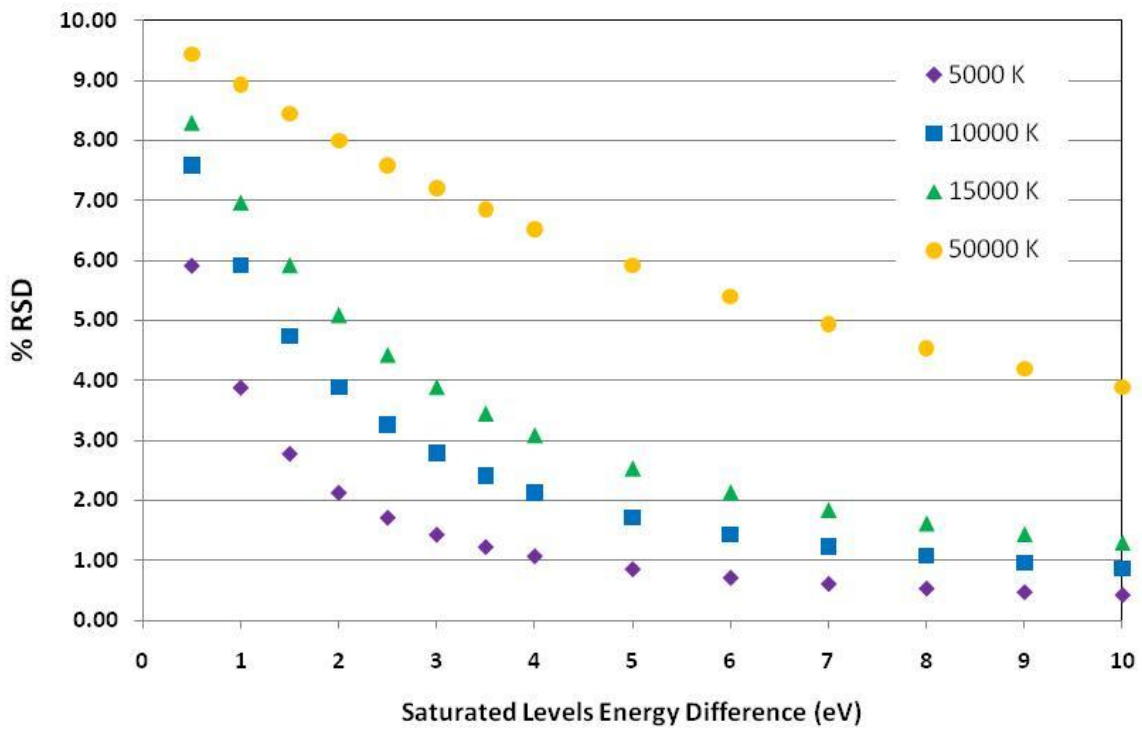


Figure 5-2. Separation of energy level dependence of the precision of the calculated temperature from a 10% error within the observed ratio.

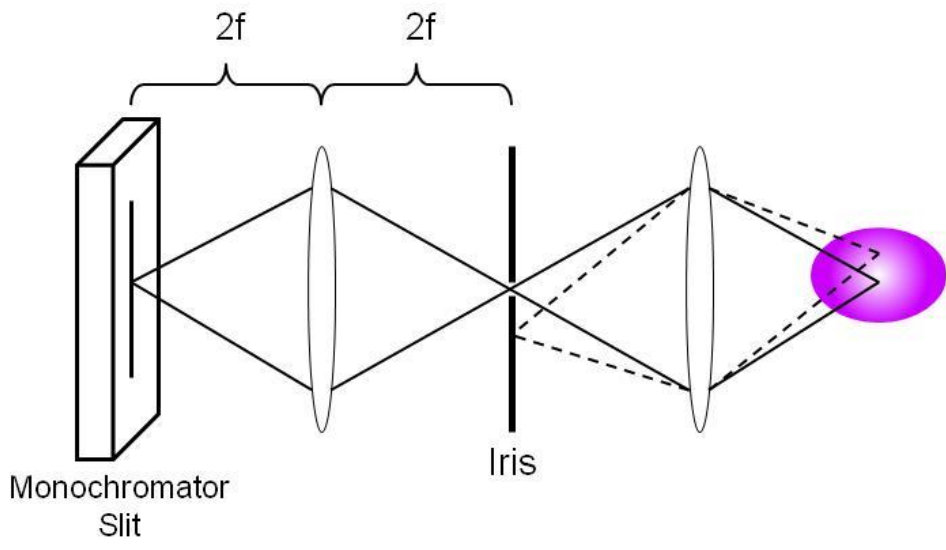


Figure 5-3. Lens geometry for spatially selecting regions of the plasma.

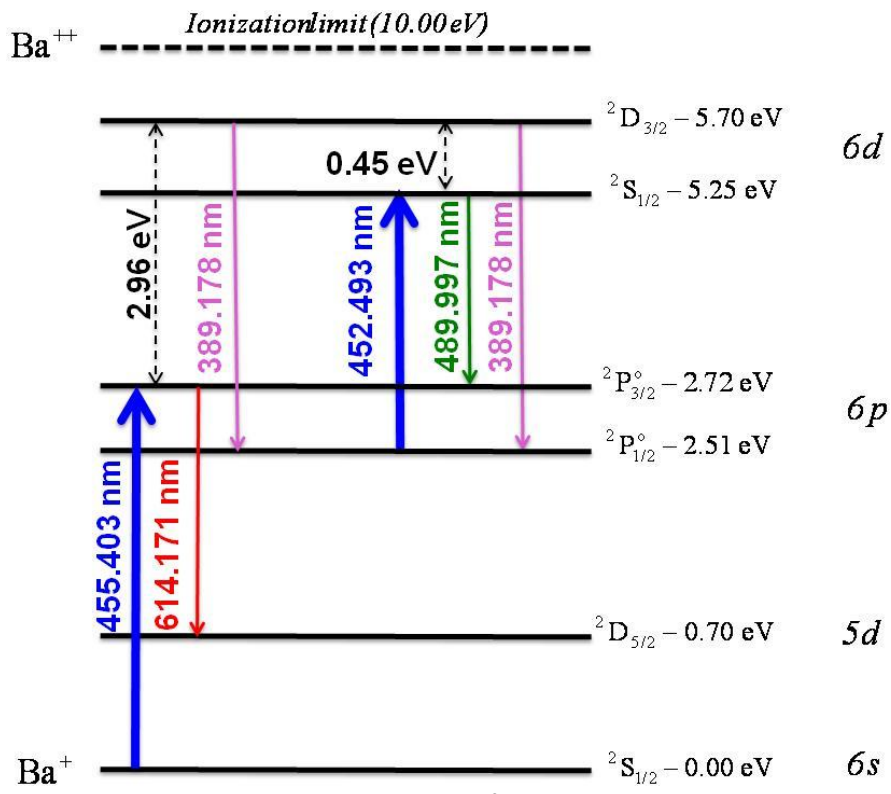


Figure 5-4. Energy level diagram for Ba II. Both excitation and direct line fluorescence transitions are shown as well as the collisionally coupled state.

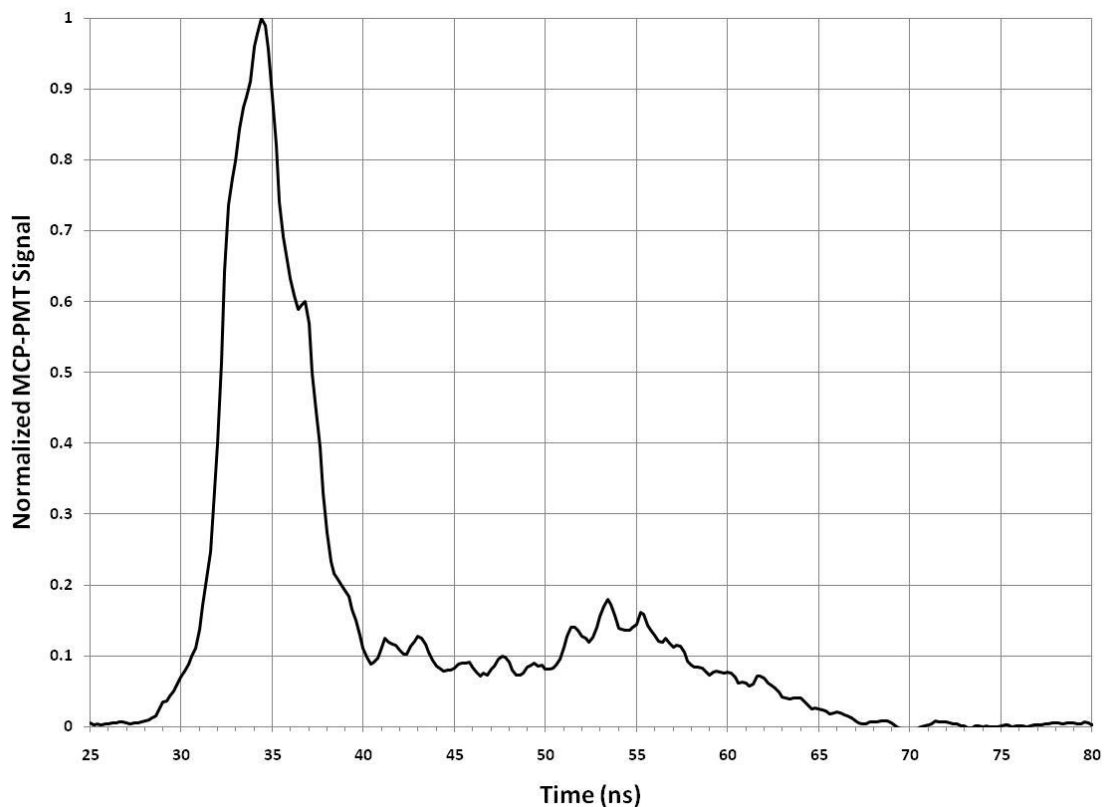


Figure 5-5. Temporal profile of the excitation pulse at 455.403 nm.

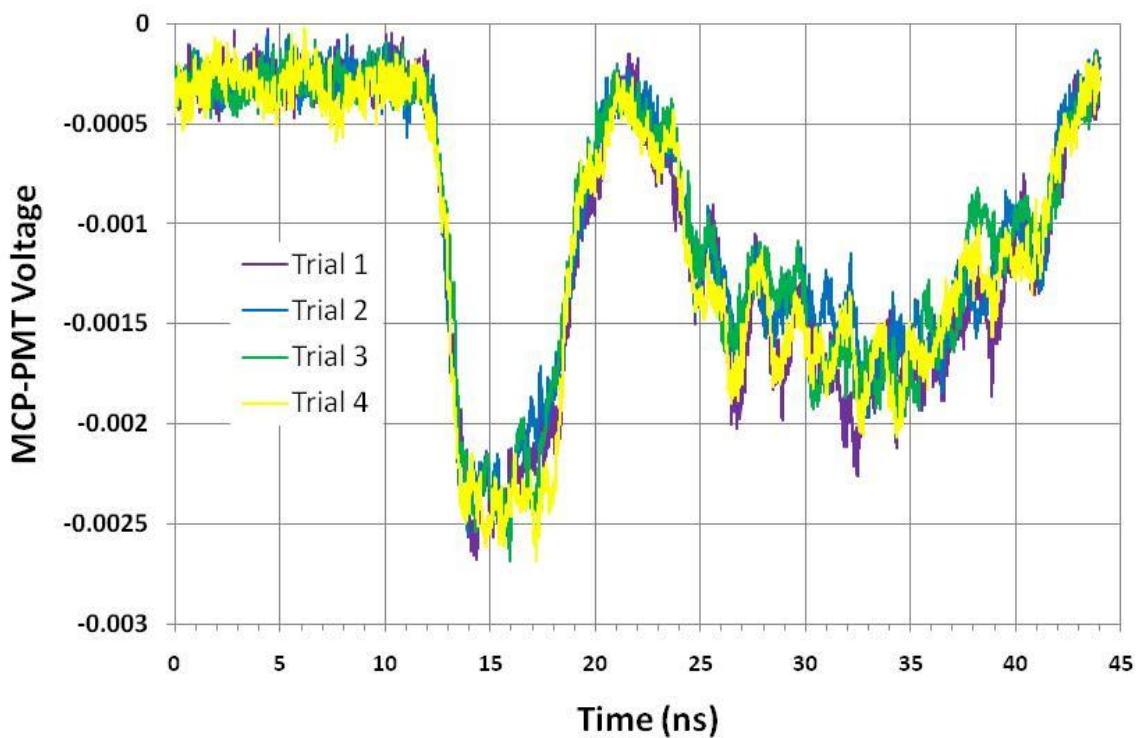


Figure 5-6. Repeatability of 4 temporal profiles of the 614.171 nm direct line fluorescence each averaged from 500 laser shots.

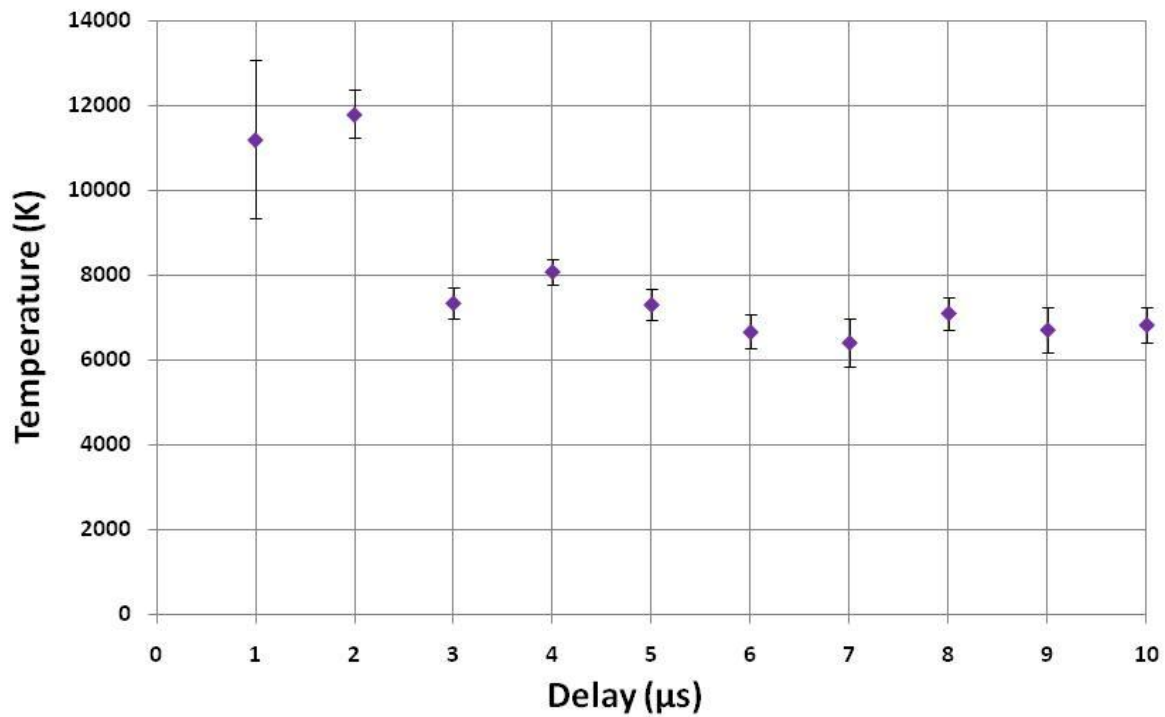


Figure 5-7. Temperatures calculated from the direct line fluorescence at 614.171 nm about 1 mm from the surface.

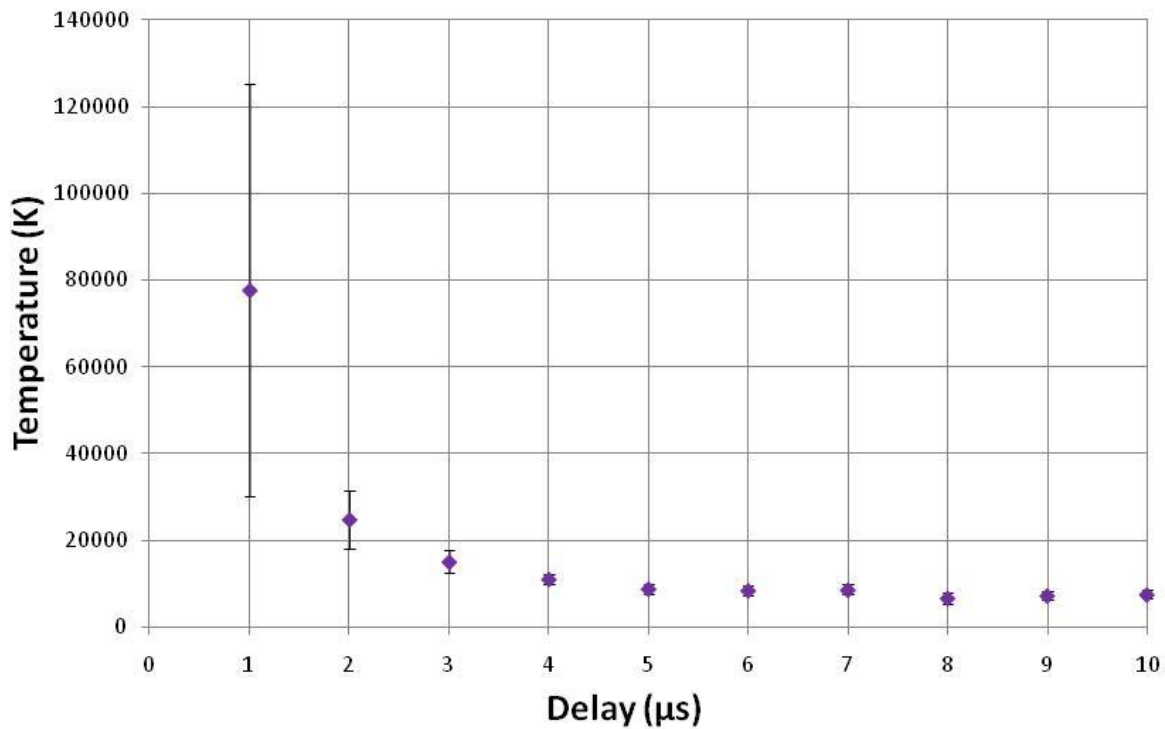


Figure 5-8. Temperatures calculated from the direct line fluorescence at 614.171 nm grazing the surface.

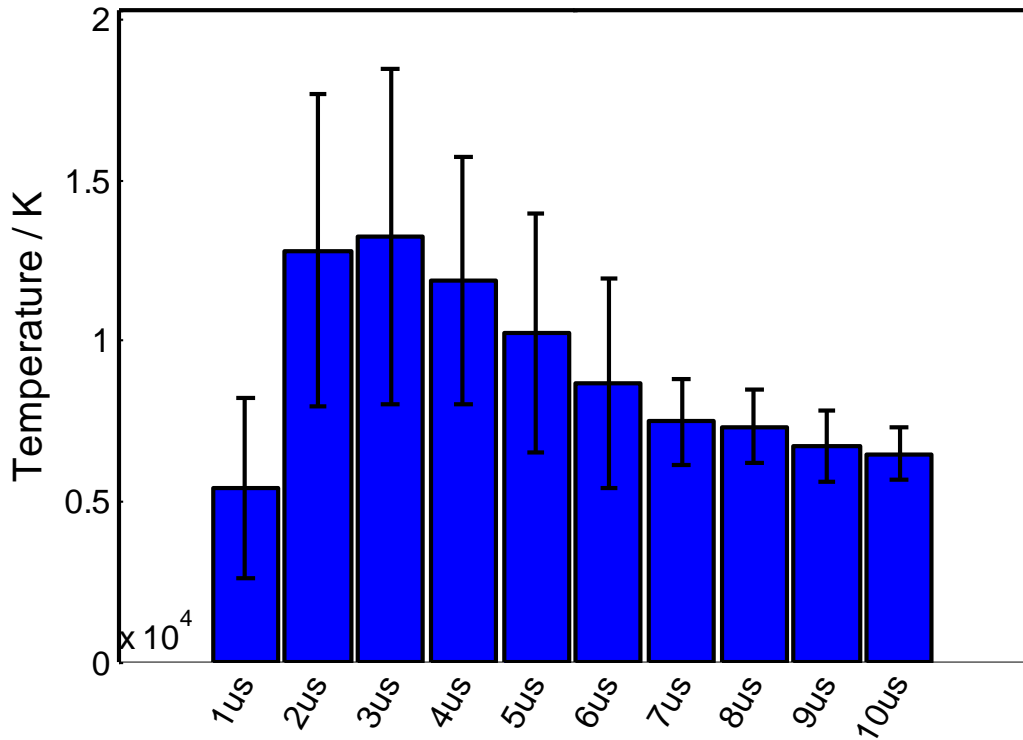


Figure 5-9. Temperatures calculated using the conventional Boltzmann plot method on D33 aluminum alloy under the same conditions as the Ba II studies.

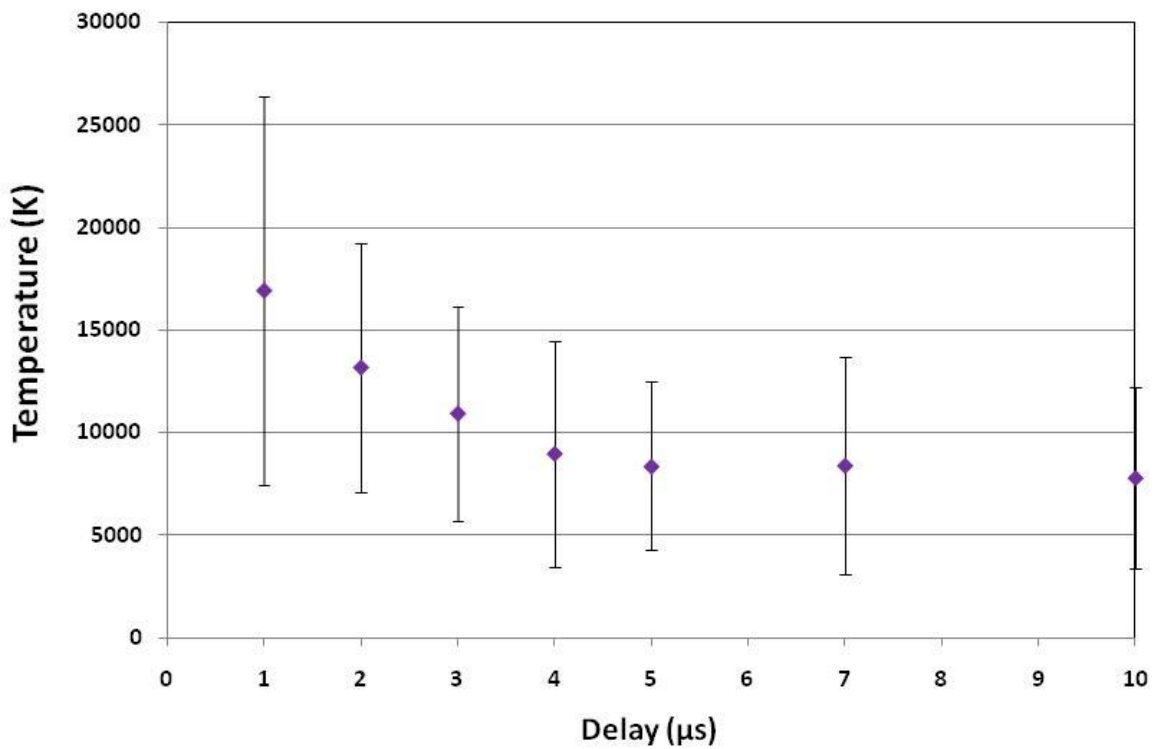


Figure 5-10. Temperatures calculated with errors propagated from interpulse standard deviations.

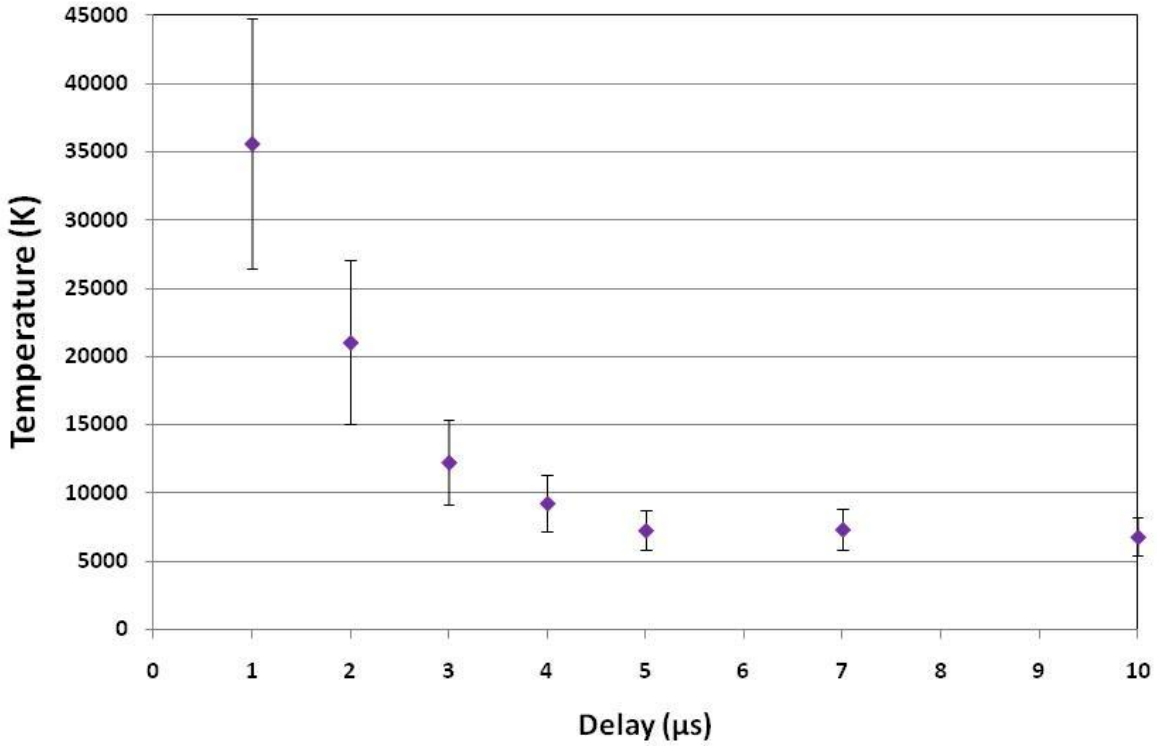


Figure 5-11. Temperatures calculated from the direct line fluorescence at 489.997 nm after excitation by 452.493 nm.

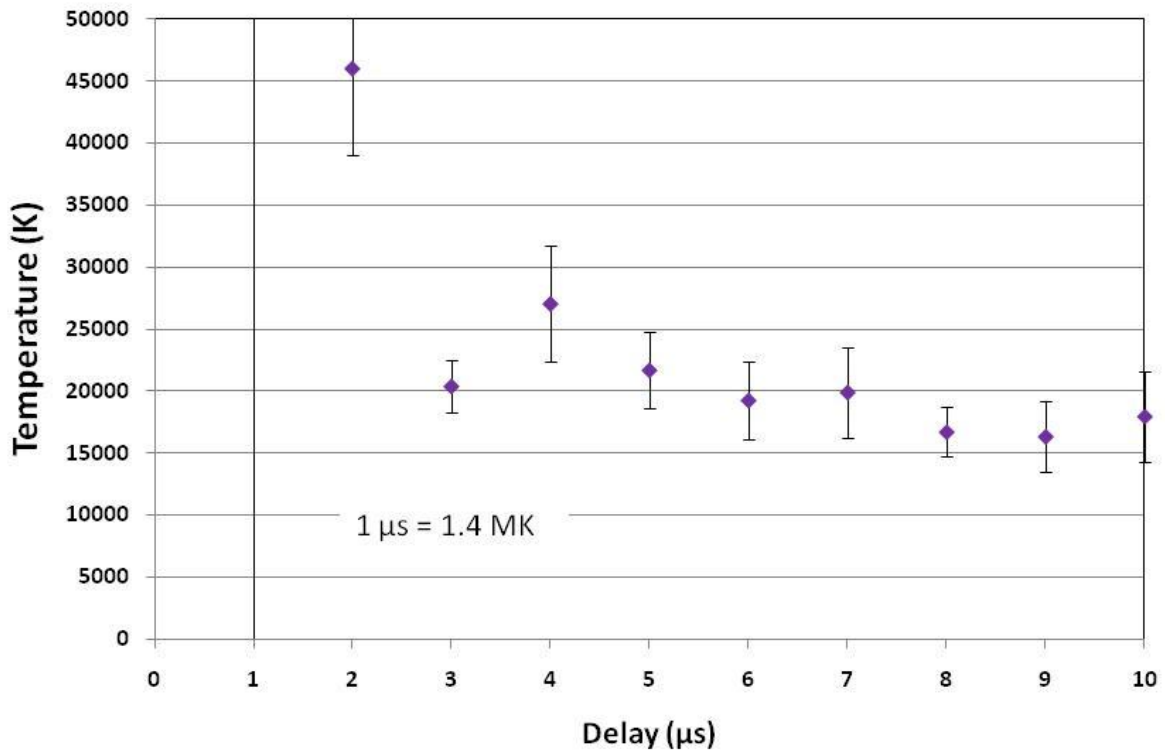


Figure 5-12. Temperatures calculated from the collisionally coupled emission at 389.178 nm after excitation by 455.403 nm.

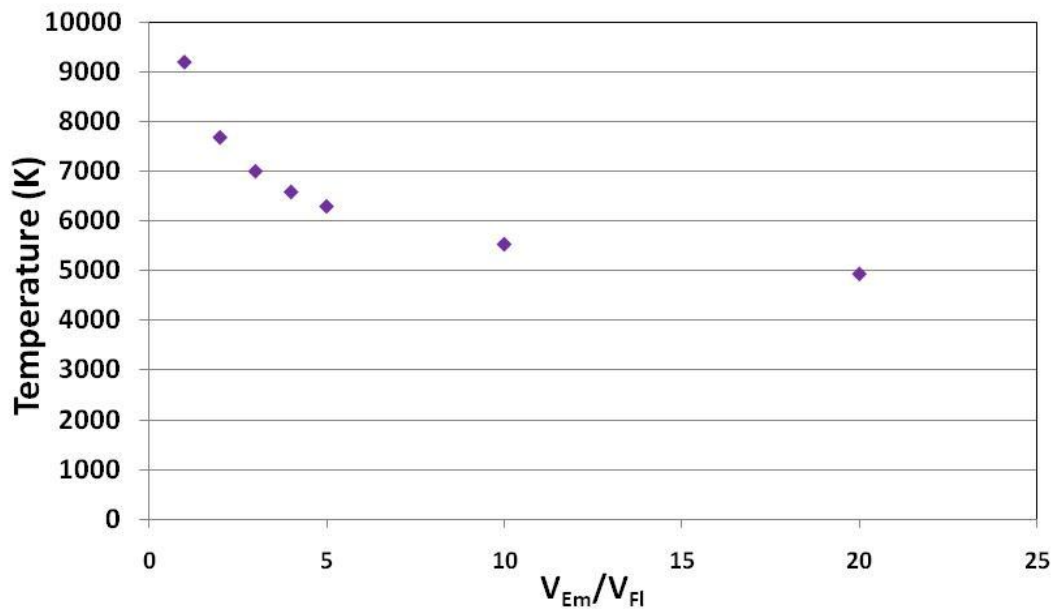


Figure 5-13. Temperature correction for volume ratio between emission and fluorescence. Data used here is typical for 4 μ s delay.

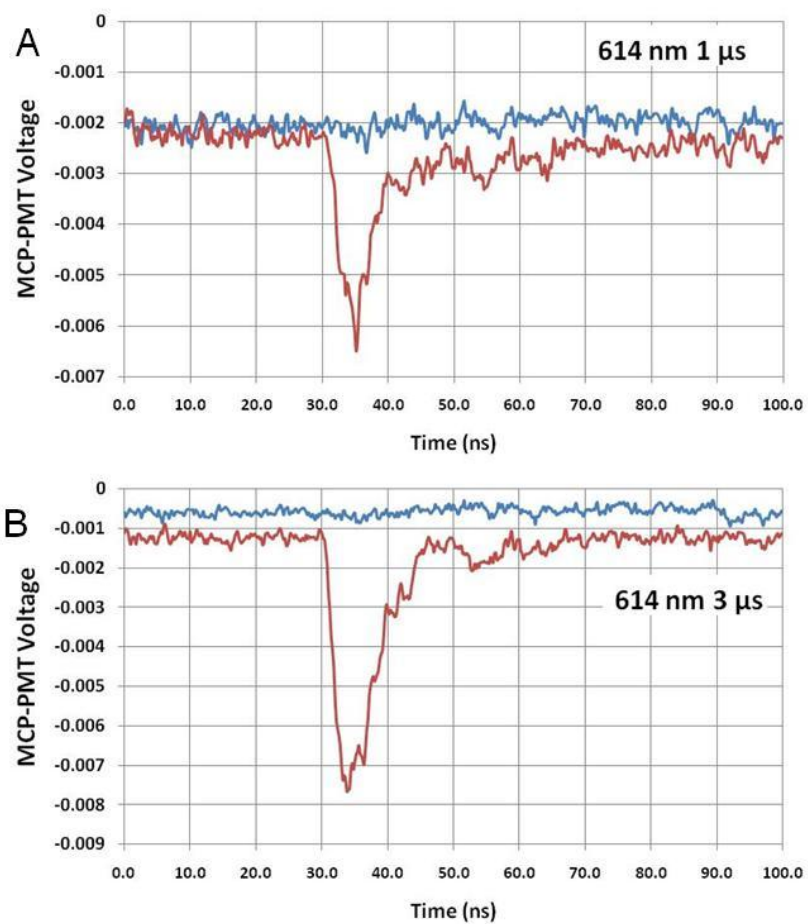


Figure 5-14. 614.171 nm emission and fluorescence traces. A) 1 μ s. B) 3 μ s.

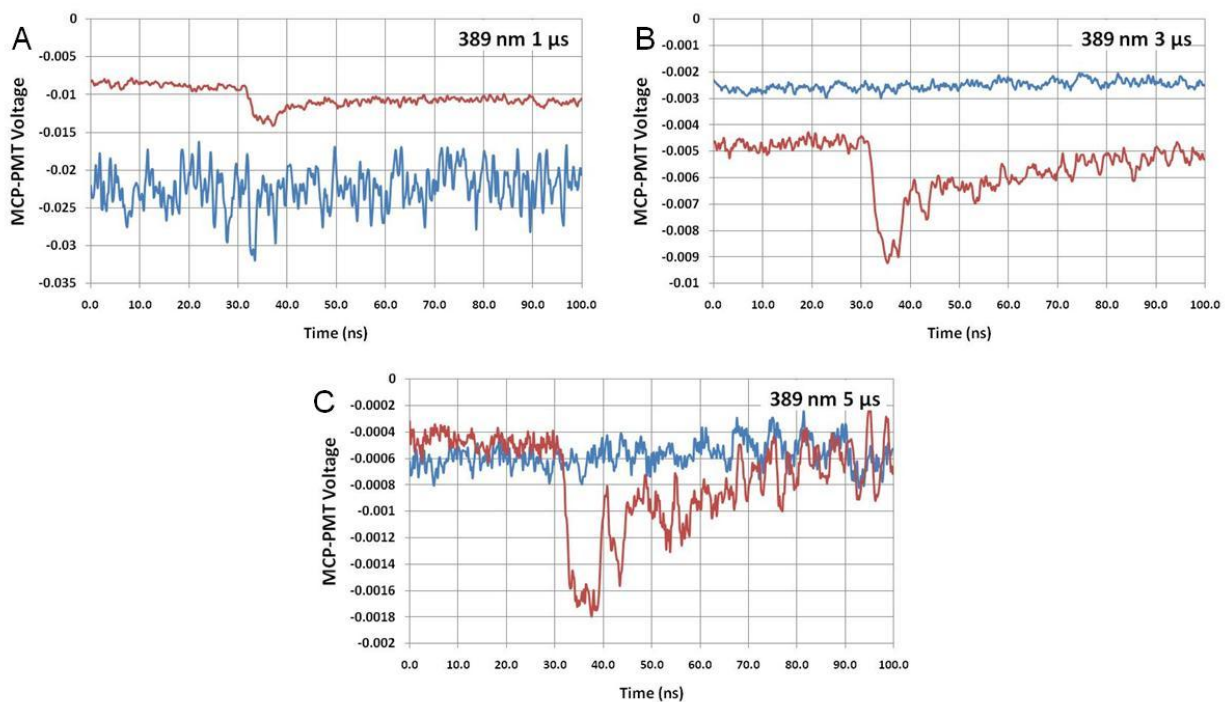


Figure 5-15. 389.178 nm emission and fluorescence traces. A) 1 μ s. B) 3 μ s. C) 5 μ s.

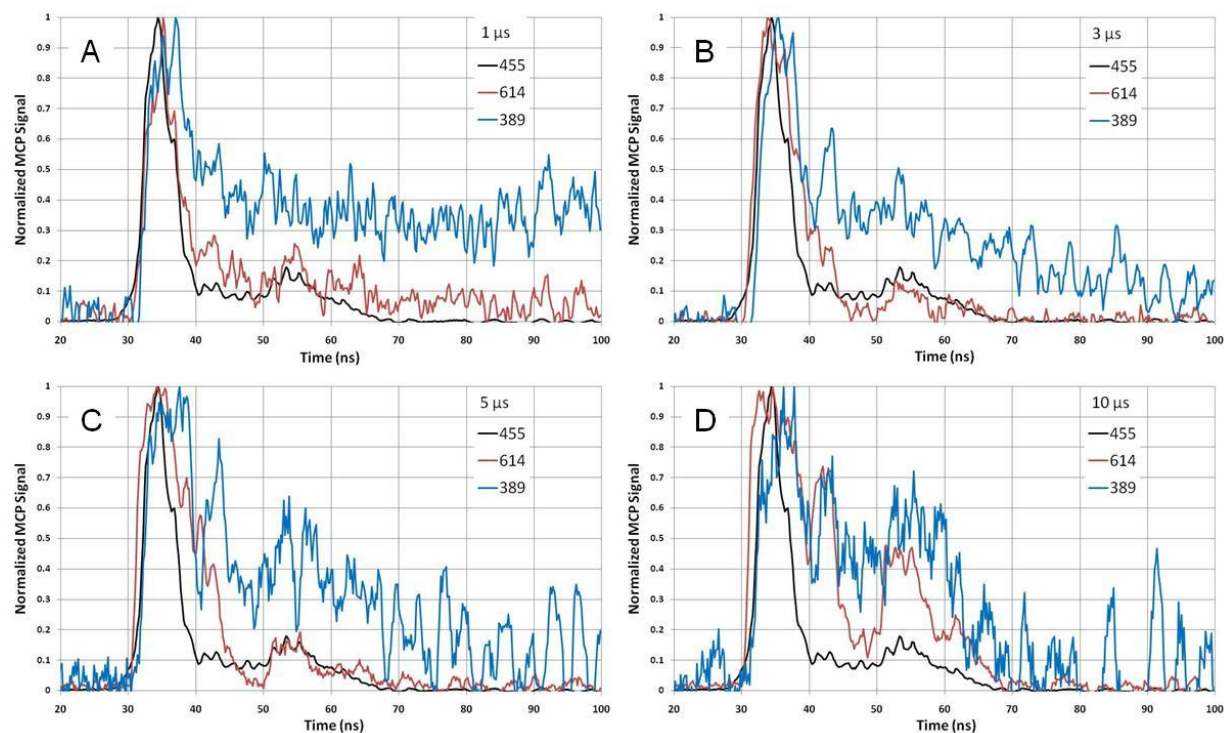


Figure 5-16. Fluorescence traces for 614.171 and 389.178 nm along with scatter from the excitation laser at 455.403 nm. A) 1 μ s. B) 3 μ s. C) 5 μ s. D) 10 μ s.

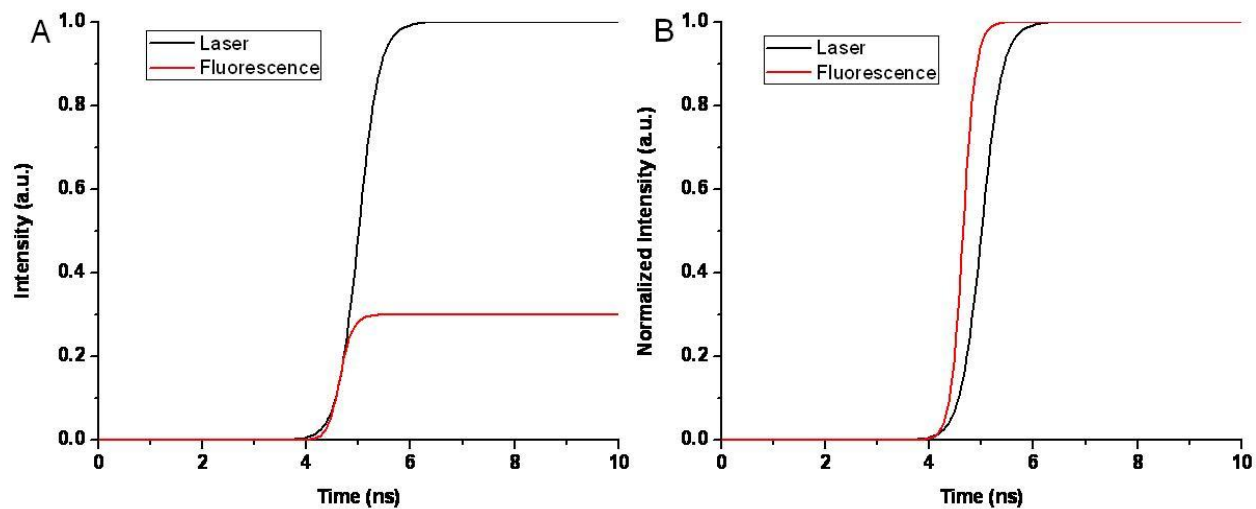


Figure 5-17. Effect of normalization on a saturated fluorescence signal. A) Raw signal of probe laser and fluorescence. B) Normalized signals.

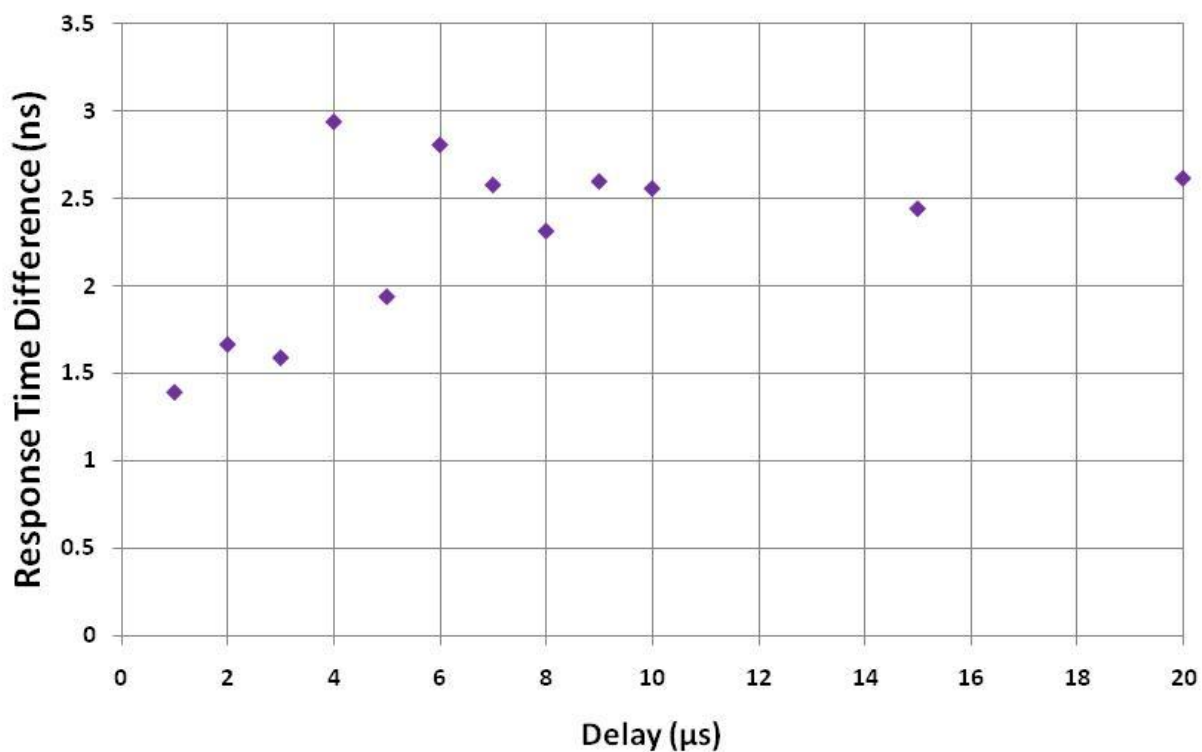


Figure 5-18. Response times calculated from difference between the half intensity of the direct line fluorescence at 614.171 nm and collisionally coupled line at 389.178 nm.

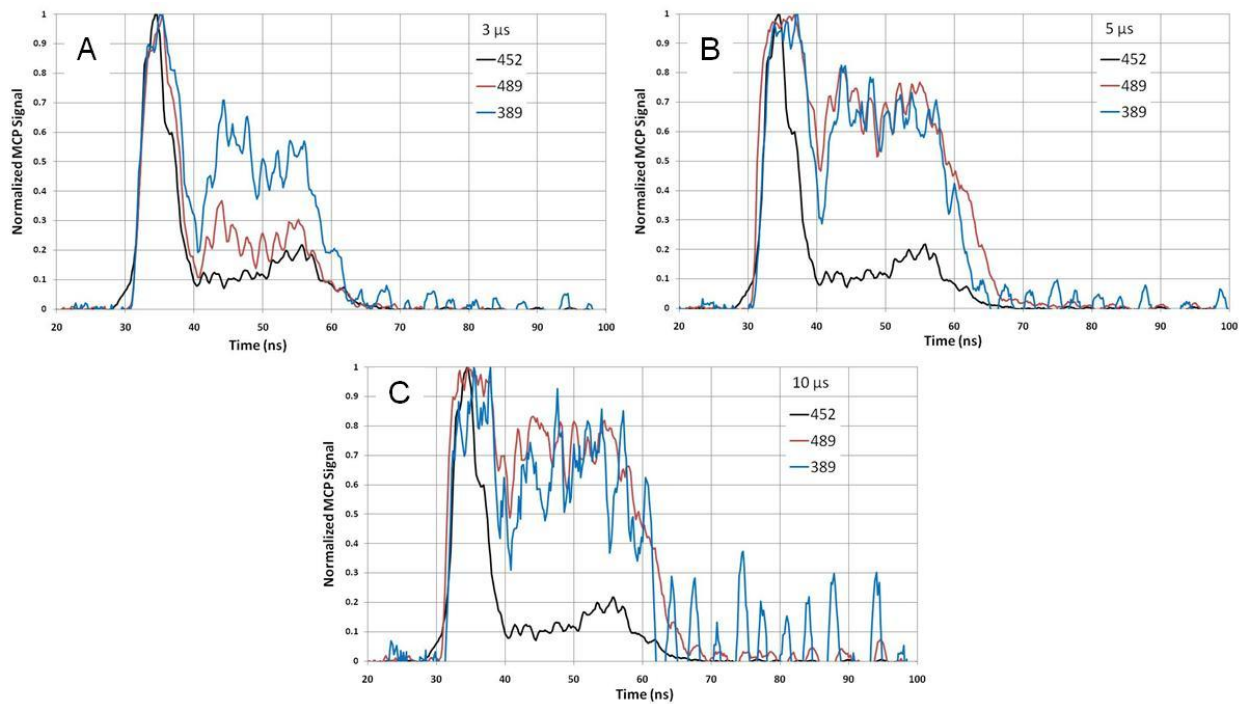


Figure 5-19. Fluorescence traces for 489.997 and 389.178 nm along with scatter from the excitation laser at 452.493 nm. The traces correspond to four delays within the plasma. A) 3 μ s. B) 5 μ s. C) 10 μ s.

CHAPTER 6 CONCLUSIONS

Completed Project Goals

Presented herein is an experimental setup that combines the benefits of emission, fluorescence and imaging. Each of these techniques exhibits resolution for space and time. It is possible to easily switch between emission and fluorescence detection with no alteration to the system. The addition of the schlieren imaging require only two optical elements to be added to the emission collection optics. These two optical elements do not replace or remove any pre-existing lenses or stops. Both pieces can be removed and replaced at no real detriment to either technique.

The emission study shows a very fine spatial distribution but suffers from a lack of sensitivity. The physical extent of the plasma observed is smaller than the emissive volume observed during the spatially resolved fluorescence work. The highly selective optical collection requires a much more sensitive detector. With such a device, many more spatial points of collection could be added to the periphery of the map investigated here. Additionally, a more sensitive detector would be able to pull the weak lines out of the background or wings of neighboring lines. With more analytical lines for investigation, a more thorough application of CF-LIBS would be possible. Despite this limitation, very clear trends are observed for atomic emission and ionic emission. Atomic emission is strongest near the surface of the sample which agrees with the temperature distribution determined by the CF-LIBS program. While the distribution of electron number densities are more erratic, the magnitude of the densities agrees well with previous observed values. This is an encouraging fact that may indicate minor

adjustments to the technique may resolve a structure to the electron number density distribution.

Schlieren imaging studied with this setup agrees well with the theoretical expansion of a shockwave. Additionally, similar trends observed herein were reported by other LIP research groups. This useful imaging technique is applied while being minimally invasive to the existing emission and fluorescence setups.

Spatially and time-resolved LIF measurements show promise for quantitative mapping of the atoms and ions within the plasma plume. While other work has been published featuring images of LIF within a plume, the technique executed within this work looks to give these values hard numbers by splicing the technique with the time-of-flight technique. By monitoring a window within space and changing the delay time, the change of atomic and ionic distributions within the plume is very clear.

Finally, a thorough look into the dynamics of the plasma are conducted using barium ion. The application of a new, single-line temperature measurement is executed and a simultaneous investigation into collisional coupling of states is possible. The time-resolved data, while clearly indicating the time scale in which collisional rates among the various levels occur, can only be seen from a qualitative point of view. In addition, the fluorescence temperature measurement is not without its limitations. The evaluation of the technique made it clear that very specific energy level systems must be used to accurately implement the method. Observation volume considerations hinder the application of this new temperature technique.

Future Project Goals

Future work on the system will refine the methods already outlined by this document. Specifically, the space-resolved emission measurements would benefit from

a more sensitive detector behind the spectrograph. This increase in sensitivity could decrease the time window of the measurement and allow for investigating the weaker emissivity of the plume edges. A more detailed investigation into the time dependence of such measurements would require the use of an echelle spectrograph. Repeating the analysis with a conventional grating spectrograph is unrealistic for both time and data management. The requirement of repeated measurements over the span of days introduces too many sources for noise or drift.

The future of the schlieren studies should seek to mimic the contrast and magnification observed by Vogel [106]. Such a refinement to the system may require more alteration to the emission collection optics. Specifically, a larger focal length lens may be required to collimate the refracted light from the plasma. By extending that working arm, the displacement from center will also increase. This increased displacement results in an easier segregation between refracted and undisturbed light. A real improvement to the system could be realized with the use of a proper imaging camera. Scientific cameras, while sensitive, lack the spatial resolution for detailed work.

The fluorescence techniques can be applied to many other analytes in other matrices. The spatially resolved measurements have a dimension of information ignored here. By marrying the time-of-flight and imaging techniques, the spatially resolved information retains the spectral width of each line observed. In this work, only the fluorescence intensities were evaluated, but an investigation into the spectral line widths is possible with this instrumentation. Temperatures calculated with this setup need to be confirmed using the two wavelength method described in the discussion. Meanwhile, the collisional dynamics of the system could be investigated as a function of

pressure or ablation laser power. These simple variables could shed light on the connection between plasma formation and electron number densities well into the life of the plasma. The qualitative interpretation of the collisional dynamics needs to be examined by a detailed rate equation approach. This future work will focus on the rates of population and depopulation for selected atomic and ionic levels.

Finally, the absorption abilities of the system need to be evaluated completely. This work builds upon the dissertation of Dr. Benoit Lauly [66]. While much of his work was done with transmission imaging of Cs within a plasma plume, the design of the instrument in this work focuses on the interrogation of an Ar line at 852.144 nm. With this convenient line, LIP's can be formed on any matrix under an Ar atmosphere and allow for interrogation of the plasma structure. Some preliminary results in this vein are shown in Figure 6-1. No data manipulation is done on this data save for an arbitrary offset introduced to give all traces the same initial intensity. As the signal moves up to less negative values, the laser intensity is being attenuated by the plasma. The legend to the right shows the frequency difference from the Ar line center. A plasma is formed on an aluminum sample, D33, under an argon atmosphere. At earlier delay times, the argon transition is wider, showing absorption of the laser diode out to 10 GHz from the line center. This width is much reduced by 3.5 μ s where little attenuation is seen even 3.3 GHz off peak. The shared attenuation earlier than 1 μ s is attributed to the phenomenon described in Chapter 3. Plasma and shockwave formation can change the refractive index near the sample surface which can deflect the diode laser beam. This investigation is in its infancy and can use some refining. For now, the method is

setup for monochromator detection which ignores spatial information. Future work should aim to integrate imaging techniques similar to the work of Dr. Lauly.

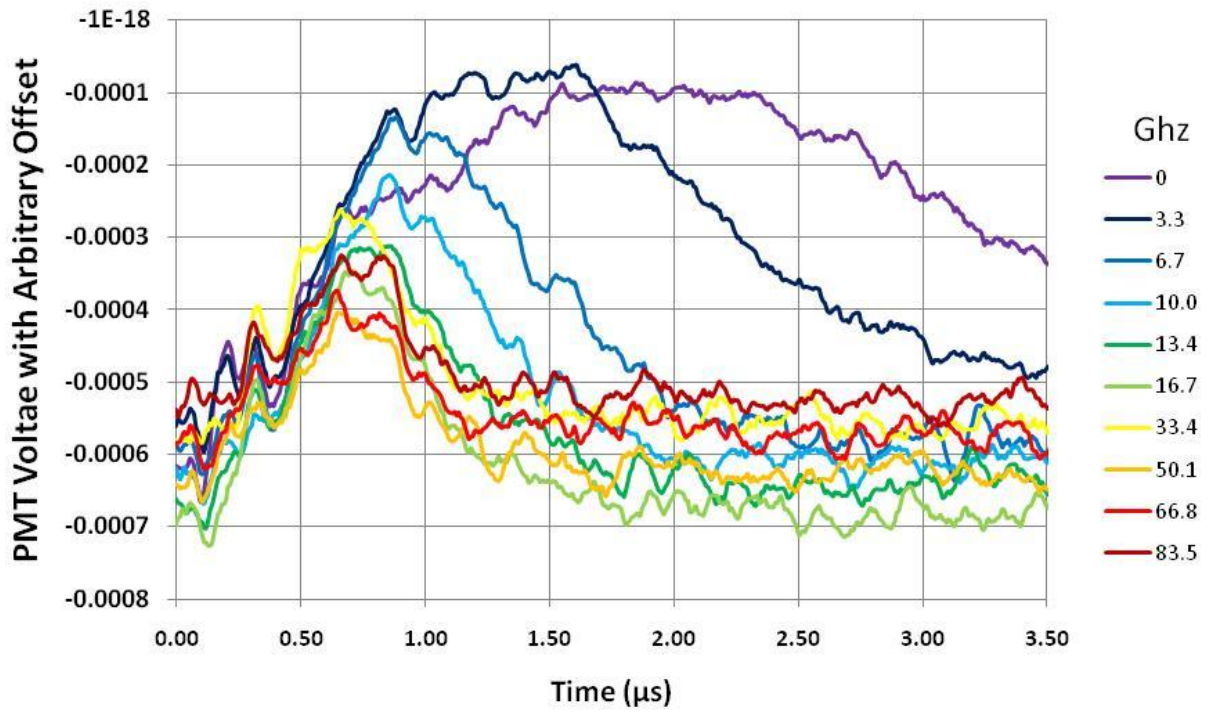


Figure 6-1. Absorption of a diode laser as it is tuned away from the center of an argon metastable absorption profile. The legend indicates the spectral distance from the center.

LIST OF REFERENCES

1. D.W. Hahn and N. Omenetto, Laser-induced breakdown spectroscopy (libs), part i: Review of basic diagnostics and plasma-particle interactions: Still-challenging issues within the analytical plasma community, *Applied Spectroscopy* 64 (2010) 335A-366A.
2. J. Miller, R. Haglund, and R. Dreyfus, Mechanisms of laser ablation of monolayers as determined by laser-induced fluorescence measurements, in *Laser ablation mechanisms and applications 1991*, Springer Berlin / Heidelberg. 209-212.
3. J.A. Aguilera and C. Aragon, A comparison of the temperatures and electron densities of laser-produced plasmas obtained in air, argon, and helium at atmospheric pressure, *Applied Physics a-Materials Science & Processing* 69 (1999) S475-S478.
4. J.A. Aguilera and C. Aragon, Temperature and electron density distributions of laser-induced plasmas generated with an iron sample at different ambient gas pressures, *Applied Surface Science* 197 (2002) 273-280.
5. R.C. Rosan, M.K. Healy, and W.F. McNary, Jr., Spectroscopic ultramicroanalysis with a laser, *Science* 142 (1963) 236-237.
6. D.W. Koopman, Ion emission from laser-produced plasmas, *Physics of Fluids* 10 (1967) 2091-2093.
7. D.W. Koopman, Langmuir probe and microwave measurements of properties of streaming plasmas generated by focused laser pulses, *Physics of Fluids* 14 (1971) 1707-1716.
8. K.A. Saum and D.W. Koopman, Discharges guided by laser-induced rarefaction channels, *Physics of Fluids* 15 (1972) 2077-2079.
9. T.R. Loree and L.J. Radziemski, Laser-induced breakdown spectroscopy: Time-integrated applications, *Plasma Chemistry and Plasma Processing* 1 (1981) 271-279.
10. H.S. Kwong and R.M. Measures, Trace-element laser microanalyzer with freedom from chemical matrix effect, *Analytical Chemistry* 51 (1979) 428-432.

11. D.A. Cremers and L.J. Radziemski, Detection of chlorine and fluorine in air by laser-induced breakdown spectrometry, *Analytical Chemistry* 55 (1983) 1252-1256.
12. L.J. Radziemski, T.R. Loree, D.A. Cremers, and N.M. Hoffman, Time-resolved laser-induced breakdown spectrometry of aerosols, *Analytical Chemistry* 55 (1983) 1246-1252.
13. G. Herziger and E.W. Kreutz, Fundamentals of laser microprocessing of metals, *Physica Scripta T13* (1986) 139-146.
14. W. Sdorra, J. Brust, and K. Niemax, Basic investigations for laser microanalysis .4. The dependence on the laser wavelength in laser ablation, *Mikrochimica Acta* 108 (1992) 1-10.
15. K. Niemax, Laser ablation - reflections on a very complex technique for solid sampling, *Fresenius Journal of Analytical Chemistry* 370 (2001) 332-340.
16. W. Sdorra and K. Niemax, Basic investigations for laser microanalysis .3. Application of different buffer gases for laser-produced sample plumes, *Mikrochimica Acta* 107 (1992) 319-327.
17. I. Horn, M. Guillong, and D. Günther, Wavelength dependant ablation rates for metals and silicate glasses using homogenized laser beam profiles - implications for la-icp-ms, *Applied Surface Science* 182 (2001) 91-102.
18. B.C. Windom and D.W. Hahn, Laser ablation-laser induced breakdown spectroscopy (la-libs): A means for overcoming matrix effects leading to improved analyte response, *Journal of Analytical Atomic Spectrometry* 24 (2009) 1665-1675.
19. B.C. Castle, K. Talabardon, B.W. Smith, and J.D. Winefordner, Variables influencing the precision of laser-induced breakdown spectroscopy measurements, *Applied Spectroscopy* 52 (1998) 649-657.
20. B.H. Soffer and McFarlan.Bb, Continuously tunable narrow-band organic dye lasers, *Applied Physics Letters* 10 (1967) 266-267.

21. R.M. Measures, Selective excitation spectroscopy and some possible applications, *Journal of Applied Physics* 39 (1968) 5232-5245.
22. M.R. Bowman, A.J. Gibson, and M.C. Sandford, Atmospheric sodium measured by a tuned laser radar, *Nature* 221 (1969) 456-457.
23. N. Omenetto, H.G.C. Human, P. Cavalli, and G. Rossi, Direct determination of lead in blood by laser-excited flame atomic-fluorescence spectrometry, *Analyst* 109 (1984) 1067-1070.
24. M. Leong, J. Vera, B.W. Smith, N. Omenetto, and J.D. Winefordner, Laser-induced double-resonance fluorescence of lead with graphite tube atomization, *Analytical Chemistry* 60 (1988) 1605-1610.
25. B.W. Smith, N. Omenetto, and J.D. Winefordner, Laser-excited atomic fluorescence in a pulsed glow-discharge, *Spectrochimica Acta Part B-Atomic Spectroscopy* 39 (1984) 1389-1393.
26. B.W. Smith, J.B. Womack, N. Omenetto, and J.D. Winefordner, Approaching single atom detection with atomic fluorescence in a glow-discharge atom reservoir, *Applied Spectroscopy* 43 (1989) 873-876.
27. N. Omenetto, H.G.C. Human, P. Cavalli, and G. Rossi, Laser-excited atomic and ionic non-resonance fluorescence detection limits for several elements in an argon inductively coupled plasma, *Spectrochimica Acta Part B-Atomic Spectroscopy* 39 (1984) 115-117.
28. M. Glick, B.W. Smith, and J.D. Winefordner, Laser-excited atomic fluorescence in a pulsed hollow-cathode glow-discharge, *Analytical Chemistry* 62 (1990) 157-161.
29. R.M. Measures, N. Drewell, and H.S. Kwong, Atomic lifetime measurements obtained by use of laser ablation and selective excitation spectroscopy, *Physical Review A* 16 (1977) 1093-1097.
30. G. Zizak, N. Omenetto, and J.D. Winefordner, Laser-excited atomic fluorescence techniques for temperature-measurements in flames - a summary, *Optical Engineering* 23 (1984) 749-755.

31. R.M. Measures and P.G. Cardinal, Laser ionization based on resonance saturation - a simple-model description, *Physical Review A* 23 (1981) 804-815.
32. N. Omenetto, B.W. Smith, and L.P. Hart, Laser-induced fluorescence and ionization spectroscopy - theoretical and analytical considerations for pulsed sources, *Fresenius Zeitschrift Fur Analytische Chemie* 324 (1986) 683-697.
33. R.M. Measures and H.S. Kwong, Tablaser - trace (element) analyzer based on laser ablation and selectively excited radiation, *Applied Optics* 18 (1979) 281-286.
34. S. Laville, C. Goueguel, H. Loudyi, F. Vidal, M. Chaker, and M. Sabsabi, Laser-induced fluorescence detection of lead atoms in a laser-induced plasma: An experimental analytical optimization study, *Spectrochimica Acta Part B-Atomic Spectroscopy* 64 (2009) 347-353.
35. M.R. Arnfield and R.M. Measures, Ion-to-neutral-atom measurements within an ablation plasma through laser selective-excitation spectroscopy, *Physical Review A* 24 (1981) 535-539.
36. R.W. Dreyfus, R. Kelly, and R.E. Walkup, Laser-induced fluorescence studies of excimer laser ablation of Al_2O_3 , *Applied Physics Letters* 49 (1986) 1478-1480.
37. R. Srinivasan, B. Braren, R.W. Dreyfus, L. Hadel, and D.E. Seeger, Mechanism of the ultraviolet-laser ablation of poly(methyl methacrylate) at 193 and 248 nm - laser-induced fluorescence analysis, chemical-analysis, and doping studies, *Journal of the Optical Society of America B-Optical Physics* 3 (1986) 785-791.
38. H. Masuhara, S. Eura, H. Fukumura, and A. Itaya, Laser ablation dynamics of poly(n-vinylcarbazole) film as revealed by time-resolved fluorescence spectroscopy, *Chemical Physics Letters* 156 (1989) 446-449.
39. M.A. Cappelli, P.H. Paul, and R.K. Hanson, Laser-induced fluorescence imaging of laser-ablated barium, *Applied Physics Letters* 56 (1990) 1715-1718.
40. A.D. Sappey and T.K. Gamble, Planar laser-induced fluorescence imaging of Cu atom and Cu-2 in a condensing laser-ablated copper plasma plume, *Journal of Applied Physics* 72 (1992) 5095-5107.

41. Y. Nakata, H. Kaibara, T. Okada, and M. Maeda, Two-dimensional laser-induced fluorescence imaging of a pulsed-laser deposition process of $\text{YBa}_2\text{Cu}_3\text{O}_{7-x}$, *Journal of Applied Physics* 80 (1996) 2458-2466.
42. J. Hermann, C. Boulmerleborgne, B. Dubreuil, and I.N. Mihailescu, Investigation by laser-induced fluorescence of surface vaporization during the pulsed CO_2 -laser irradiation of a titanium sample in an ambient gas, *Journal of Applied Physics* 71 (1992) 5629-5634.
43. T. Okada, N. Shibamaru, Y. Nakayama, and M. Maeda, Time-of-flight measurement of particles with laser-induced fluorescence in the plume produced by laser ablation of $\text{YBa}_2\text{Cu}_3\text{O}_{7-x}$ target, *Japanese Journal of Applied Physics Part 2-Letters* 31 (1992) L367-L369.
44. Y. Oki, T. Tani, N. Kidera, and M. Maeda, Trace-element analysis by laser-ablation atomic fluorescence spectroscopy, *Optics Communications* 110 (1994) 298-302.
45. B.W. Smith, I.B. Gornushkin, L.A. King, and J.D. Winefordner, A laser ablation-atomic fluorescence technique for isotopically selective determination of lithium in solids, *Spectrochimica Acta Part B-Atomic Spectroscopy* 53 (1998) 1131-1138.
46. B.W. Smith, A. Quentmeier, M. Bolshov, and K. Niemax, Measurement of uranium isotope ratios in solid samples using laser ablation and diode laser-excited atomic fluorescence spectrometry, *Spectrochimica Acta Part B-Atomic Spectroscopy* 54 (1999) 943-958.
47. A. Quentmeier, W. Sdorra, and K. Niemax, Internal standardization in laser-induced fluorescence spectrometry of microplasmas produced by laser ablation of solid samples, *Spectrochimica Acta Part B-Atomic Spectroscopy* 45 (1990) 537-546.
48. I.B. Gornushkin, S.A. Baker, B.W. Smith, and J.D. Winefordner, Determination of lead in metallic reference materials by laser ablation combined with laser excited atomic fluorescence, *Spectrochimica Acta Part B-Atomic Spectroscopy* 52 (1997) 1653-1662.
49. R.E. Neuhauser, U. Panne, R. Niessner, G.A. Petrucci, P. Cavalli, and N. Omenetto, On-line and in-situ detection of lead aerosols by plasma-spectroscopy and laser-excited atomic fluorescence spectroscopy, *Analytica Chimica Acta* 346 (1997) 37-48.

50. M.K. Kim, H. Ishii, K. Taoka, Y. Oki, and M. Maeda, Nanometer-scale surface element analysis in polymers using laser ablation atomic fluorescence spectroscopy, *Journal of Applied Physics* 87 (2000) 1029-1033.
51. F. Hilbk-Kortenbruck, R. Noll, P. Wintjens, H. Falk, and C. Becker, Analysis of heavy metals in soils using laser-induced breakdown spectroscopy combined with laser-induced fluorescence, *Spectrochimica Acta Part B-Atomic Spectroscopy* 56 (2001) 933-945.
52. H.H. Telle, D.C.S. Beddows, G.W. Morris, and O. Samek, Sensitive and selective spectrochemical analysis of metallic samples: The combination of laser-induced breakdown spectroscopy and laser-induced fluorescence spectroscopy, *Spectrochimica Acta Part B-Atomic Spectroscopy* 56 (2001) 947-960.
53. C.B. Stipe, D. Lucas, C.P. Koshland, and R.F. Sawyer, Soot particle disintegration and detection by two-laser excimer laser fragmentation fluorescence spectroscopy, *Applied Optics* 44 (2005) 6537-6544.
54. Y. Godwal, S.L. Lui, M.T. Taschuk, Y. Tsui, and R. Fedosejevs, Determination of lead in water using laser ablation-laser induced fluorescence, *Spectrochimica Acta Part B-Atomic Spectroscopy* 62 (2007) 1443-1447.
55. K. Sasaki and H. Watarai, Dynamics of laser-ablation plume and ambient gas visualized by laser-induced fluorescence imaging spectroscopy, *Japanese Journal of Applied Physics Part 2-Letters & Express Letters* 45 (2006) L447-L449.
56. H. Loudyi, K. Rifai, S. Laville, F. Vidal, M. Chaker, and M. Sabsabi, Improving laser-induced breakdown spectroscopy (libs) performance for iron and lead determination in aqueous solutions with laser-induced fluorescence (lif), *Journal of Analytical Atomic Spectrometry* 24 (2009) 1421-1428.
57. X.K. Shen, H. Wang, Z.Q. Xie, Y. Gao, H. Ling, and Y.F. Lu, Detection of trace phosphorus in steel using laser-induced breakdown spectroscopy combined with laser-induced fluorescence, *Applied Optics* 48 (2009) 2551-2558.
58. F. Colao, V. Lazic, R. Fantoni, and S. Pershin, A comparison of single and double pulse laser-induced breakdown spectroscopy of aluminum samples, *Spectrochimica Acta Part B-Atomic Spectroscopy* 57 (2002) 1167-1179.

59. R.M. Measures, N. Drewell, and P. Cardinal, Laser interaction based on resonance saturation (libors) - alternative to inverse bremsstrahlung for coupling laser energy into a plasma, *Applied Optics* 18 (1979) 1824-1827.
60. S.Y. Chan and N.H. Cheung, Analysis of solids by laser ablation and resonance-enhanced laser-induced plasma spectroscopy, *Analytical Chemistry* 72 (2000) 2087-2092.
61. J.D. Wu and N.H. Cheung, Resonance-enhanced laser-induced plasma spectroscopy for multielement analysis in laser ablative sampling, *Applied Spectroscopy* 55 (2001) 366-370.
62. C. Goueguel, S. Laville, F. Vidal, M. Sabsabi, and M. Chaker, Investigation of resonance-enhanced laser-induced breakdown spectroscopy for analysis of aluminium alloys, *Journal of Analytical Atomic Spectrometry* 25 (2010) 635-644.
63. G.C. Eiden, J.E. Anderson, and N.S. Nogar, Resonant laser-ablation - semiquantitative aspects and threshold effects, *Microchemical Journal* 50 (1994) 289-300.
64. *Application 2: Selecting the right lens*. Optics Application Examples [cited 2011 June 11]; Available from: <http://www.edmundoptics.com/technical-support/optics/optics-application-examples/?pagenum=4>.
65. A.P. Thorne, *Spectrophysics*, Chapman and Hall Ltd, London, 1974.
66. B. Lauly, *Diode laser diagnostics of laser-induced plasmas and atomic vapor cells*, 2008, University of Florida, Department of Chemistry
67. T. Sakka, T. Nakajima, and Y.H. Ogata, Spatial population distribution of laser ablation species determined by self-reversed emission line profile, *Journal of Applied Physics* 92 (2002) 2296-2303.
68. H.R. Pakhal, R.P. Lucht, and N.M. Laurendeau, Spectral measurements of incipient plasma temperature and electron number density during laser ablation of aluminum in air, *Applied Physics B-Lasers and Optics* 90 (2008) 15-27.
69. I.B. Gornushkin, S.V. Shabanov, S. Merk, E. Tognoni, and U. Panne, Effects of non-uniformity of laser induced plasma on plasma temperature and

- concentrations determined by the boltzmann plot method: Implications from plasma modeling, *Journal of Analytical Atomic Spectrometry* 25 (2010) 1643-1653.
70. J.A. Aguilera and C. Aragon, Characterization of a laser-induced plasma by spatially resolved spectroscopy of neutral atom and ion emissions. Comparison of local and spatially integrated measurements, *Spectrochimica Acta Part B-Atomic Spectroscopy* 59 (2004) 1861-1876.
 71. J.A. Aguilera, J. Bengoechea, and C. Aragon, Spatial characterization of laser induced plasmas obtained in air and argon with different laser focusing distances, *Spectrochimica Acta Part B-Atomic Spectroscopy* 59 (2004) 461-469.
 72. J.A. Aguilera and C. Aragon, Multi-element saha-boltzmann and boltzmann plots in laser-induced plasmas, *Spectrochimica Acta Part B-Atomic Spectroscopy* 62 (2007) 378-385.
 73. J.A. Aguilera, C. Aragon, and J. Bengoechea, Spatial characterization of laser-induced plasmas by deconvolution of spatially resolved spectra, *Applied Optics* 42 (2003) 5938-5946.
 74. J. James D. Ingle and S.R. Crouch, *Spectrochemical analysis*, Prentice Hall, Upper Saddle River, 1988.
 75. S. Yalcin, D.R. Crosley, G.P. Smith, and G.W. Faris, Influence of ambient conditions on the laser air spark, *Applied Physics B-Lasers and Optics* 68 (1999) 121-130.
 76. H.R. Griem, A.C. Kolb, and K.Y. Shen, Stark broadening of hydrogen lines in a plasma, *Physical Review* 116 (1959) 4-16.
 77. J.B. Simeonsson and A.W. Miziolek, Time-resolved emission studies of arf-laser-produced microplasmas, *Applied Optics* 32 (1993) 939-947.
 78. C. Parigger, D.H. Plemmons, and J.W.L. Lewis, Spatially and temporally resolved electron number density-measurements in a decaying laser-induced plasma using hydrogen-alpha line-profiles, *Applied Optics* 34 (1995) 3325-3330.

79. C. Aragon and J.A. Aguilera, Determination of the local electron number density in laser-induced plasmas by stark-broadened profiles of spectral lines comparative results from h-alpha, fe i and si ii lines, *Spectrochimica Acta Part B-Atomic Spectroscopy* 65 (2010) 395-400.
80. H.R. Griem, *Spectral line broadening by plasmas*, Academic Press Inc, New York, 1974.
81. A. Ciucci, M. Corsi, V. Palleschi, S. Rastelli, A. Salvetti, and E. Tognoni, New procedure for quantitative elemental analysis by laser-induced plasma spectroscopy, *Applied Spectroscopy* 53 (1999) 960-964.
82. A. Ciucci, V. Palleschi, S. Rastelli, A. Salvetti, D.P. Singh, and E. Tognoni, Cf-lips: A new approach to lips spectra analysis, *Laser and Particle Beams* 17 (1999) 793-797.
83. L.M. Cabalin and J.J. Laserna, Atomic emission spectroscopy of laser-induced plasmas generated with an annular-shaped laser beam, *Journal of Analytical Atomic Spectrometry* 19 (2004) 445-450.
84. X.Z. Zeng, X.L. Mao, S.S. Mao, S.B. Wen, R. Greif, and R.E. Russo, Laser-induced shockwave propagation from ablation in a cavity, *Applied Physics Letters* 88 (2006)
85. A. Bogaerts and Z.Y. Chen, Nanosecond laser ablation of cu: Modeling of the expansion in he background gas, and comparison with expansion in vacuum, *Journal of Analytical Atomic Spectrometry* 19 (2004) 1169-1176.
86. I.B. Gornushkin, A.Y. Kazakov, N. Omenetto, B.W. Smith, and J.D. Winefordner, Radiation dynamics of post-breakdown laser induced plasma, *Spectrochimica Acta Part B-Atomic Spectroscopy* 59 (2004) 401-418.
87. A. Casavola, G. Colonna, A. De Giacomo, and M. Capitelli, A combined fluid dynamic and chemical model to investigate the laser induced plasma expansion, *Applied Physics a-Materials Science & Processing* 79 (2004) 1315-1317.
88. W.T. Chan, A.P.K. Leung, X.L. Mao, and R.E. Russo, Effects of gas environment on picosecond laser ablation, *Applied Surface Science* 127 (1998) 269-273.

89. A.P.K. Leung, W.T. Chan, X.L. Mao, and R.E. Russo, Influence of gas environment on picosecond laser ablation sampling efficiency and icp conditions, *Analytical Chemistry* 70 (1998) 4709-4716.
90. A. Töpler, Optische studien nach der methode der schlierenbeobachtung, *Annalen der Physik* 207 (1867) 180-215.
91. H. Schardin, Die schlierenverfahren und ihre anwendungen, *Ergebnisse der Exakten Naturwissenschaften* 20 (1942) 303-439.
92. G.S. Settles, *Schlieren and shadowgraph techniques*, Springer-Verlag, Berlin, 2001.
93. S. Siano, R. Pini, R. Salimbeni, and M. Vannini, A diagnostic set-up for time-resolved imaging of laser-induced ablation, *Optics and Lasers in Engineering* 25 (1996) 1-12.
94. X.L. Mao, S.B. Wen, and R.E. Russo, Time resolved laser-induced plasma dynamics, *Applied Surface Science* 253 (2007) 6316-6321.
95. S.B. Wen, X.L. Mao, R. Greif, and R.E. Russo, Laser ablation induced vapor plume expansion into a background gas. II. Experimental analysis, *Journal of Applied Physics* 101 (2007)
96. J.F.Y. Gravel and D. Boudreau, Study by focused shadowgraphy of the effect of laser irradiance on laser-induced plasma formation and ablation rate in various gases, *Spectrochimica Acta Part B-Atomic Spectroscopy* 64 (2009) 56-66.
97. H. Schittenhelm, G. Callies, P. Berger, and H. Hugel, Two-wavelength interferometry on excimer laser induced vapour/plasma plumes during the laser pulse, *Applied Surface Science* 127 (1998) 922-927.
98. N. Vogel and N. Kochan, Interferometric diagnostic of picosecond laser ablation in air, *Applied Surface Science* 127 (1998) 928-934.
99. H. Sobral, M. Villagran-Muniz, R. Navarro-Gonzalez, and A.C. Raga, Temporal evolution of the shock wave and hot core air in laser induced plasma, *Applied Physics Letters* 77 (2000) 3158-3160.

100. M. Hauer, D.J. Funk, T. Lippert, and A. Wokaun, Time resolved study of the laser ablation induced shockwave, *Thin Solid Films* 453 (2004) 584-588.
101. M. Thiyagarajan and J. Scharer, Experimental investigation of ultraviolet laser induced plasma density and temperature evolution in air, *Journal of Applied Physics* 104 (2008)
102. J. Grun, J. Stamper, C. Manka, J. Resnick, R. Burris, J. Crawford, and B.H. Ripin, Instability of Taylor-Sedov blast waves propagating through a uniform gas, *Physical Review Letters* 66 (1991) 2738-2741.
103. M. Corsi, G. Cristoforetti, M. Hidalgo, D. Iriarte, S. Legnaioli, V. Palleschi, A. Salvetti, and E. Tognoni, Temporal and spatial evolution of a laser-induced plasma from a steel target, *Applied Spectroscopy* 57 (2003) 715-721.
104. G. Callies, P. Berger, and H. Hugel, Time-resolved observation of gas-dynamic discontinuities arising during excimer-laser ablation and their interpretation, *Journal of Physics D-Applied Physics* 28 (1995) 794-806.
105. G. Cristoforetti, S. Legnaioli, L. Pardini, V. Palleschi, A. Salvetti, and E. Tognoni, Spectroscopic and shadowgraphic analysis of laser induced plasmas in the orthogonal double pulse pre-ablation configuration, *Spectrochimica Acta Part B-Atomic Spectroscopy* 61 (2006) 340-350.
106. A. Vogel, I. Apitz, S. Freidank, and R. Dijkink, Sensitive high-resolution white-light schlieren technique with a large dynamic range for the investigation of ablation dynamics, *Optics Letters* 31 (2006) 1812-1814.
107. G. Taylor, The formation of a blast wave by a very intense explosion .2. The atomic explosion of 1945, *Proceedings of the Royal Society of London Series A-Mathematical and Physical Sciences* 201 (1950) 175-186.
108. Y.B. Zel'dovich and Y.P. Raizer, *Physics of shock waves and high-temperature hydrodynamic phenomena*, Dover, Mineola, 2002.
109. S.B. Wen, X.L. Mao, R. Greif, and R.E. Russo, Expansion of the laser ablation vapor plume into a background gas. I. Analysis, *Journal of Applied Physics* 101 (2007)

110. R.A. Armstrong, R.A. Lucht, and W.T. Rawlins, Spectroscopic investigation of laser-initiated low-pressure plasmas in atmospheric gases, *Applied Optics* 22 (1983) 1573-1577.
111. J. Halenka. *Fe01.Dat*. [cited May 25, 2011]; Available from: <http://draco.uni.opole.pl/~halenka/FE01.DAT>.
112. R.W. Dreyfus, R.E. Walkup, and R. Kelly, Laser sputtering .4. Laser interferometry and laser-induced fluorescence studies of insulators, *Radiation Effects and Defects in Solids* 99 (1986) 199-211.
113. D.K. Zerkle and A.D. Sappey, Time-resolved plif imaging of cu in a laser-ablated copper plasma plume, *IEEE Transactions on Plasma Science* 24 (1996) 37-38.
114. R.A. AlWazzan, C.L.S. Lewis, and T. Morrow, A technique for mapping three-dimensional number densities of species in laser produced plumes, *Review of Scientific Instruments* 67 (1996) 85-88.
115. K. Sasaki, S. Matsui, H. Ito, and K. Kadota, Dynamics of laser-ablation ti plasmas studied by laser-induced fluorescence imaging spectroscopy, *Journal of Applied Physics* 92 (2002) 6471-6476.
116. K. Sasaki, T. Wakasaki, S. Matsui, and K. Kadota, Distributions of c-2 and c-3 radical densities in laser-ablation carbon plumes measured by laser-induced fluorescence imaging spectroscopy, *Journal of Applied Physics* 91 (2002) 4033-4039.
117. C. Dutouquet and J. Hermann, Laser-induced fluorescence probing during pulsed-laser ablation for three-dimensional number density mapping of plasma species, *Journal of Physics D-Applied Physics* 34 (2001) 3356-3363.
118. Y. Oki, K. Furukawa, and M. Maeda, Extremely sensitive na detection in pure water by laser ablation atomic fluorescence spectroscopy, *Optics Communications* 133 (1997) 123-128.
119. G. De Boer, S. Arepalli, W. Holmes, P. Nikolaev, C. Range, and C. Scott, Detection of nickel atom by laser induced fluorescence during carbon nanotube formation in a laser produced plume, *Journal of Applied Physics* 89 (2001) 5760-5768.

120. H. Wang, H. Ohba, M. Saeki, M. Miyabe, T. Shibata, H. Miyatake, and H. Iimura, Velocity and metastable state population distributions of neodymium atoms produced by laser ablation, *Applied Physics B-Lasers and Optics* 81 (2005) 1127-1133.
121. B.T. Fisher, H.A. Johnsen, S.G. Buckley, and D.W. Hahn, Temporal gating for the optimization of laser-induced breakdown spectroscopy detection and analysis of toxic metals, *Applied Spectroscopy* 55 (2001) 1312-1319.
122. F. Vidal, S. Laville, C. Goueguel, H. Loudyi, K. Rifai, M. Chaker, and M. Sabsabi, A simple model of laser-induced fluorescence under arbitrary optical thickness conditions at the excitation wavelength, *Journal of Quantitative Spectroscopy & Radiative Transfer* 111 (2010) 2528-2533.
123. Y.Y. Feng, W. Zhang, B. Kuang, L.L. Ning, Z.K. Jiang, and Z.W. Dai, Radiative lifetime measurements on odd-parity levels of La I by time-resolved laser spectroscopy, *Journal of the Optical Society of America B-Optical Physics* 28 (2011) 543-546.
124. Y. Nakata, T. Okada, and M. Maeda, Correction of the quenching effect in two-dimensional laser-induced fluorescence measurement of laser-ablation processes, *Optics Letters* 24 (1999) 1765-1767.
125. D.D. Burgess and C.H. Skinner, Dye laser-induced fluorescence of plasmas and its application to measurement of lower state decay-rates, *Journal of Physics B-Atomic Molecular and Optical Physics* 7 (1974) L297-L301.
126. N. Omenetto and O.I. Matveev, Time-resolved fluorescence as a direct experimental approach to the study of excitation and ionization processes in different atom reservoirs, *Spectrochimica Acta Part B-Atomic Spectroscopy* 49 (1994) 1519-1535.
127. N. Omenetto, Interactions of laser-induced fluorescence and ionization techniques in atomic and molecular-spectroscopy, *Institute of Physics Conference Series* (1992) 151-154.
128. A. Okano and K. Takayanagi, Laser-induced fluorescence from collisionally excited Si atoms in laser ablation plume, *Journal of Applied Physics* 86 (1999) 3964-3972.

129. H.J. Kunze, Experimental check of local thermodynamic equilibrium in discharges, *Appl. Opt.* 25 (1986) 13-13.
130. M. Sabsabi and P. Cielo, Quantitative-analysis of aluminum-alloys by laser-induced breakdown spectroscopy and plasma characterization, *Applied Spectroscopy* 49 (1995) 499-507.

BIOGRAPHICAL SKETCH

Daniel Shelby was born in Evansville, Indiana. After attending high school at F.J. Reitz High School, he moved to Bloomington, Indiana to earn a degree in chemistry from Indiana University. In May of 2006, he graduated from IU with a Bachelor of Science in chemistry and mathematics and research experience with Dr. Gary Hieftje. Daniel began his graduate school studies with Dr. Nicolás Omenetto at the University of Florida in the fall of 2006. He graduated in the summer of 2011 with a Doctor of Philosophy in chemistry from the University of Florida.